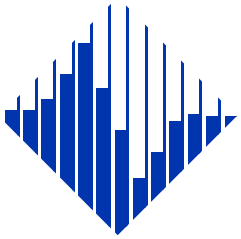

PACIFIC EARTHQUAKE ENGINEERING RESEARCH CENTER

NGA-East: Adjustments to Median Ground-Motion Models for Central and Eastern North America

PEER Report No. 2015/08

Pacific Earthquake Engineering Research Center
Headquarters at the University of California, Berkeley

August 2015

PEER 2015/08
August 2015

NGA-East: Adjustments to Median Ground-Motion Models for Central and Eastern North America

PEER Report No. 2015/08
Pacific Earthquake Engineering Research Center
Headquarters at the University of California, Berkeley

August 2015

ABSTRACT

This report documents a series of adjustments developed for the median ground-motion models (GMMs) developed as part of the Next Generation Attenuation for Central and Eastern North America (CENA) project (NGA-East). NGA-East is a multi-disciplinary research project coordinated by the Pacific Earthquake Engineering Research Center (PEER) that involves a large number of participating junior and senior researchers, practitioners, and end-users. Various organizations have provided technical input to the project from academia, industry, and government agencies. The objective of NGA-East is to develop a new ground motion characterization (GMC) model for the CENA region. The tectonic region of interest reaches across into Canada; thus, the term CENA instead of CEUS is used. The GMC consists in a set of new models (GMMs, a.k.a. GMPEs) for median horizontal ground motions, a set of standard deviation models, and their associated weights in logic trees for use in probabilistic seismic hazard analyses (PSHA).

The current report documents a set of adjustments to median GMMs that are necessary so that NGA-East (1) is applicable to rupture distances in the range from 0 to 1500 km; (2) allows source depth effects to be incorporated; and (3) is applicable to the vast CENA region to include the Gulf Coast and the Mississippi Embayment. The three corresponding adjustment models are documented herein. This report can be considered as a supplemental report to the original NGA-East PEER report on median GMMs [PEER 2015].

ACKNOWLEDGMENTS

This study was sponsored by the Pacific Earthquake Engineering Research center (PEER), as part of the NGA-East research project, and was funded by the U.S. Nuclear Regulatory Commission (NRC), the U.S. Department of Energy (DOE), and the Electric Power Research Institute (EPRI), with the participation of the U.S. Geological Survey (USGS).

Any opinions, findings, and conclusions or recommendations expressed in this material are those of the authors and do not necessarily reflect those of the sponsoring agencies.

We acknowledge the continued contributions and interactions with the following GMM developers (who are not already co-authors of chapters) who provided helpful input for this report: Norm Abrahamson, Md. Nayeem Al Noman, Gail Atkinson, Ken Campbell, Chris Cramer, Art Frankel, V. Graizer, N. Gregor, B. Hassani, S. Pezeshk, A. Shahjouei, B. Tavakoli, E. Yenier, and A. Zandieh. We also thank Karen Assatourians, Tadahiro Kishida, Robert Graves, and Jack Boatwright for timely responses to requests for clarifications and data files.

In the tradition of all NGA projects, NGA-East has also had very fruitful interactions among tens of participants. We gratefully acknowledge all NGA-East participants for their dedication and teamwork.

LIST OF ACRONYMS

We provide a list of the most common acronyms and symbols below and alternative notations when applicable.

1CCSP	Single Corner Constant Stress Parameter (DASG GMM), Table 1.2
1CVSP	Single Corner Variable Stress Parameter (DASG GMM), Table 1.2
2CCSP	Double Corner Constant Stress Parameter (DASG GMM), Table 1.2
2CVSP	Double Corner Variable Stress Parameter (DASG GMM), Table 1.2
ANC	Al Noman and Cramer GMM, Table 1.2
B_a04	Boore GMM based on Atkinson [2004], Table 1.2
B_ab14	Boore GMM based on Atkinson and Boore [2014], Table 1.2
B_ab95	Boore GMM based on Atkinson and Boore [1995], Table 1.2
B_bca10d	Boore GMM based on a Boore et al. [2010], Table 1.2
B_bs11	Boore GMM based on Boatwright and Seekins [2011], Table 1.2
B_sgd02	Boore GMM based on Silva et al. [2002], Table 1.2
CENA	Central and Eastern North America
CNA	Central North America
DASG	Darragh, Abrahamson, Silva and Gregor Model(s), Table 1.2
GC	Gulf Coast
GMC	Ground Motion Characterization
CEUS	Central and Eastern United States
CEUS SSC	Central and Eastern U.S. Seismic Source Characterization for Nuclear Facilities Project
DOE	United States Department of Energy
EPRI	Electric Power Research Institute
FAS	Fourier Amplitude Spectra
GMC	Ground Motion Characterization
GMM	Ground Motion Model is used preferably in the report, GMMs includes GMPEs and other model formats
GMPE	Ground Motion Prediction Equation is used for GMMs that have been parameterized into equations
GMIM	Ground Motion Intensity Measure (PSA, PGA, PGV)
HA15	Hassani and Atkinson GMM, Table 1.2
M	Moment magnitude
NGA	Next Generation Attenuation
NGA-East	Next Generation Attenuation Relationship for the Central and Eastern North American Region
NGA-West	Next Generation Attenuation Relationship for shallow crustal earthquakes in active tectonic regions (original project)
NGA-West2	Next Generation Attenuation Relationship for shallow crustal earthquakes in active tectonic regions (phase 2 of NGA-West project)
NRC	United States Nuclear Regulatory Commission
PEER_EX	PEER GMM based on EXSIM simulations [Atkinson and Assatourians 2015] , Table 1.2
PEER_GP	PEER GMM based on Graves and Pitarka [2015] simulations, Table 1.2

PZCT_M1SS	Pezeshk, Zandieh, Campbell and Tavakoli GMM, simulations-based magnitude scaling, Table 1.2
PZCT_M2ES	Pezeshk, Zandieh, Campbell and Tavakoli GMM, empirical magnitude scaling, Table 1.2
PGA	Peak Ground Acceleration
PGV	Peak Ground Velocity
PIE	Potentially-Induced Event
PS	Point-Source
PSA	Pseudo-Spectral Acceleration (5% damping in this report)
PSHA	Probabilistic Seismic Hazard Analysis
Q	Quality factor
R_{HYP}	Hypocentral distance (km)
R_{JB}	Joyner-Boore distance: closest distance to the horizontal projection of the earthquake rupture plane (km)
R_X	The horizontal distance from the surface projection of the top edge of the earthquake rupture to the site, measured perpendicular to the strike of the earthquake rupture (km). R_X is negative on the footwall side of the rupture and positive on the hanging-wall side
R_{RUP}	Rupture distance: closest distance to the earthquake rupture plane (km)
RotD_{50}	Median value of resultants of two horizontal components of ground motions as computed over each angle of rotation from 1 to 180°
SSC	Seismic Source Characterization
$\Delta\sigma$	Stress Parameter
T	Spectral period (in seconds)
U.S.	United States
USGS	United States Geological Survey
V_S	Shear-wave velocity
V_{S30}	Time-averaged shear-wave velocity in top 30 meters of geomaterial
WNA	Western North America
YA15	Yenier and Atkinson GMM, Table 1.2
Z_{HYP}, H_{hypo}	Depth to hypocenter (km)
Z_{TOR}	Depth to top of rupture (km)

LIST OF TABLES

Table 1.1 Minimum 5%-damped PSA periods (and frequencies) for NGA-East GMM development. 2

Table 1.2 Summary of NGA-East median GMMs. 3

Table 3.1 Fault widths (W) used in finding an average stress parameter (courtesy of R. Graves). 47

Table 3.2 Coefficients for proposed model [Equation (3.18)]. 61

Table 3.3 Magnitude dependence of Z_{TOR} from the CEUS SSC (interim model) 65

Table 4.1 Summary of events recorded in Region 1 (GC), including station distance and site conditions. All events used for the PEER model development; only events marked with * next to the EQ I.D. used for the DASG model. 69

LIST OF FIGURES

Figure 1.1 Four regions defined for Central and Eastern North America (CENA). The regions have been numbered as follows for the NGA-East database: (1) Mississippi Embayment/Gulf Coast region; (2) Central North America; (3) the Appalachian Province; and (4) the Atlantic Coastal Plain. Together, Regions 2, 3 and 4 form the larger mid-continent region. 6

Figure 2.1 Z_{TOR} values calculated for strike–slip and reverse faulting events for two hypocentral depths. 11

Figure 2.2 Illustration of R_{RUP} conversion for the DASG 1CVSP model at 1 Hz. 11

Figure 2.3 Illustration of R_{RUP} conversion for the HA15 model at 1 Hz....12

Figure 2.4 Illustration of R_{RUP} conversion for the SP15 model at 1 Hz. 12

Figure 2.5 Distance extensions for the B_a04, 1Hz PSA. The left frame shows the extended regions in blue and red; the right frame shows the final model. 15

Figure 2.6 Distance extensions for the B_a04, 10 Hz PSA. The left frame shows the original predictions in black and the extended regions in blue and red; the right frame shows the final model. The right panel shows the results of the algorithm used to prevent the crossover. 15

Figure 2.7 Distance extensions for the DASG 1CCSP GMM, 1 Hz PSA. The left frame shows the original predictions in black and the fitted model in red; the right frame shows the final model....16

Figure 2.8 Large distance extensions for the YA15 GMM, 1 Hz PSA. The left frame shows the original predictions in black, and the green line shows the lower-bound limit of ground motions used to fit the model (in red); the right frame shows the final model. 17

Figure 2.9 Illustration of short-distance correction [Equations (2.6)–(2.9)] for the 25 Hz PSA example of YA15. The left frame shows the original predictions in black, the dashed green line is anchored at 15 km, the solid green line shows the lower-bound limit of ground motions used to fit the model at large distances, and the red line shows the model; the right frame shows the final model, including the short distance corrections and the large distance extrapolations. 19

Figure 2.10 Large distance extrapolations for the PZCT_M1SS GMM, 1 Hz PSA. The left frame shows the original predictions in black, and the green line shows the lower-bound limit of ground motions used to fit the model (dashed red lines show the model fit and solid red lines show the extrapolations); the right frame shows the final model. 20

Figure 2.11 Extrapolation of Frankel GMM, 0.1 Hz PSA, Case 1 example. The left frame shows open black circles for Z_{TOR} = 5 km simulations, solid black circles for Z_{TOR} = 1 km simulations, green circles for ground motions extrapolated to R_{RUP} = 0 km for **M**7.5 and **M**8 and open red circles for the extrapolations (short and large distances); the right frame shows the final model.....22

Figure 2.12 Extrapolation of Frankel GMM, 0.2 Hz PSA, Case 2 example. The left frame shows open black circles for Z_{TOR} = 5 km simulations, solid black circles for Z_{TOR} = 1 km simulations, green circles for ground motions extrapolated to R_{RUP} = 0 km for **M**7.5 and **M**8 and open red circles for the extrapolations (short and large distances); the right frame shows the final model.....23

Figure 2.13 Extrapolation of SP15 GMM, 1 Hz PSA. The left frame shows the original predictions in black, and the green line shows the lower-bound limit of ground motions used to fit the model at large distances (dashed red lines show the model fit and solid red lines show the extrapolations); the right frame shows the final model. 24

Figure 2.14 AND15 GMM ground motions for 1 Hz PSA. The model has not been extrapolated. 25

Figure 2.15 Graizer GMM ground motions for 1 Hz PSA. The model has not been extrapolated and is used as-is over the full distance range. 26

Figure 2.16 Illustration of extrapolation for the HA15 GMM, PSA 1 Hz. The left frame shows the original predictions in black, the dashed green line is anchored at 20 km, the solid green line shows the lower-bound limit of ground motions used to fit the model at large distances (anchored at 120 km), and the red lines show the model; the right frame shows the final model.....27

Figure 2.17 Illustration of extrapolation for the PEER_GP GMM, PSA 1 Hz. The left frame shows the original predictions in black and the extrapolations in red; the right frame shows the final model.....28

Figure 2.18 Example of spectral-shape correction showing the 1CCSP spectrum for **M**8 and R_{RUP} = 1200 km. The blue line is the original spectrum showing a trough-and-peak pair at high frequencies. The purple line shows the adjusted spectrum.....29

Figure 2.19 Example of spectral-shape correction showing the PEER_GP spectrum for **M**8 and R_{RUP} = 1200 km. The blue line is the original spectrum showing a trough at high frequencies. The purple line shows the adjusted spectrum. 29

Figure 3.1 Taken from Frankel in PEER [2015], Chapter 6, Figure 6.9: 3.0-sec PSA values from two of the **M**5.5 simulations showing the effect of changing the depth of the rupture. 32

Figure 3.2 Magnitude-depth distribution of events for which YA15 determined stress parameters. The heavy blue line indicates the depth used in deriving the ground motions provided to the NGA-East project. 34

Figure 3.3 YA15 stress parameters as a function of magnitude. The lines are their equations. 35

Figure 3.4 YA15 stress parameters as a function of focal depth. The lines are their equations. 36

Figure 3.5 Magnitude-depth distribution of events for which Boatwright determined stress parameters. 37

Figure 3.6 Boatwright's stress parameters as a function of magnitude. The eastern Quebec points are subdivided into events with focal depths less than and greater than 10 km. The lines are from Yenier and Atkinson for **M** = 4 and a subjective fit by David Boore to DASG values (see Section 3.2.2). 38

Figure 3.7 Boatwright's stress parameters as a function of focal depth. The eastern Quebec points are subdivided into events with magnitudes less than and greater than 4. The western Quebec symbols have been enlarged so that two of the values at a depth near 5 km can be seen. The lines are from Yenier and Atkinson for **M** = 4 and a subjective fit by David Boore to Boatwright's values. 39

Figure 3.8 Magnitude-depth distribution of events for which Darragh et al. determined stress parameters. The horizontal blue lines show the depth range used in the simulations (it is our understanding that these depths were used to give a range of R_{RUP} for a given R_{JB}; no depth dependence of $\Delta\sigma$ was used in the simulations). 41

Figure 3.9 DASGs stress parameters as a function of magnitude. The lines are from YA15 for **M**4 and a subjective fit by D.Boore to DASG's values. Also shown by lines are the stressed used by DASG for **M**4.5 and **M**5.5, as well as for their magnitude-dependent stress model for larger magnitudes (the magenta line)....42

Figure 3.10 DASG's stress parameters as a function of focal depth. The solid lines are from Yenier and Atkinson for **M**4 and a subjective fit by D. Boore to Boatwright's values for eastern Quebec. Those lines were adjusted downward by the indicated factors to account for the differences in the values of $\Delta\sigma$ (see text for details). The horizontal dashed lines are values in DASG's depth-dependent $\Delta\sigma$ model for two magnitudes; the vertical magenta lines show the range of depths used in DASG's simulations (but they did not allow any depth dependence of $\Delta\sigma$ in their simulations—see caption to Figure 3.8). 44

Figure 3.11 The stress parameter–depth function used in the simulations. Shown is the $\Delta\sigma(z)$ function from the inversions discussed earlier, as well as the stress parameters used in the simulations for three magnitudes (**M** = 4, 6, and 8); these parameters were derived by an averaging of a power of $\Delta\sigma(z)$ over the width of the fault for each magnitude. 46

Figure 3. 12 Ratio of simulated motions from point sources at depths *z* (in km) and 10 km, for **M** = 4 and two values of R_{RUP}: (20 km and 200 km). The relation between $\Delta\sigma$ and *z* discussed above was used in choosing the $\Delta\sigma$ to be used for the point source at each depth *z*. 49

Figure 3.13 Ratio of simulated motions from point sources at depths *z* (in km) and 10 km for **M** = 5 and two values of R_{RUP} (20 km and 200 km). The relation between $\Delta\sigma$ and z discussed above was used in choosing the $\Delta\sigma$ to be used for the point source at each depth *z*. 50

Figure 3.14 Ratio of simulated motions from point sources at depths *z* (in km) and 10 km for **M** = 6 and two values of R_{RUP} (20 km and 200 km). The relation between $\Delta\sigma$ and *z* discussed above was used in choosing the $\Delta\sigma$ to be used for the point source at each depth *z*. 51

Figure 3.15 Ratio of simulated motions from point sources at depths *z* (in km) and 10 km for **M** = 7 and two values of R_{RUP} (20 km and 200 km). The relation between $\Delta\sigma$ and *z* discussed above was used in choosing the $\Delta\sigma$ to be used for the point source at each depth *z*. 52

Figure 3.16 Ratio of simulated motions from point sources at depths *z* (in km) and 10 km for **M**=8 and two values of R_{RUP} (20 km and 200 km). The relation between $\Delta\sigma$ and z discussed above was used in choosing the $\Delta\sigma$to be used for the point source at each depth *z*. 53

Figure 3.17 Ratio of simulated T = 0.2 sec response spectra from point sources at the indicated depth $Z_{TOR} = z$ and Z_{TOR} = 10 km for **M**=4, 5, 6, 7, and 8, and R_{RUP} = 20 km. The stress parameter used in the simulations was from an average of $\Delta\sigma(z)$ over the fault width for each magnitude event. 54

Figure 3.18 Focal depth—magnitude scatterplot for events in the 18 November 2014 NGA-East database flatfile [Goulet et al. 2014]. 55

Figure 3.19 Source-depth model scale factors for the three NGA-West2 models and the implied source-depth scaling factor from the PEER NGA-East model: CY14 in dark green, ASK14 in blue and, CB14 in black, PEER in magenta (top **M** = 5.0, middle **M** = 6.5, and bottom **M** = 8.0). 59

Figure 3.20 Source-depth model scaling factors for the average of the three NGA-West2 models (cyan) and the proposed source-depth adjustment model (red). The NGA-West2 models and the implied source-depth scaling factor from the PEER NGA-East model are included for comparison: CY14 in dark green, ASK14 in blue and, CB14 in black, and PEER NGA-East in magenta (top **M** = 5.0 and bottom **M** = 6.5). 62

Figure 3.21 Proposed source-depth model scale factors for **M** = 5.0, 5.5, 6.0, and 6.5.....63

Figure 4.1 Magnitude (**M**) and rupture distance (R_{RUP}) ranges for records in the NGA-East database from Path Region 1 (i.e., both the earthquake source and the site are located in the GC region).....69

Figure 4.2 Number of events (N_e), stations (N_{stat}) and, records (N_{rec}) per frequency of PSA for Region 1 (GC).....70

Figure 4.3 Comparison of the number of events (N_e), stations (N_{stat}), and records (N_{rec}) available per PSA frequency from the NGA-East database (solid blue line) and the subset of records used by the PEER modeling group (dashed red line).....72

Figure 4.4 Total residuals plotted against rupture distance for PSA at frequencies 0.5, 1.0, 5.0, and 10.0 Hz. Blue points are observations from tectonic events, and red points are observations from PIE. The black lines represent a linear fit to the data with ± standard error in dashed lines. The red lines represent a locally weighted least-squares fit to the data with ± standard error in dashed lines.....75

Figure 4.5 Comparison of model constant, c_0, for EM1 (black), EM2 (red), and the proposed model (green) plotted against frequency of PSA. Note that coefficient c_0 value is equal to zero for EM1 and the proposed model.....76

Figure 4.6 Comparison of model coefficient, c_7', for EM1 (black), EM2 (red), and the proposed model (green) plotted against frequency of PSA. The c_7' for the proposed model are taken as the average of points from EM1, taken in the 0.5–10 Hz range, where the data is deemed more reliable.....76

Figure 4.7 **B**etween-event residuals for EM1 (black points) and EM2 (red points) plotted against magnitude for PSA at frequencies 0.5, 1.0, 5.0, and 10.0 Hz. The largest event (**M**4.71) is a PIE, all other events are tectonic.....77

Figure 4.8 Between-event (squares), and within-event (triangles) standard deviations for EM1 (solid black points) and EM2 (open red points) plotted against frequency of PSA.....78

Figure 4.9 Model 1 within-event residuals plotted against rupture distance for PSA at frequencies 0.5, 1.0, 5.0, and 10.0 Hz. Blue points are observations from tectonic events, and red points are observations from PIE.....79

Figure 4.10 Model 2 within-event residuals plotted against rupture distance for PSA at frequencies 0.5, 1.0, 5.0, and 10.0 Hz. Blue points are observations from tectonic events, and red points are observations from PIE.....80

Figure 4.11 Within-event residuals for EM1 (black points) and EM2 (red points) plotted against rupture distance for PSA at frequencies 0.5, 1.0, 5.0, and 10.0 Hz.....81

Figure 4.12 Gulf Coast adjustment ratios from EM (black), EM2 (red), and the proposed model (green) plotted against rupture distance for PSA at frequencies 0.5, 1.0, 5.0, and 10.0 Hz.....83

Figure 4.13 Gulf Coast adjustment ratios of the four DASG models along with the mean DASG ratios (solid blue) plotted against rupture distance for PSA at frequencies 0.5, 1.0, 5.0, and 10.0 Hz.....86

Figure 4.14 Comparison of Gulf Coast adjustment ratios between DASG model (blue) and the PEER model (green) plotted against distance for PSA at frequencies 0.5, 1.0, 5.0, and 10.0 Hz.....88

CONTENTS

ABSTRACT ..... **iii**

ACKNOWLEDGMENTS ..... **v**

LIST OF ACRONYMS ..... **vii**

LIST OF TABLES ..... **ix**

LIST OF FIGURES ..... **xi**

TABLE OF CONTENTS ..... **xvii**

1 INTRODUCTION **1**

1.1 Purpose **1**

1.2 Summary of the NGA-East Median GMMs **2**

1.3 Adjustments to NGA-East: Rationale **4**

1.3.1 Distance Extrapolation 4

Short-Distance Extrapolation *4*

Large-Distance Extrapolation *4*

Spectral-Shape Adjustment at High Frequencies *5*

1.3.2 Modeling of Source-Depth Effects 5

1.3.3 Regional Adjustments for the Gulf Coast and Mississippi Embayment 5

2 EXTENSION OF MEDIAN GROUND-MOTION MODELS TO SHORT AND LARGE DISTANCES **9**

2.1 Conversion from R_{JB} to R_{RUP} **9**

2.2 Distance Extrapolation: General Approach **13**

2.2.1 Short-Distance Extrapolation (< 10 km) 13

2.2.2 Large-Distance Extrapolation (up to 1500 km) 13

2.3 Extrapolation Specific to Each GMM **13**

2.3.1 Boore GMMs 14

2.3.2 Darragh, Abrahamson, Silva, and Gregor (DASG) GMMs 16

2.3.3 Yenier and Atkinson (YA15) GMM 17

2.3.4 Pezeshk, Zandieh, Campbell, and Tavakoli (PZCT) GMMs 19

2.3.5 Frankel GMM 20

2.3.6 Shahjouei and Pezeshk (SP15) GMM 23

2.3.7 Al Noman and Cramer (ANC) GMM 24

2.3.8 Graizer GMM 25

2.3.9 Hassani and Atkinson (HA15) GMM 26

2.3.10 PEER GMMs 27

2.4 Spectral-Shape Adjustments 28

3 ADJUSTMENT FOR SOURCE DEPTH 31

3.1 Introduction 31

3.2 Depth and Stress Parameter from CENA Data 32

3.2.1 Depth-Dependence of the Stress Parameter: Evidence from Data Inversion Exercises 33
YA15's Derived Stress Parameters 33
Boatwright's Derived Stress Parameters 36
DASG's Derived Stress Parameters 40
3.2.2 Consequences of a Depth-Dependent Stress Parameter using the Point-Source Stochastic Model 45
The Stress Parameter–Depth Function, $\Delta\sigma(z)$ 45
Simulated Motions using SMSIM 47
Discussion 55

3.3 Existing Source-Depth models 56

Chiou and Youngs 2014 56
Abrahamson, Silva, and Kamai 2014 57
Campbell and Bozorgnia 2014 57
PEER NGA-East Median GMM 58
Comparisons of Source-Depth Scaling Models 58

3.4 Development of Source-Depth Adjustment Model 60

3.4.1 Source-Depth Scaling 60
3.4.2 Centering of Source-Depth Adjustment Model 63
CEUS SSC-Based Magnitude Dependence of Z_{TOR} (Interim Model) 64

4 ADJUSTMENT FOR GULF COAST AND MISSISSIPPI EMBAYMENT REGION 67

4.1 Introduction 67

4.1.1 Overview of Available Gulf Coast Data in the NGA-East Database 68

4.2 PEER Gulf Coast Adjustment Model 70

4.2.1 Overview of PEER NGA-East Median GMM 71
4.2.2 Selection of Data 71
4.2.3 Model Development 73

4.3 DASG Gulf coast Adjustment Model 84

4.3.1 Overview of DASG NGA-East Median GMM 84
4.3.2 Updated Point-Source Inversions 84
4.3.3 PSA Ratio Model 85

4.4 Comparison of Gulf Coast Adjustment Models 87

REFERENCES.....89

ELECTRONIC APPENDIX A 91

ELECTRONIC APPENDIX B 93

1 Introduction

Christine A. Goulet, Yousef Bozorgnia

Pacific Earthquake Engineering Research Center (PEER)
University of California, Berkeley

Norman A. Abrahamson

Pacific Gas and Electric Company
San Francisco, California

1.1 PURPOSE

This report presents a summary of adjustments to be applied to the median Ground Motion Models (GMMs) developed as part of the Next Generation Attenuation for Central and Eastern North America (CENA) project (NGA-East). The twenty-one new GMMs are documented in a separate report [PEER 2015] and are introduced below.

The objective of NGA-East is to develop a new ground motion characterization (GMC) for the CENA region. The GMC consists of a set of new GMMs (a.k.a., GMPEs) for median horizontal ground motions, a set of standard deviation models, and their associated weights in logic trees. The NGA-East GMC is to be used in conjunction with the Central and Eastern U.S. Seismic Source Characterization (CEUS SSC) products [EPRI/DOE/NRC 2012] to conduct probabilistic seismic hazard analyses (PSHA).

Over the course of the NGA-East Project, the goals for the GMC evolved to include the following: (1) it should be applicable from the source to 1500 km; (2) it should allow source-depth effects to be modeled; and (3) it should be applicable to the vast CENA region to include the Gulf Coast and the Mississippi Embayment. The median GMMs documented in the previous PEER report [2015] did not address these specific issues, and the NGA-East Project undertook the development of three types of adjustments to address them. This chapter presents a brief summary of the available GMMs, which is followed by a short description of the motivation for each of the three adjustments. The subsequent chapters are dedicated to each of these adjustments.

1.2 SUMMARY OF THE NGA-EAST MEDIAN GMMS

This report uses the term GMM as a general term (as some models have been parameterized into equations), and the term "ground-motion prediction equations (GMPE)" is applicable; other models consist of sets of ground-motion tables [PEER 2015]. The more general term GMM is applicable to all the models in their various forms.

The median GMMs provide "average" horizontal ground motions on very hard-rock (VHR) sites located up to 1500 km from future earthquakes in CENA, with **M** in the 4.0 to 8.2 range. The VHR reference site conditions have been defined by the NGA-East Geotechnical Working Group as corresponding to shear-wave velocity V_S = 3000 m/sec and a kappa (κ) of 0.006 sec [Hashash et al. 2014]. The preferred "average" horizontal ground-motion intensity measure (GMIM) is $RotD_{50}$ [Boore 2010]. $RotD_{50}$is the median value of resultants of two horizontal components of ground motions as computed over each angle of rotation from 1 to 180°. $RotD_{50}$ is computed independently for each spectral period/frequency. The minimum requested GMIMs are peak ground acceleration (PGA), peak ground velocity (PGV), and 5%-damped linear pseudo-spectral acceleration (PSA) for oscillator periods listed in Table 1.1.

Table 1.1 Minimum 5%-damped PSA periods (and frequencies) for NGA-East GMM development.

T **(sec)**	***F*** **(Hz)**
0.01	100
0.02	50
0.025	40
0.03	33.33
0.04	25
0.05	20
0.075	13.33
0.1	10
0.15	6.67
0.2	5
0.25	4
0.3	3.33
0.4	2.5
0.5	2
0.75	1.33
1	1
1.5	0.67
2	0.5
3	0.33
4	0.25
5	0.2
7.5	0.13
10	0.1

The twenty-one models are listed in Table 1.2. They are documented in detail in the previous PEER report [2015]; the title, authorship and chapter number listed in Table 1.2 refer to that specific report. The acronyms are used in the text and in various figures in the current report and are provided for convenience. All the GMMs are for footwall conditions, with adjustments for hanging-wall conditions developed in a separate task. In addition, GMM developers have focused on limiting their developed models to the mid-continent region (CENA region that excludes the Gulf Coast, as defined in Section 1.3.3).

Table 1.2 Summary of NGA-East median GMMs.

Title (Authorship), chapter number in *PEER Report 2015/04* [2015]	**Acronym(s)**
Point-Source Stochastic-Method Simulations of Ground Motions for the PEER NGA-East Project (D.M. Boore), Chapter 2.	Six GMMs from Boore, each based on a different Q and geometrical spreading model: B_a04 B_ab14 B_ab95 B_bca10d B_bs11 B_sgd02
Development of Hard Rock Ground-Motion Models for Region 2 of Central and Eastern North America (R.B. Darragh, N.A. Abrahamson, W.J. Silva, and N. Gregor), Chapter 3.	Four GMMs from DASG, each based single or double point source and on constant or variable stress parameter: 1CCSP 1CVSP 2CCSP 2CVSP
Regionally-Adjustable Generic Ground-Motion Prediction Equation based on Equivalent Point-Source Simulations: Application to Central and Eastern North America (E. Yenier and G.M. Atkinson), Chapter 4.	YA15
Ground-Motion Prediction Equations for Eastern North America using a Hybrid Empirical Method (S. Pezeshk, A. Zandieh, K.W. Campbell, and B. Tavakoli), Chapter 5.	Two GMMs from PZCT based on different large **M**-scaling (simulation- and empirical-based): PZCT15_M1SS PZCT15_M2ES
Ground-Motion Predictions for Eastern North American Earthquakes Using Hybrid Broadband Seismograms from Finite-Fault Simulations with Constant Stress-Drop Scaling (A. Frankel), Chapter 6.	Frankel
Hybrid Empirical Ground-Motion Model for Central and Eastern North America using Hybrid Broadband Simulations and NGA-West2 GMPEs (A. Shahjouei and S. Pezeshk), Chapter 7.	SP15
Empirical Ground-Motion Prediction Equations for Eastern North America (M.N. Al Noman and C.H. Cramer), Chapter 8.	ANC15
Ground-Motion Prediction Equations for the Central and Eastern United States (V. Graizer), Chapter 9.	Graizer
Referenced Empirical Ground-Motion Model for Eastern North America (B. Hassani and G.M. Atkinson), Chapter 10.	HA15
PEER NGA-East Median Ground-Motion Models (J. Hollenback, N. Kuehn, C.A. Goulet and N.A. Abrahamson), Chapter 11.	Two GMMs from PEER, based on alternate finite-fault models: PEER_GP PEER_EX

1.3 ADJUSTMENTS TO NGA-EAST: RATIONALE

This section summarizes the motivations for developing the three types of adjustments discussed in this report.

1.3.1 Distance Extrapolation

Short-Distance Extrapolation

The GMC is to be implemented in hazard analysis codes and should cover the complete range of distances in the CEUS SSC, including 0 km or values very close to 0 km, in terms of closest distance to the rupture plane, R_{RUP}. As source depth tends to be magnitude-dependent, it is very unlikely to have a **M**4 event rupture to the surface, but making this source depth and **M** combination possible and defined in the GMC may prevent computational problems in hazard codes.

The various GMMs listed in Table 1.2 cover a wide range of distances based on two main distance metrics: the Joyner-Boore Distance, R_{JB}, and the closest distance to the rupture plane, R_{RUP}. The R_{JB} distance is defined as the horizontal distance from the projection of the earthquake rupture plane on the Earth's surface. It is therefore zero everywhere above the rupture plane and does not include depth. However, the GMMs that use R_{JB} often incorporate a "fictitious depth" to allow for the near saturation of ground-motion levels at very short distances observed in empirical data. Note that GMMs that use R_{RUP} also include such terms to model ground-motion saturation at very short distances.

The NGA-East Project decided to include both R_{RUP} and source depth as parameters for the final GMC, implying that the ground motions from all the R_{JB}-based models had to be converted to R_{RUP}. This is a simple correction if the average depths used in the assumption of the models are known or are in the dataset used to constrain the models. However, when this simple conversion is applied, it is possible that the resulting extensions to R_{RUP} near and at 0 km may not be reasonable, depending on the specific modeling assumptions. For that reason, an extrapolation scheme based on fitting of ground-motion values with (converted) R_{RUP} values at larger distances, typically 10 km and larger, was developed. These topics are discussed in Sections 2.1 and 2.2.

Large-Distance Extrapolation

As documented in the previous PEER report [2015], the NGA-East team requested that all the GMMs provide ground motions up to 1200 km. Following recent hazard analysis runs and based on experience in assessment of hazard for nuclear facilities, the NGA-East Project team extended the distance range from 1200 to 1500 km. This large distance allows for application of the GMMs at sites in regions with low seismicity where ground motions from a large, distant earthquake (such as from the New Madrid fault zone) contribute significantly to the site hazard. Because the intent for the NGA-East Project team was to have evaluated the model over the full range of distances to which it is likely to be applied, extrapolation of all the models to 1500 km was therefore required.

In addition, most models were not strongly calibrated for distances beyond about 400 or 600 km. The difficulty of calibration at large distance using data (NGA-East database [Goulet et

al. 2014]) is primarily due to the lack of ground-motion records at large magnitudes. Because most of the data is from earthquakes smaller than **M**6, the ground motions at large distances are fairly weak and often below the noise threshold for a wide frequency band. The only ground motions that remain are those motions that are "exceptionally high" for the given magnitude and distance, effectively biasing the dataset. This effect is denoted as distance censoring of the data and has been discussed in the literature with respect to development of GMPEs from empirical data; see, for example, Abrahamson et al. [2014] and Chiou and Youngs [2014]. NGA-East therefore proposed to develop "reasonable" extrapolation rules for large distances as an alternative to the original GMM ground motions. This extrapolation is discussed in Section 2.3.

Spectral-Shape Adjustment at High Frequencies

The extrapolated models went through one additional adjustment to correct for spectral-shape issues at high frequencies. The description of the observed trends and the solution, which affect spectra from some GMMs at large-distance earthquake scenarios (beyond 400 km), are described in Section 2.4.

The electronic appendix includes the median GMMs as modified, with the extrapolations and spectral-shape adjustments described in Chapter 2. The output files have the same format and layout as those provided in the original NGA-East GMM PEER report [2015].

1.3.2 Modeling of Source-Depth Effects

The issue of source-depth effects was discussed in NGA-East workshops and working meetings. Various researchers, including Dr. Boatwright, presented data-based evidence of this important contribution to ground motions in CENA. The importance of source depth on the ground-motion prediction has already been established for crustal earthquakes in NGA-West1 [Power et al. 2008] and NGA-West2 [Bozorgnia et al. 2014]. However, the scaling of ground motions with source depth was not specifically addressed in the original NGA-East median GMMs [PEER, 2015]. Of the ten developers who provided ground motions for the NGA-East project, only two [Yenier and Atkinson (YA15) and PEER] included a focal-depth dependence of the motions as a fundamental part of their methodology. The motions provided by those developers were for nominal focal depths, however, and did not include a focal-depth as a variable (such as hypocentral depth Z_{HYP} or the depth to the top of rupture Z_{TOR}). The depth issue is summarized in Chapter 3, which covers the evidence of source-depth effects, the evaluation of depth effects' potential impact on ground motions beyond the recorded events (larger **M**), and the development of a source-depth effects model based on a combination of NGA-West2 models and NGA-East data.

1.3.3 Regional Adjustments for the Gulf Coast and Mississippi Embayment

A separate task in NGA-East was to regionalize CENA on the basis of systematic differences in simulated ground motions and their attenuation. From this task four distinct regions were defined as follows [Dreiling et al. 2014]:

1. Mississippi Embayment/Gulf Coast region (MEM or GC, both acronyms used)
2. Central North America (CNA)

3. The Appalachian Province (APP)
4. The Atlantic Coastal Plain (ACP)

These four regions are shown in Figure 1.1; numbering protocol is consistent with that used in the NGA-East flatfile [Goulet et al. 2014]. The flatfile includes three separate fields for regionalization. The first two correspond to the "Event and Station Region Number," respectively. For these two fields, the number directly corresponds to the region containing the epicenter (Event Field) and the station (Station Field). If the epicenter or the station is outside these four regions, the flag is set to -999.

The third and last regionalization field is called "Path Region Number" and aims to define a region containing the full propagation path (from the epicenter to the Station). If the full path is contained within any of the four regions above, the field is populated with the region number directly. If either or both of the Event or Station Region Number are outside the four regions (at least one of the fields is -999), then the Event Station Field is also -999.

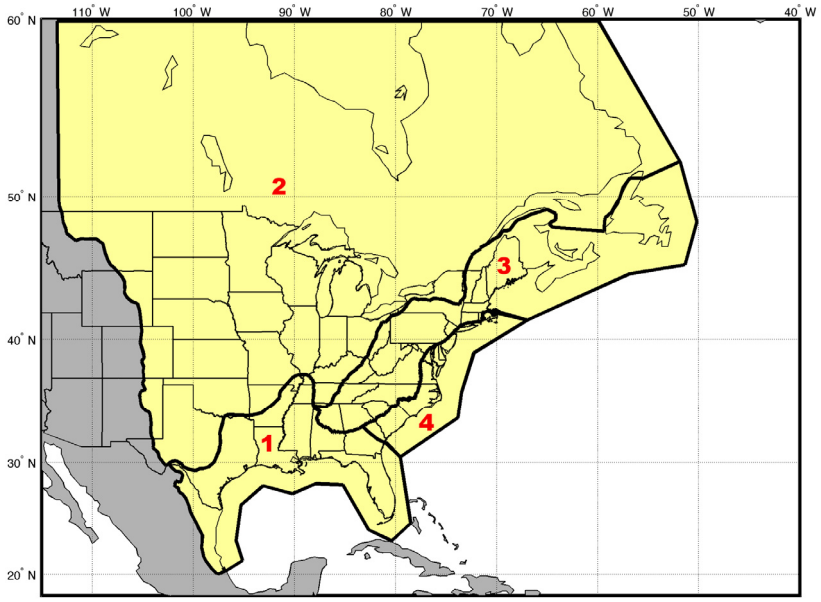

Figure 1.1 Four regions defined for Central and Eastern North America (CENA). The regions have been numbered as follows for the NGA-East database: (1) Mississippi Embayment/Gulf Coast region; (2) Central North America; (3) the Appalachian Province; and (4) the Atlantic Coastal Plain. Together, Regions 2, 3 and 4 form the larger mid-continent region.

The regionalization task also demonstrated that the four regions could be aggregated into two distinct attenuation groups:

Mid-continent (Group 1): Central North America (CNA), Appalachians (APP), and Atlantic Coastal Plain (ACP)

Gulf Coast (Group 2): Mississippi Embayment/Gulf Coast (MEM or GC)

Two new regions were created to accommodate this grouping. Region 5 includes paths that cross any or many of the boundaries of Regions 2, 3, and 4 (i.e., within the mid-continent group). Region 6 allows for paths crossing the boundary between any sub-region of the mid-continent group and the Gulf Coast group.

All the GMMs from Table 1.1 were developed for the mid-continent region. There is very limited data in the Gulf Coast region, making the development of stand-alone GMMs impractical (see Section 4.1.1). Therefore, the NGA-East team favored developing two models to provide adjustments to the existing GMMs for applicability to the Gulf Coast region. With these two new models, which can be applied to any of the existing mid-continent GMMs, it is possible to cover the complete CENA region. The model development is presented in Chapter 4. Adjustments for the Gulf Coast region are provided in the form of tables in the electronic appendix.

2 Extension of Median Ground-Motion Models to Short and Large Distances

Robert R. Youngs

Amec Foster Wheeler
Oakland, California

Nicolas Kuehn

Pacific Earthquake Engineering Research Center
University of California, Berkeley

As mentioned in Section 1.3.1, most median GMMs required extrapolations at close and/or large distances to cover the full range of R_{RUP} (0–1500 km). This chapter summarizes the extrapolation procedures for each of the median GMMs documented in the previous PEER report [2015]. A series of interactions with the GMM developers facilitated refinement of the extrapolation schemes documented here, and the final ground-motion estimates have been approved by the model developers. Plots of results and tables containing all the ground motions are available in Electronic Appendix A associated with this report.

2.1 CONVERSION FROM R_{JB} TO R_{RUP}

The median GMMs listed in Table 1.2 are available as electronic appendices to the previous PEER report [2015]. Each GMM includes an EXCEL workbook with a worksheet that provides ground motions for either PGA, PGV, or PSA at a given frequency. Each worksheet includes ground-motion values for different magnitudes and distances. The full magnitude range covers **M** = 4–8.2, and the distance range covers 0 to 1500 km. Different modeling groups provide ground motions for two different distance metrics: R_{JB} and R_{RUP}. The Joyner-Boore distance R_{JB} is the shortest distance to the horizontal projection of the rupture plane, while the rupture distance R_{RUP} is the shortest distance to the rupture plane. Because the final NGA-East models are required to provide ground-motion values for R_{RUP}, ground motions from GMMs using R_{JB} need to be converted.

The following GMMs provide ground-motion values for R_{JB}:

- The Darragh et al. (DASG) suite of models:
  - Single-Corner Constant Stress Parameter (1CCSP)

- Single-Corner Variable Stress Parameter (1CVSP)
- Double-Corner Constant Stress Parameter (2CCSP)
- Double-Corner Variable Stress Parameter (2CVSP)

- Hassani and Atkinson (HA15)
- Shahjouei and Pezeshk (SP15)

The conversion from R_{JB} to R_{RUP} assumes that the ground motions provided by the developers are valid for the footwall. For a given value for the depth to the top of the rupture, Z_{TOR}, the corresponding rupture distance value for a given R_{JB} value can be calculated by

$$R_{RUP} = \sqrt{R_{JB}^{\ 2} + Z_{TOR}^{\ 2}} \tag{2.1}$$

This provides a corresponding R_{RUP} value for each prediction. Then, interpolation is conducted in $logR_{RUP}$ /$logY$ space to calculate ground-motion values for other values of R_{RUP} (where $logY$ is the natural logarithmic value of ground motions).

A Z_{TOR} value is calculated for each magnitude as follows: for a given a hypocentral depth, average hypocenter depth ratios, a dip of the rupture, a rupture area relationship, and the aspect ratio of the rupture, the nominal depth to the top and bottom can be calculated. The rupture area relationship is from Somerville [2014]:

$$Log_{10}A = \mathbf{M} - 4.25 \tag{2.2}$$

The aspect ratio is 1:1 (Table 5.4-1 in EPRI/DOE/NRC [2012]). For strike–slip events, a dip of 75° is used; for reverse events the dip is 45° (Table 5.4-1 in EPRI/DOE/NRC [2012]). The average depth ratio is computed using the Chiou and Youngs [2008] model (Appendix B in report); they are 0.6375 for strike–slip events and 0.628 for reverse events.

For the DASG models, a fixed hypocentral depth of 8 km is assumed, which is concordant with the development of their model (Chapter 3 of PEER [2015]). For the HA15 model, a fixed hypocentral depth of 10 km is used as an average of the depths of events in the NGA-East flatfile (12 km) and the depth suggested by Chapter 5 of EPRI/DOE/NRC [2012] (8 km). With these inputs, Z_{TOR} values can be calculated for strike–slip and reverse faulting events. For the conversion, the mean value of the two is used. In Figure 2.1, the Z_{TOR} values for each magnitude are shown for two hypocentral depths. Figures 2.2–2.4 show the models originally developed for R_{JB} after their conversion to R_{RUP}.

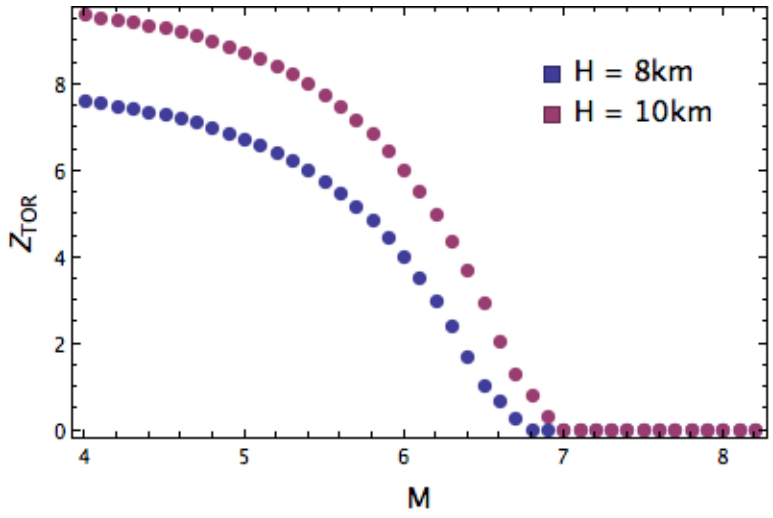

Figure 2.1 Z_{TOR} values calculated for strike–slip and reverse faulting events for two hypocentral depths.

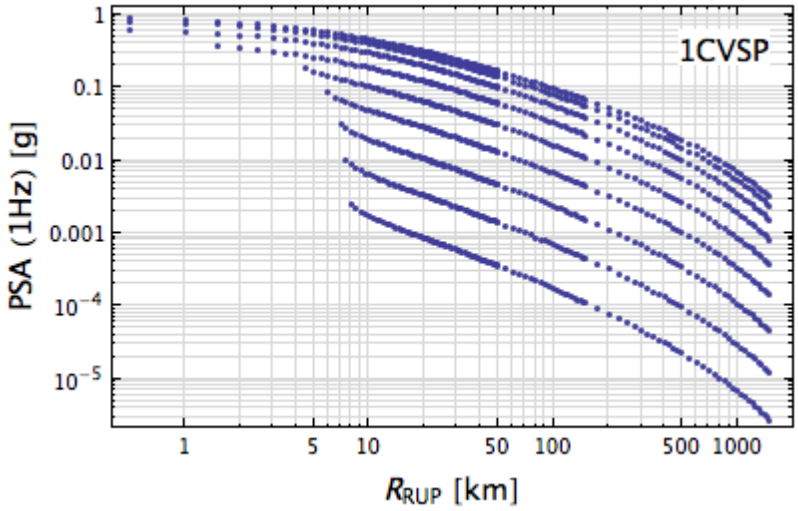

Figure 2.2 Illustration of R_{RUP} conversion for the DASG 1CVSP model at 1 Hz.

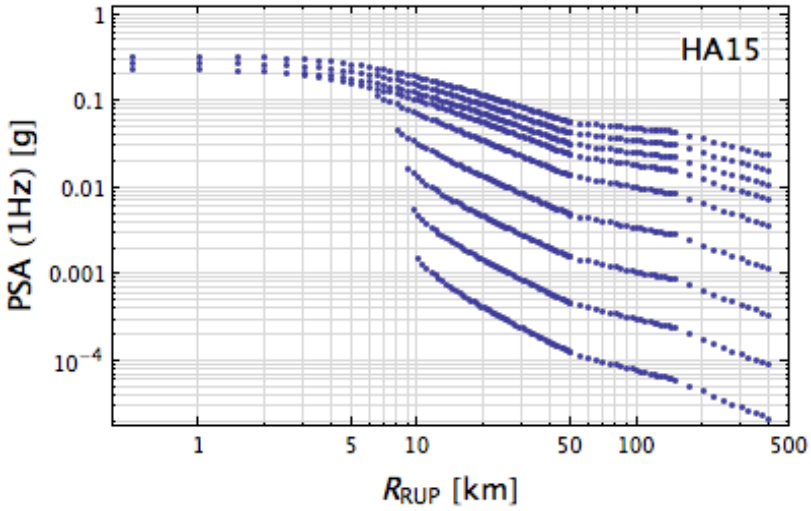

Figure 2.3 Illustration of R_{RUP} conversion for the HA15 model at 1 Hz.

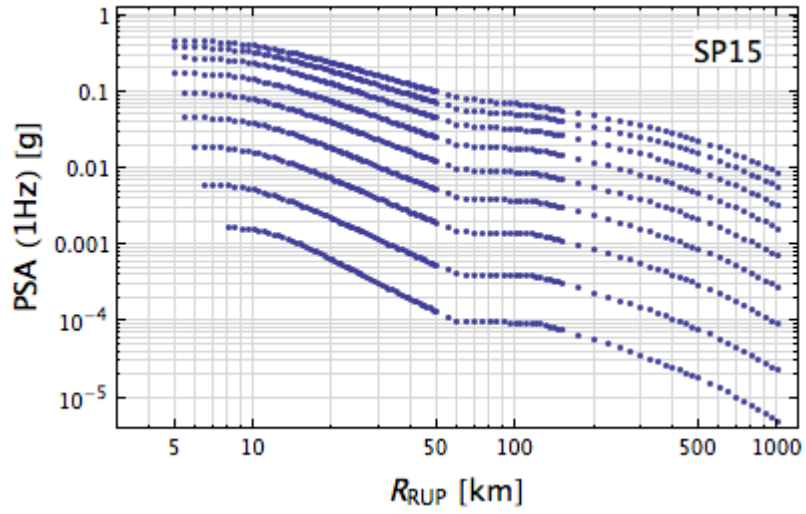

Figure 2.4 Illustration of R_{RUP} conversion for the SP15 model at 1 Hz.

2.2 DISTANCE EXTRAPOLATION: GENERAL APPROACH

2.2.1 Short-Distance Extrapolation (< 10 km)

For models that require extrapolation to R_{RUP} = 0 km, one of two functional forms is fit to the median predictions in the distance range where the geometric spreading term in the original model development is approximately constant (except for near-source saturation effect), and where the conversion from R_{JB} has not introduced unphysical effects (notably, upward curvature). This distance varies depending on the specific GMM, but is usually within 50–70 km. For large magnitudes, the original model data at very short distances was used, while for smaller magnitudes, the original data was typically limited to distances of 10–15 km and greater. The two functional forms are as follows:

$$\ln(GMIM) = c_1 + c_2 \ln(R_{RUP} + c_3) \tag{2.3}$$

$$\ln(GMIM) = c_1 + c_2 \ln(R_{RUP} + h)^{1/2} \tag{2.4}$$

where *GMIM* is the ground motion intensity measure (such as PGA, PGV, or PSA), h is a "fictitious depth" used for ground-motion saturation at close distances, and c_1, c_2, and c_3 are coefficients obtained from regression. For each GMM, the equation that best fits the predictions is selected.

2.2.2 Large-Distance Extrapolation (up to 1500 km)

For models that require extrapolation to R_{RUP} =1500 km, a single functional form is fit to the median predictions in a relatively large distance range where they are deemed usable, again where the geometric spreading term in the original model development is approximately constant and where the effects of Q appear to be physically reasonable. This distance varies depending on the specific GMM, but is usually beyond 400 km. The functional form for large distance extrapolation is provided by:

$$\ln(GMIM) = c_1 + c_2 \ln(R_{RUP}) + c_3 R_{RUP} \tag{2.5}$$

2.3 EXTRAPOLATION SPECIFIC TO EACH GMM

The following sub-sections summarize the process used to extrapolate the median GMMs. The GMM-specific constraints described below were developed through extensive interaction with each GMM development team. Issues discussed included close-in attenuation shape and whether or not to allow oversaturation and are reflected below. The intermediate and final extrapolated curves were all reviewed and approved by the GMM developers.

For most of the GMM extensions described below, figures are presented to illustrate the process. For a given frequency, the left panel shows the extension process, and the right panel shows the final extended model results. Each line in the plots corresponds to a specific magnitude. Most of the plots span a range from **M**4 or 4.5 to **M**8 or 8.2, with spacings of either 0.1 or 0.5 magnitude units. This variable set of lines was selected to highlight specific features of

the GMMs. Note that in all the plots provided below, ground-motion values at $R_{RUP} = 0$ km are plotted at $R_{RUP} = 0.1$ km.

2.3.1 Boore GMMs

The six original GMMs are documented in Chapter 2 of the previous PEER report [2015], with the original tables in the corresponding electronic appendices (2B-2G).

The R_{RUP} versions of the Boore GMMs require extrapolation to zero distance for the smaller magnitudes. This extrapolation was performed by fitting Equation (2.4) to the predictions for distances in the range of 15–65 km. The blue curves in Figure 2.5 show example results. As indicated on the figure, the conversion from R_{JB} to R_{RUP} and the process of extrapolation led to crossing of attenuation curves at small distances in which **M**4 predictions are larger than **M**8 predictions at distances less than a few kilometers (e.g., see left panel of Figure 2.6). In general, this occurred for higher frequency ground motions, especially those using an $R^{-1.3}$ geometrical spreading at short distances, such as B_a04 and B_ab14. Dr. Boore indicated that this is an unintended effect, and that the ground-motion predictions should increase monotonically with magnitude. To implement this intent, the following algorithm was applied to all the Boore GMMs (see example right panel of on Figure 2.6):

- The **M**8 are defined as the upper limit of ground motions for all lower magnitudes.
- Proceeding downward in **M** from **M**8 if the ground motions at zero distance (extended as described above) exceed those for larger magnitudes, they are capped at the predictions for the next largest magnitude; if not, they are retained.
- Having fixed the value at $R_{RUP} = 0$ from the previous step, the data in the distance range of 20–65 km was refit with Equation (2.4), applied with added constraint of the fixed value at zero distance. The fitted curves were adjusted to match the original predictions at 20 km. The results are the red curves shown on Figure 2.5.

For large distances, Equation (2.5) was fitted from predictions in the $R_{RUP} = 14$–1000 km range.

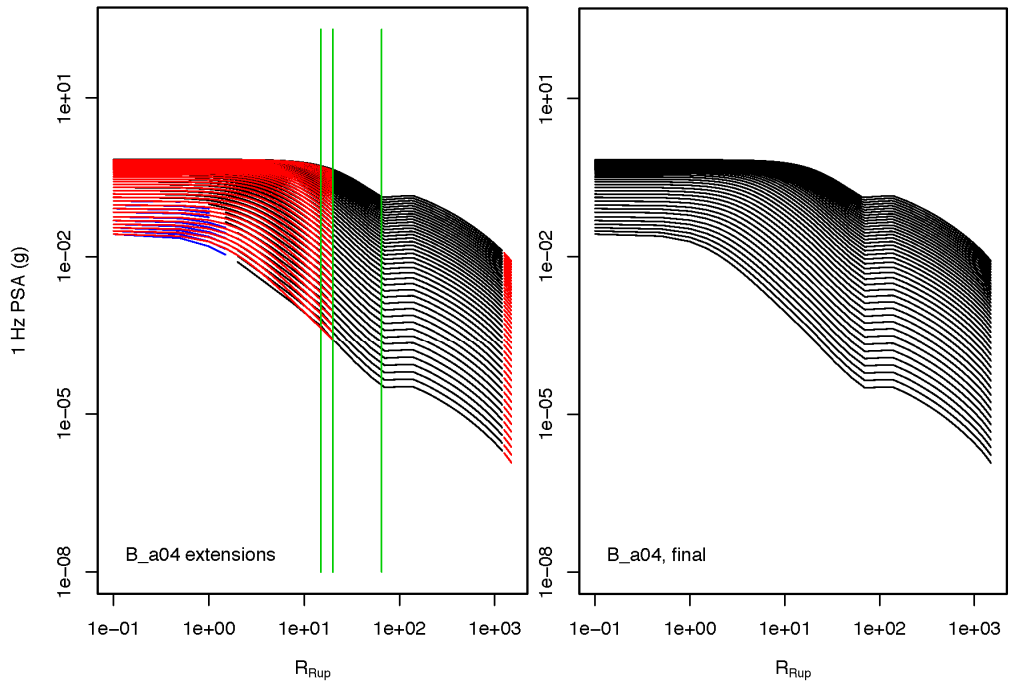

Figure 2.5 Distance extensions for the B_a04, 1Hz PSA. The left frame shows the extended regions in blue and red; the right frame shows the final model.

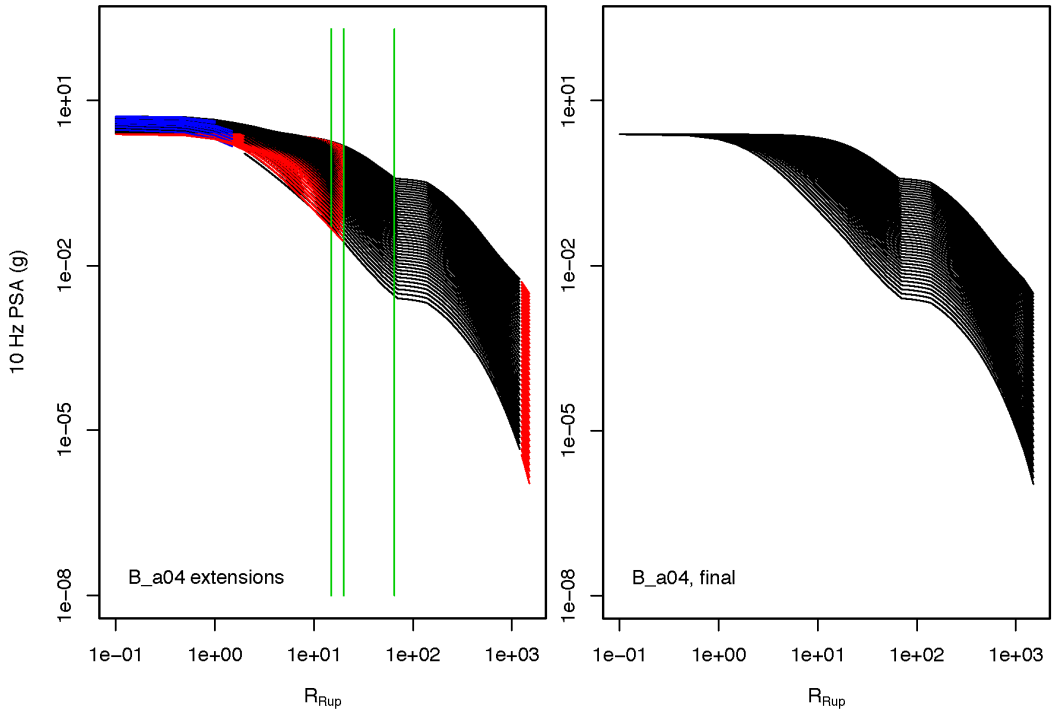

Figure 2.6 Distance extensions for the B_a04, 10 Hz PSA. The left frame shows the original predictions in black and the extended regions in blue and red; the right frame shows the final model. The right panel shows the results of the algorithm used to prevent the crossover.

2.3.2 Darragh, Abrahamson, Silva, and Gregor (DASG) GMMs

The four original GMMs are documented in Chapter 3 of the previous PEER report [2015], with the original tables in the corresponding electronic appendices (3C–3F).

The four GMMs in this suite already provide ground motions up to 1500 km and were converted from R_{JB} to R_{RUP}, as described in Section 2.1. The process used for short distances was to fit the data for individual magnitudes over the whole distance range using a combination of Equations (2.3) and (2.5). This model was then used to predict ground motions at distances less than the minimum provided. The red curves on the first plot for each frequency show the results: the solid red curves show the extrapolation, and the dashed red curves show the fitted model compared to the provided ground motions.

The predictions at short R_{RUP} were then scaled so that the prediction at the minimum distance provided by the developed model matched the value provided by the developer to remove any offset. For large magnitudes, the minimum distance provided by the developers was $R_{RUP} = 0.5$ km, and the fitted model matches the provided model very well over all distances. For smaller magnitudes, there is an upward curvature in the provided data at very short distances. These points with upward curvature were discarded. In order to maintain smooth model, the number of discarded distances increased for decreasing magnitude. Figure 2.7 shows an example of the process and final extrapolated model.

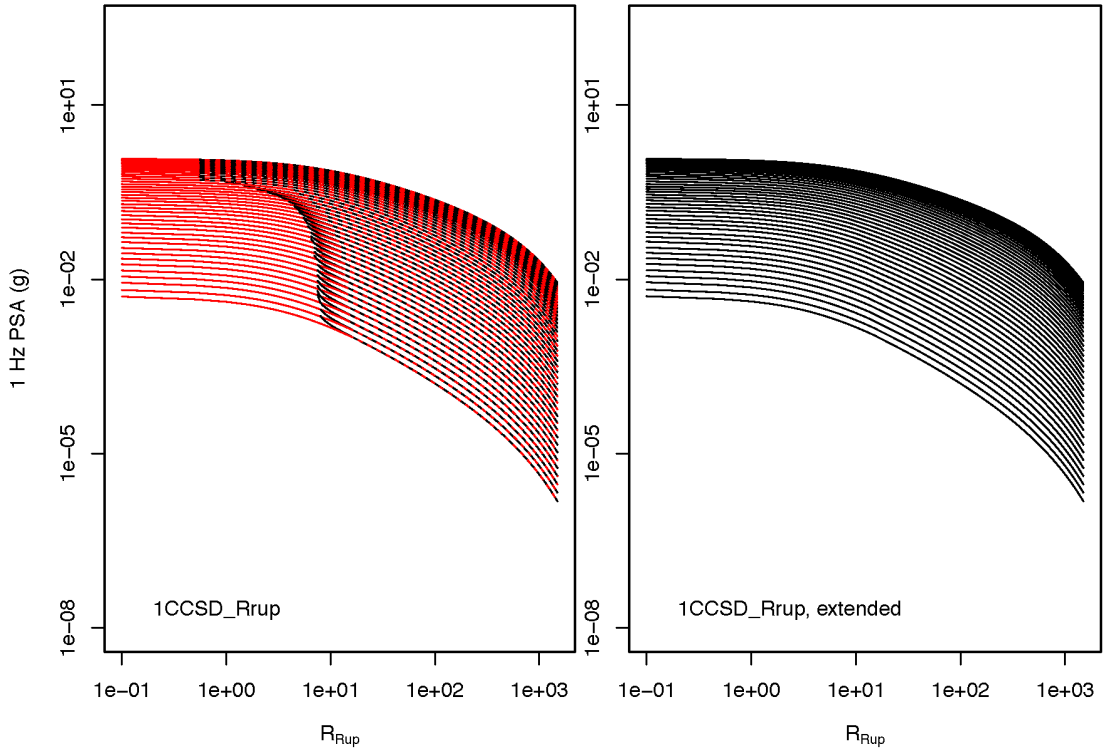

Figure 2.7 Distance extensions for the DASG 1CCSP GMM, 1 Hz PSA. The left frame shows the original predictions in black and the fitted model in red; the right frame shows the final model.

2.3.3 Yenier and Atkinson (YA15) GMM

The original GMM is documented in Chapter 4 of the previous PEER report [2015], with the original tables in the corresponding electronic appendix (4A).

This model is only defined up to 600 km. Figure 2.8 shows an example of extrapolation from 600 to 1500 km. For each frequency and each magnitude, the ground-motion values beyond 50 km (vertical green line) were fitted with Equation (2.5). The red dashed curves show the fit, and the red solid curves show the extrapolation. The extrapolated values were then scaled so that the value at 600 km predicted by the fitted model matched the value provided by YA15 at 600 km.

The YA15 model provided ground-motion values at R_{RUP} = 0 km for all magnitudes. However, for frequencies of 25 Hz and higher, the values for the lower magnitudes show kinks in the distance scaling at R_{RUP} < 15 km (see left pane of Figure 2.9), which are likely artifacts of the adjustments from R_{JB} to R_{RUP}; these adjustments were completed during the model development by Yenier and Atkinson These breaks were removed as follows (using the 25 Hz PSA as an example):

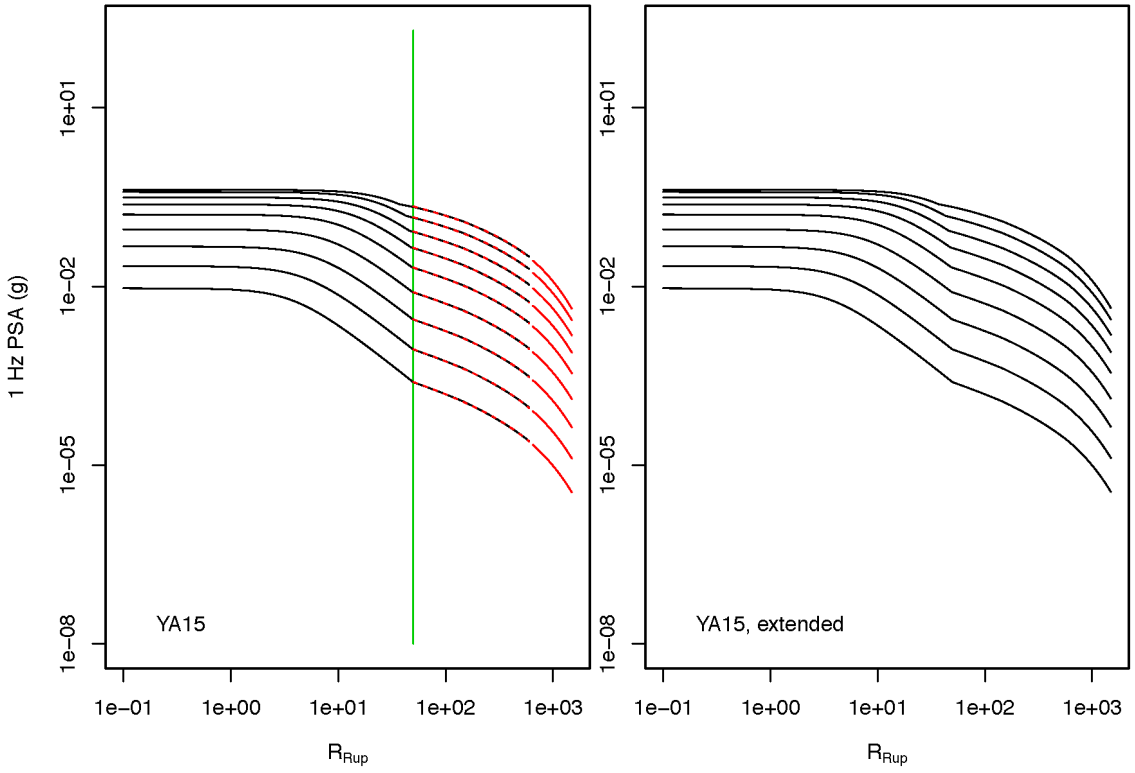

Figure 2.8 Large distance extensions for the YA15 GMM, 1 Hz PSA. The left frame shows the original predictions in black, and the green line shows the lower-bound limit of ground motions used to fit the model (in red); the right frame shows the final model.

- The highest frequency without the kinks is 20 Hz. Predictions for 20 Hz at R_{RUP} < 15 km were used as a template for the distance scaling at higher frequencies, using the predictions for **M**8.2 as the reference ground motions.
- The ratio of ground motions for any magnitude **M**(i), and the ground motions for **M**8.2 is computed at 15 km for 20 Hz PSA:

$$PSARatio_{20\text{Hz},15\text{km}}[\text{M}(i)] = \ln\left\{PSA_{20\text{Hz},15\text{km}}[\text{M}(i)] / PSA_{20\text{Hz},15\text{km},\mathbf{M}8.2}\right\} \quad (2.6)$$

An equivalent ratio can be computed using the 25 Hz ground motions:

$$PSARatio_{25\text{Hz},15\text{km}}[\text{M}(i)] = \ln\left\{PSA_{25Hz,15km}[\text{M}(i)] / PSA_{25\text{Hz},15\text{km},\mathbf{M}8.2}\right\} \quad (2.7)$$

Taking the ratio of Equations (2.7) and (2.6), we obtain a magnitude-scaling factor (MSF):

$$MSF_{25Hz}[\text{M}(i)] = \ln\left\{PSARatio_{25\text{Hz},15\text{km}}[\text{M}(i)] / PSARatio_{20\text{Hz},15\text{km}}[\text{M}(i)]\right\} \quad (2.8)$$

which provides the difference in magnitude scaling between 20 and 25 Hz.

- Then for each magnitude **M***(i)*< 8.2 and distance $R_{RUP}(j)$ less than 15 km, the ground motions are computed from the prediction for **M**8.2 as follows

$$PSA_{25\text{Hz}}[\text{M}(i), R_{RUP}(j)] = PSA_{25Hz}[\mathbf{M}8.2, R_{RUP}(j)] * \exp\left\{\ln\left[PSA_{20Hz}[\text{M}(i), R_{RUP}(j)] / PSA_{20\text{Hz},15\text{km},\mathbf{M}8.2}\right] * MSF_{25Hz}[\text{M}(i)]\right\} \quad (2.9)$$

The same computations are applied to frequencies above 25 Hz and to PGA. This process preserves the predictions for **M**8.2 and produces similar magnitude scaling at each distance less than 15 km, as that seen in the 20 Hz motions (Figure 2.9).

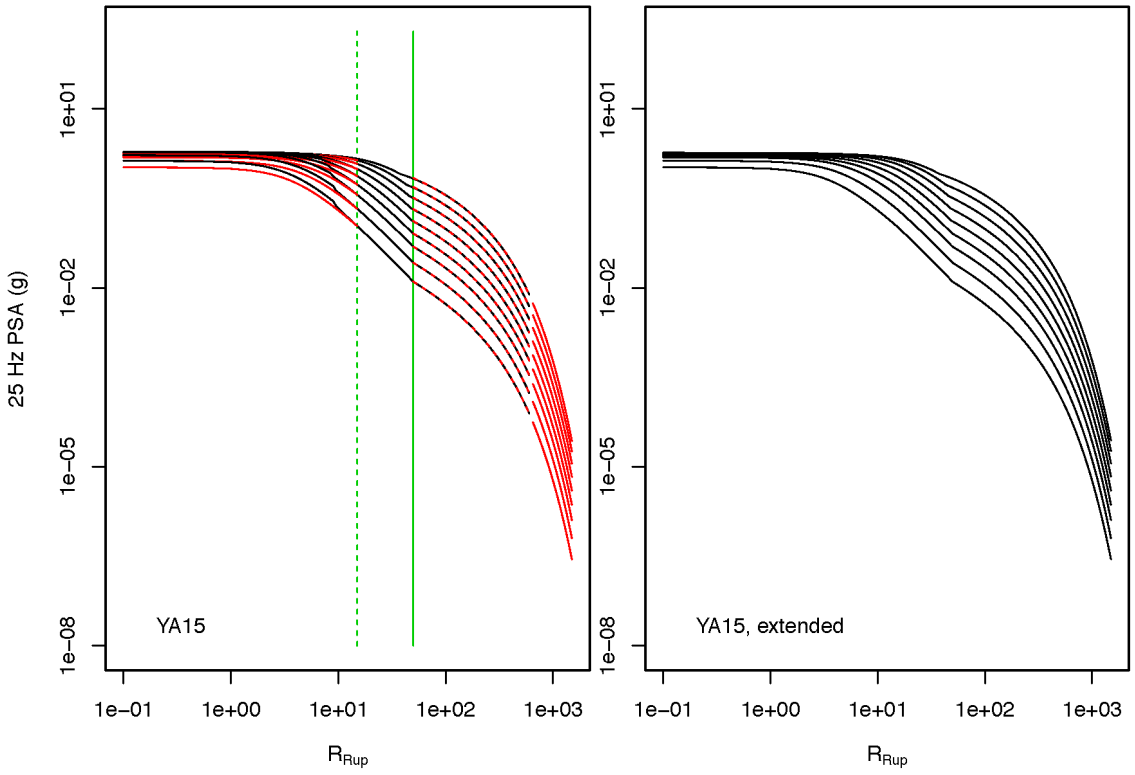

Figure 2.9 Illustration of short-distance correction [Equations (2.6)–(2.9)] for the 25 Hz PSA example of YA15. The left frame shows the original predictions in black, the dashed green line is anchored at 15 km, the solid green line shows the lower-bound limit of ground motions used to fit the model at large distances, and the red line shows the model; the right frame shows the final model, including the short distance corrections and the large distance extrapolations.

2.3.4 Pezeshk, Zandieh, Campbell, and Tavakoli (PZCT) GMMs

The two original GMMs are documented in Chapter 5 of the previous PEER report [2015], with the original tables in the corresponding electronic appendix (5A-5B).

Figure 2.10 shows the large-distance extrapolation from 1000 to 1500 km. For each frequency and each magnitude, the ground-motion values beyond 120 km (vertical green line) were fitted with Equation (2.5). The red dashed curves show the fit, and the red solid curves show the extrapolation. The extrapolated values were then scaled so that the value at 1000 km predicted by the fitted model matched the value provided by PZCT at 1000 km.

Although difficult to see on the left frame of Figure 2.10, there is some oversaturation at close distance for the upper magnitude range, which was not a feature intended by the GMM developers. The right frame in Figure 2.10 shows fewer curves, and one can see the adjustment applied at close distances to prevent oversaturation. This is achieved as follows: for each frequency, the magnitude curve that produces the highest ground motions at R_{RUP} = 0 km is identified as the upper-limit ground motions. Then starting in sequence with the next highest magnitude, the ground motions at each distance are taken to be the maximum of the values for

that magnitude and the magnitude below. In this way, full saturation is achieved. Both models were extrapolated using Equation (2.5) and the approach described above.

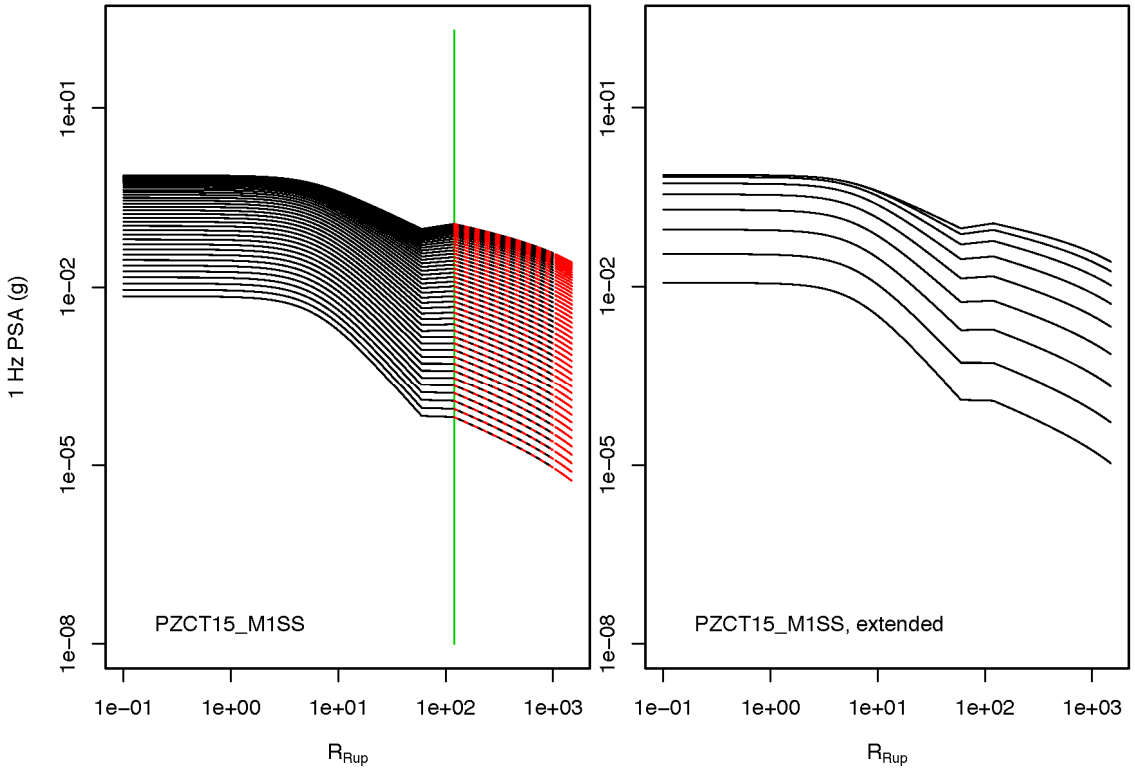

Figure 2.10 Large distance extrapolations for the PZCT_M1SS GMM, 1 Hz PSA. The left frame shows the original predictions in black, and the green line shows the lower-bound limit of ground motions used to fit the model (dashed red lines show the model fit and solid red lines show the extrapolations); the right frame shows the final model.

2.3.5 Frankel GMM

The original GMM is documented in Chapter 6 of the previous PEER report [2015], with the original tables in the corresponding electronic appendix (6A). The Frankel model is simulations-based and provided for a series of discrete magnitudes (4.5, 5.5, 6.5, 7.5, and 8.0) and distances. The final ground motion tables developed and documented in Chapter 6 of the previous PEER report [2015] are based on a suite of simulations with Z_{TOR} = 5 km. Following discussions with the developer, and in order to capture the effect of shallower ruptures for larger magnitudes, NGA-East opted to use a modified version of the GMM. The Frankel GMM, as used by NGA-East, is defined by the simulations for Z_{TOR} = 1 km for **M**≥7.5 and for Z_{TOR} = 5 km for all the other magnitudes.

The large distance extrapolation from 1000 to 1500 km was performed by fitting Equation (2.5) to the ground motions from the model in the 200–1000 km range. Because of the limited number of data points and their somewhat irregular nature, coefficient c_2 in Equation (2.5) was fixed at -0.5.

The following steps were taken for the extension to R_{RUP} = 0 km (see Figures 2.11 and 2.12):

- Fit the **M**7.5 and **M**8 ground motions for distances ≤ 10 km with Equation (2.4). Parameter h is set to a small value (0.2 km) that prevents singularity at R_{RUP} = 0 km while producing essentially a linear trend with ln(R_{RUP}).
- Case 1: the ground-motion value at R_{RUP} = 0 km for **M**7.5 is smaller or equal to the equivalent ground motion at **M**8:
  - Both ground-motions values are kept for R_{RUP} = 0 km (one value for each magnitude, as shown by green dots in Figure 2.11).
  - For each of the two magnitudes, use the fit to predict ground motions to obtain missing values for distances less than those provided by the developer (red dots in Figure 2.11).
- Case 2: the ground-motion value at R_{RUP} = 0 km for **M**7.5 is larger than the equivalent ground motion at **M**8:
  - Combining the data from both magnitudes and refit the data for distances ≤ 10 km with the added constraint that the ground motion R_{RUP} = 0 km is the same for both magnitudes (full saturation is shown as a single green dot in Figure 2.12).
  - For each of the two magnitudes, apply the constrained fit to the combined data to predict ground motions at all distances less than those provided by the developer (see red dots in Figure 2.12).
- For **M**6.5, 5.5, and 4.5, the ground motions at R_{RUP} < 5 km are computed as the extended values for **M**7.5 (from above) multiplied by the ratio of the predictions for **M**6.5, 5.5, or 4.5 divided by the prediction for **M**7.5 from the Z_{TOR} = 5 km simulations. In other words, the slope in ground motions from the **M**7.5 is applied to the lower magnitudes for R_{RUP} < 5 km. The results are shown by the red open circles in Figures 2.11 and 2.12.

The ground-motion values were then extrapolated to **M**4 and **M**8.2, and interpolated to fill-up the intermediate magnitudes and distances composing the table.

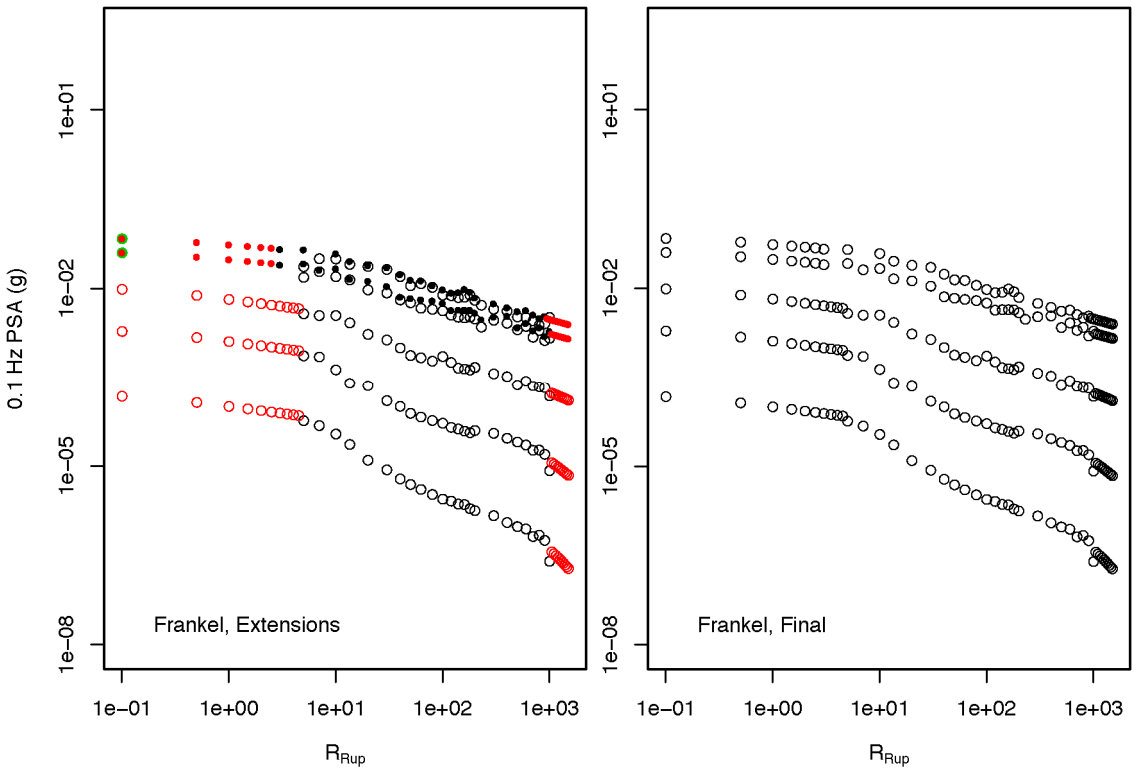

Figure 2.11 Extrapolation of Frankel GMM, 0.1 Hz PSA, Case 1 example. The left frame shows open black circles for Z_{TOR} = 5 km simulations, solid black circles for Z_{TOR} = 1 km simulations, green circles for ground motions extrapolated to R_{RUP} = 0 km for **M**7.5 and **M**8 and open red circles for the extrapolations (short and large distances); the right frame shows the final model.

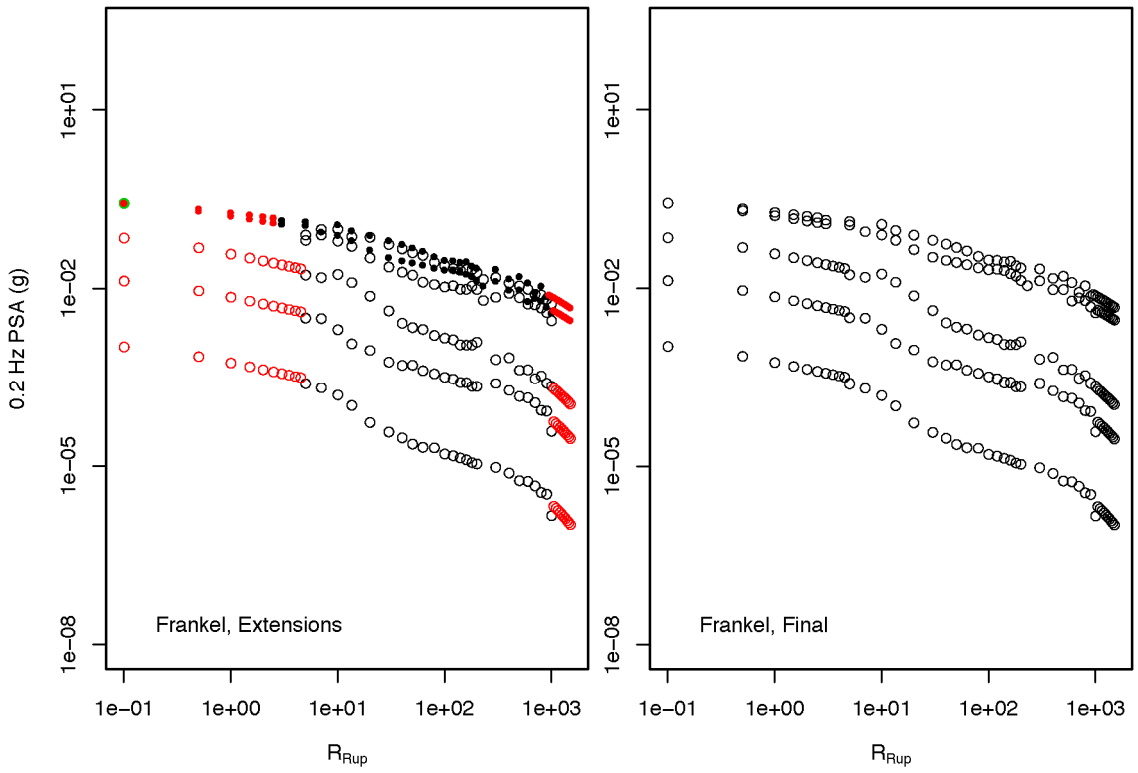

Figure 2.12 Extrapolation of Frankel GMM, 0.2 Hz PSA, Case 2 example. The left frame shows open black circles for Z_{TOR} = 5 km simulations, solid black circles for Z_{TOR} = 1 km simulations, green circles for ground motions extrapolated to R_{RUP} = 0 km for **M**7.5 and **M**8 and open red circles for the extrapolations (short and large distances); the right frame shows the final model.

2.3.6 Shahjouei and Pezeshk (SP15) GMM

The original GMM is documented in Chapter 7 of the previous PEER report [2015], with the original tables in the corresponding electronic appendix (7B).

Before SP15 GMM was extrapolated, it was first converted from R_{JB} to R_{RUP}, as described in Section 2.1. Figure 2.13 shows the extrapolation from 1000 to 1500 km. For each frequency and each magnitude, the ground-motion values beyond R_{RUP} = 120 km (vertical green line) were fitted with Equation (2.5). The red dashed curves show the fit, and the red solid curves show the extrapolation. The extrapolated values were then scaled so that the value at R_{RUP} = 1000 km predicted by the fitted model matched the value provided by SP15 at 1000 km.

Also shown on Figure 2.13 is the extrapolation from the minimum R_{RUP} provided by SP15 to R_{RUP} = 0 km. This is performed assuming that there is no change in amplitude at R_{RUP} values smaller than the smallest R_{RUP} provided by SP15.

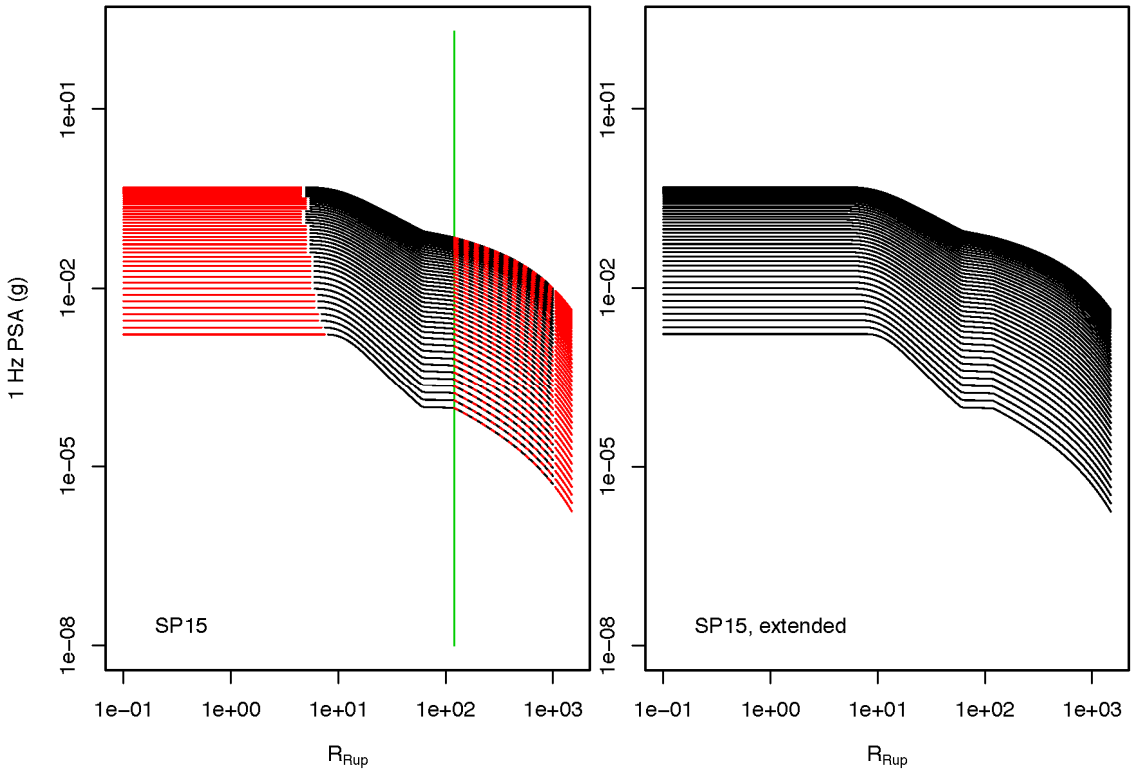

Figure 2.13 Extrapolation of SP15 GMM, 1 Hz PSA. The left frame shows the original predictions in black, and the green line shows the lower-bound limit of ground motions used to fit the model at large distances (dashed red lines show the model fit and solid red lines show the extrapolations); the right frame shows the final model.

2.3.7 Al Noman and Cramer (ANC) GMM

The original GMM is documented in Chapter 8 of the previous PEER report [2015], with the original tables in the corresponding electronic appendix (9A). This GMM was not deemed ready for use in the NGA-East project, and ground motions were not extrapolated. For completeness, we provide the same ground-motion table that was published with the original GMM report. Figure 2.14 shows the distance scaling for 1 Hz PSA.

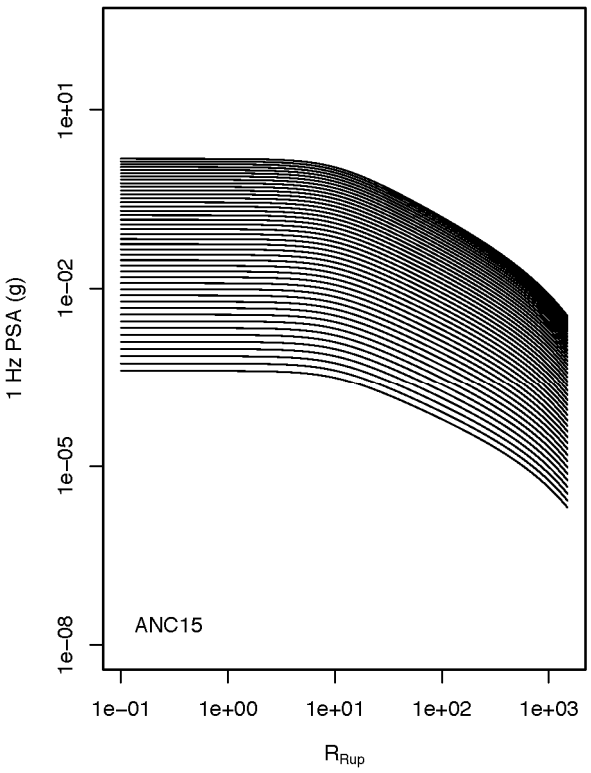

Figure 2.14 AND15 GMM ground motions for 1 Hz PSA. The model has not been extrapolated.

2.3.8 Graizer GMM

The original GMM is documented in Chapter 9 of the previous PEER report [2015], with the original tables in the corresponding electronic appendix (9A). Median ground motions were provided for the complete distance range and did not require extrapolations (Figure 2.15). For completeness, we provide the same ground-motion table that was published with the original GMM report.

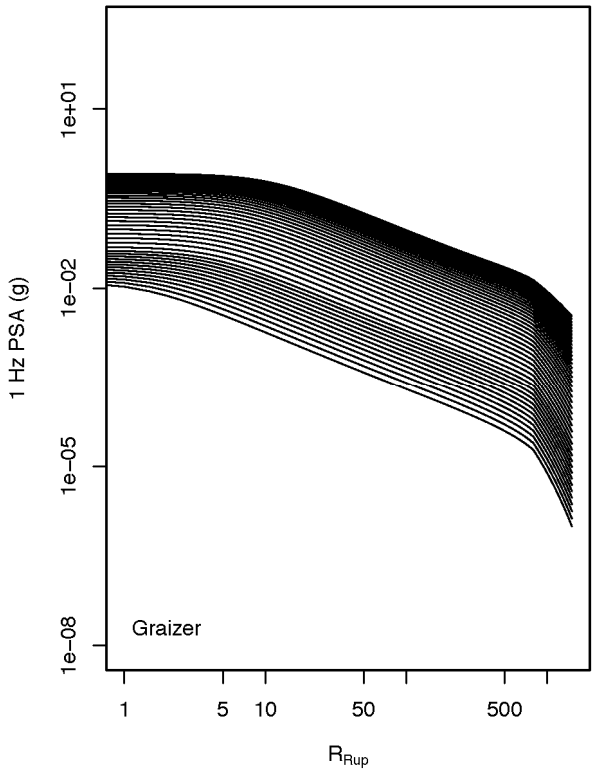

Figure 2.15 Graizer GMM ground motions for 1 Hz PSA. The model has not been extrapolated and is used as-is over the full distance range.

2.3.9 Hassani and Atkinson (HA15) GMM

The original GMM is documented in Chapter 10 of the previous PEER report [2015], with the original tables in the corresponding electronic appendix (10A).

Before HA15 GMM was extrapolated, it was first converted from R_{JB} to R_{RUP}, as described in Section 2.1. Figure 2.15 shows an example of extrapolation. Starting with **M**8, the curves for **M**8 to **M**6.9 from the HA15 results were extended from R_{RUP} = 0.5 km to R_{RUP} = 0 km, using a fit to Equation (2.4), with the ground motions for each magnitude capped by the predictions for the next largest magnitude.

After capping, predictions for **M**6.9 were fitted with Equation (2.4) to obtain the value of h for **M**6.9. For **M**6.8 and lower, h was set using the following equation from YA15:

$$h = h(\mathbf{M}6.9) * 10^{0.235*(\mathbf{M}-6.9)} \tag{2.10}$$

Equation (2.4) was fitted against (for each magnitude below 6.8), using the h obtained with Equation (2.10) and the ground motions for R_{RUP} values between 20 and 50 km. The resulting fitted model was extrapolated back to R_{RUP} = 0 km, capping the predictions with those for the next highest magnitude (Figure 2.16).

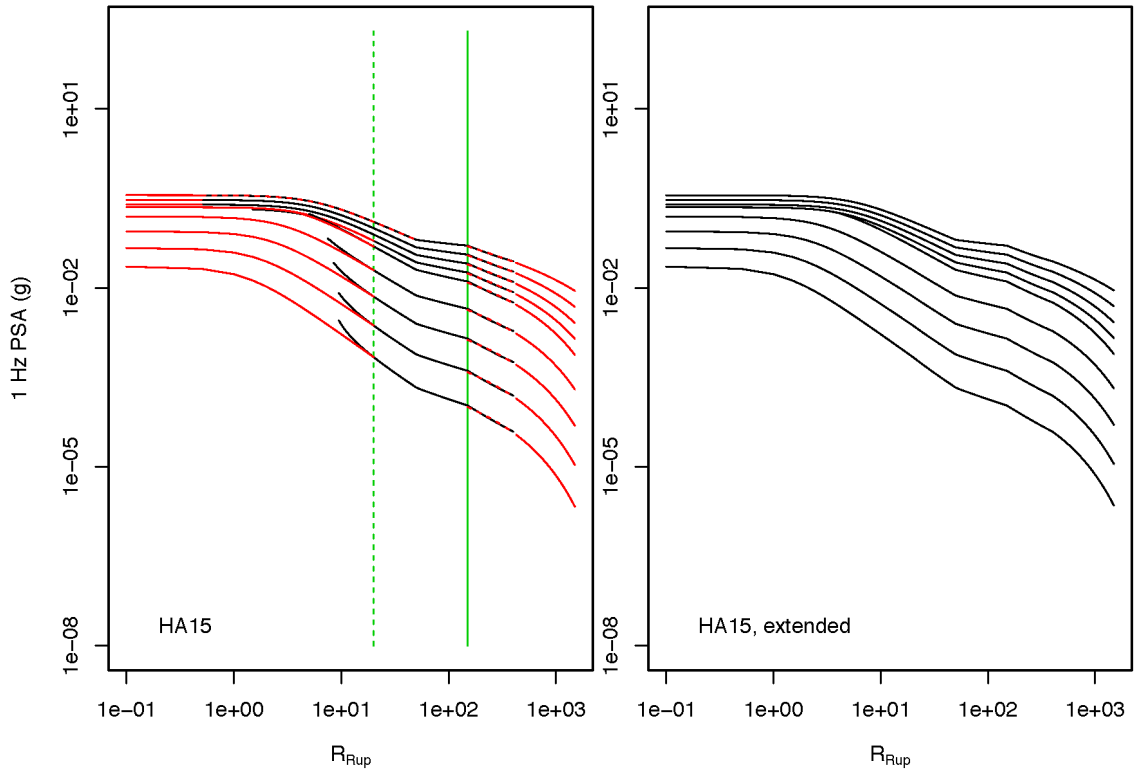

Figure 2.16 Illustration of extrapolation for the HA15 GMM, PSA 1 Hz. The left frame shows the original predictions in black, the dashed green line is anchored at 20 km, the solid green line shows the lower-bound limit of ground motions used to fit the model at large distances (anchored at 120 km), and the red lines show the model; the right frame shows the final model.

2.3.10 PEER GMMs

The two original GMMs are documented in Chapter 11 of the previous PEER report [2015], with the original tables in the corresponding electronic appendix (11A-11B).

For both PEER GMMs, ground-motion predictions beyond 400 km were discarded, and the ground-motion values in the 140 to 400 km R_{RUP} range were fitted with Equation (2.5). The fitted model was adjusted to match the ground motions at R_{RUP} = 400 km and then used to extrapolate to 1500 km. The ground-motion values for R_{RUP} < 10 km were discarded, and those in the distance range of 10 to 50 km were fitted by Equation (2.4). The fitted model was scaled to match the ground motions at 10 km and used to extrapolate to R_{RUP} = 0 km. Some degree of oversaturation was allowed for higher frequency ground motions, as provided by the fitted model. Figure 2.17 illustrates the extrapolation scheme.

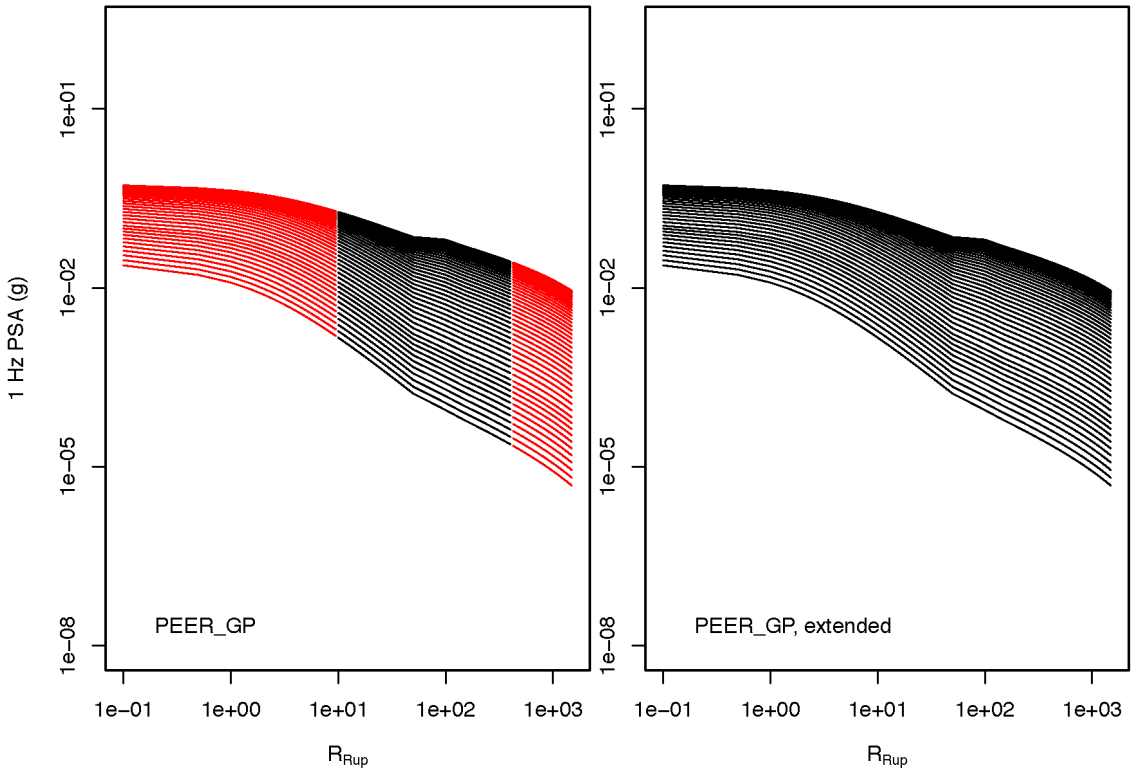

Figure 2.17 Illustration of extrapolation for the PEER_GP GMM, PSA 1 Hz. The left frame shows the original predictions in black and the extrapolations in red; the right frame shows the final model.

2.4 SPECTRAL-SHAPE ADJUSTMENTS

The adjustment of the GMMs to large distances was performed independently for each frequency. This can lead to an unphysical spectrum at large distances, with a trough at high frequencies beyond the peak of the spectrum. This observation was also made for some of the initial NGA-East GMMs (before extrapolation) and was noticed for large distances in some of the NGA-West2 GMMs (R. Youngs and N. Abrahamson, *personal communication*). Examples are shown for the 1CCSP and the PEER_GP models (blue lines in Figure 2.18 and 2.19). This effect is not observed for all models, but when it occurs, it is typically for distances larger than 400 km (specific range is model dependent).

To correct these unphysical spectra, the high-frequency part is essentially replaced by a linear trend. If there is a trough at frequencies beyond the peak, the high-frequency ground-motion values are fixed to a specific value, following two possible cases. If there is a secondary peak beyond the trough, then the ground-motion values are fixed at the geometric mean of the trough value and the secondary peak value (Figure 2.18). Otherwise, the spectrum is fixed at the geometric mean of the trough value and the PGA value (anchored at 200 Hz in the plots, for illustration), as shown in Figure 2.19. After the distance extrapolation is completed, the process is applied systematically to all the spectra from all the GMMs.

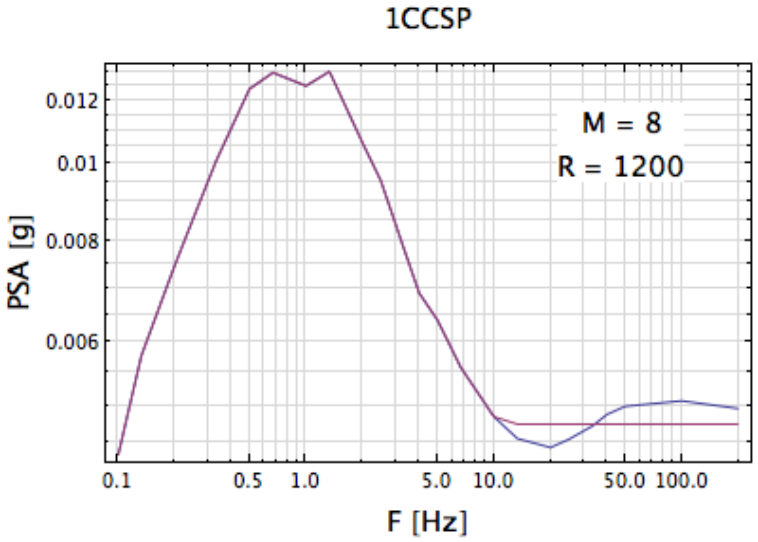

Figure 2.18 Example of spectral-shape correction showing the 1CCSP spectrum for **M**8 and R_{RUP} = 1200 km. The blue line is the original spectrum showing a trough-and-peak pair at high frequencies. The purple line shows the adjusted spectrum.

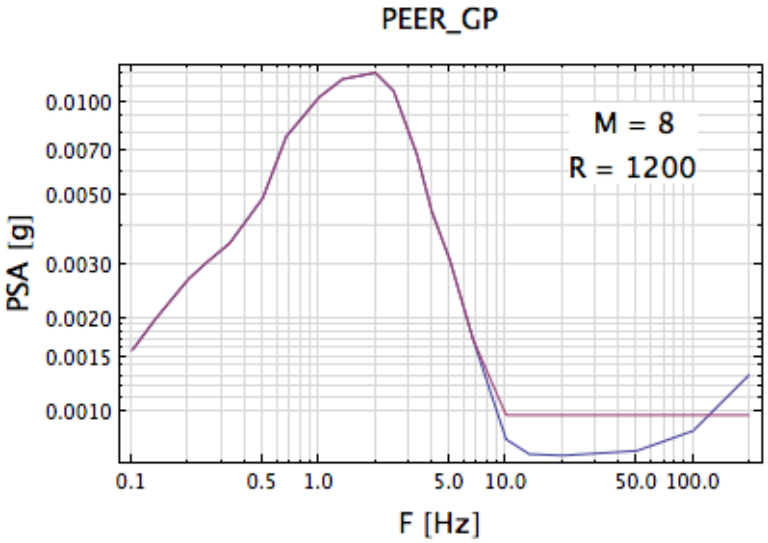

Figure 2.19 Example of spectral-shape correction showing the PEER_GP spectrum for **M**8 and R_{RUP} = 1200 km. The blue line is the original spectrum showing a trough at high frequencies. The purple line shows the adjusted spectrum.

3 Adjustment for Source Depth

Justin Hollenback

Christine A. Goulet

Pacific Earthquake Engineering Research Center
University of California, Berkeley

David M. Boore

U.S. Geological Survey
Menlo Park, California

3.1 INTRODUCTION

The scaling of PSA, PGA, and PGV with source depth was not specifically addressed in the previous PEER report [2015]. Of the ten developers who provided ground motions for the NGA-East project, only two (YA15 and PEER) included a focal-depth dependence of the motions as a fundamental part of their methodology. The motions provided by those developers were for nominal focal depths, however, and did not include a depth variable (such as focal depth or the depth to the top of rupture Z_{TOR}). Frankel has shown that there is a significant depth dependence for longer period motions (see Figure 3.1), which he attributes to the excitation of surface waves for shallow sources. But short-period motions in his model were obtained from stochastic model simulations, which use a depth-independent stress parameter and therefore have no depth dependence.

Empirical evidence suggests that the scaling of ground-motion intensity measures with source depth may be a non-negligible effect. Section 3.2.1 discusses empirical evidence of a relationship between source depth and stress parameter. Section 3.2.2 discusses how a relationship between stress parameter and source depth would affect the forward computations of ground motions; and Section 3.3 discusses the development of a simple scaling model for application to the NGA-East Median GMMs.

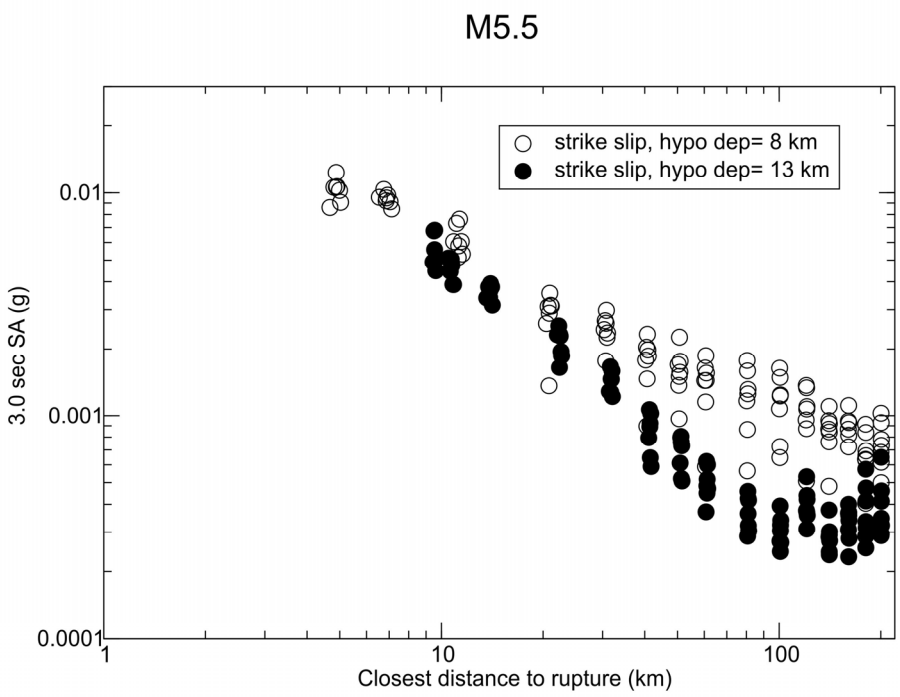

Figure 3.1 Taken from Frankel in PEER [2015], Chapter 6, Figure 6.9: 3.0-sec PSA values from two of the **M**5.5 simulations showing the effect of changing the depth of the rupture.

3.2 DEPTH AND STRESS PARAMETER FROM CENA DATA[+]

This section consists of two distinct parts. The first part looks at stress parameters obtained by several teams in the NGA-East Project from inversions of data. One team (YA15) found a depth dependence to the stress parameter of earthquakes, particularly for depths less than about 10 km. This depth dependence is largely driven by shallow natural events and by shallow potentially-induced earthquakes (PIEs); both types of events have relatively low stress parameters. There is a slight suggestion of a weaker dependence of stress with depth for depths greater than 10 km from independent work of Boatwright (not one of the GMM developers, *personal communication*). Guided by these studies, as well as that of DASG, we constructed a depth-dependent stress parameter model and then performed simulations to make quantitative assessments of the differences in ground motions for events of varying **M** at different depths. For small events, we find that the depth dependence of stress at depths less than 10 km leads to a depth scaling of ground motions that is much larger than the depth dependence in the PEER NGA-East models or several NGA-West2 models. Averaging the depth-dependent stress over a fault width, however, decreases the depth-dependence of motions for larger events, and then the results are in better agreement with those from NGA-West2 models.

[+] This section was written by David M. Boore

3.2.1 Depth-Dependence of the Stress Parameter: Evidence from Data Inversion Exercises

DASG and YA15 inverted stress parameters for CENA earthquakes. In addition, Dr. Boatwright provided a spreadsheet with stress parameters for CENA earthquakes [*personal communication*, 2014 and 2015]. In this section we summarize the results of these three studies.

YA15's Derived Stress Parameters

It is well known (e.g., Boore et al. [2010] and Boore [2012]) that stress parameters ($\Delta\sigma$) derived from the absolute values of either Fourier amplitude spectra (FAS) or PSA at certain frequencies or periods can be quite sensitive to the model parameters used to predict the amplitudes of the FAS or PSA. In particular, different attenuation models (geometrical spreading and anelastic attenuation) can lead to very different stress parameters when inverting motions from the same dataset (e.g., see Chapter 2 in the previous PEER report [2015]). To overcome this dependence, YA15 determined $\Delta\sigma$ by fitting the shape of the response spectra, not the absolute levels. In essence, this determined the corner frequency from which $\Delta\sigma$ can be derived.

The hypocentral depth (Z_{HYP}, H_{hypo}) and magnitude dependence of the events analyzed by YA15 are shown in Figure 3.2. They used events from all but the Gulf Coast region, and they include PIEs in their equation for $\Delta\sigma$ as a function of focal depth and magnitude. In Figure 3.2, tectonic (or natural) events are distinguished from PIEs, and for both cases, events for which their derived $\Delta\sigma$ is less than and greater than 200 bars are also plotted using different symbols (this is close to the median stress of 212 bars for natural events).

One thing that is clear from Figure 3.2: PIEs are generally small, shallow, and have $\Delta\sigma$ less than 200 bars. It is worth noting, however, that a number of naturally occurring events are also small, shallow, and have $\Delta\sigma$ less than 200 bars. There are few events with **M** > 5, and of those, all of the natural events have focal depths greater than 10 km and $\Delta\sigma$ greater than 200 bars.

YA15 included PIEs in their analysis. They found a small magnitude dependence to $\Delta\sigma$ (Figure 3.3) and a larger dependence of $\Delta\sigma$ on focal depth (Figure 3.4). The depth dependence of $\Delta\sigma$ is driven both by natural events and PIE events. Both types of events have similar $\Delta\sigma$'s for the same focal depth.

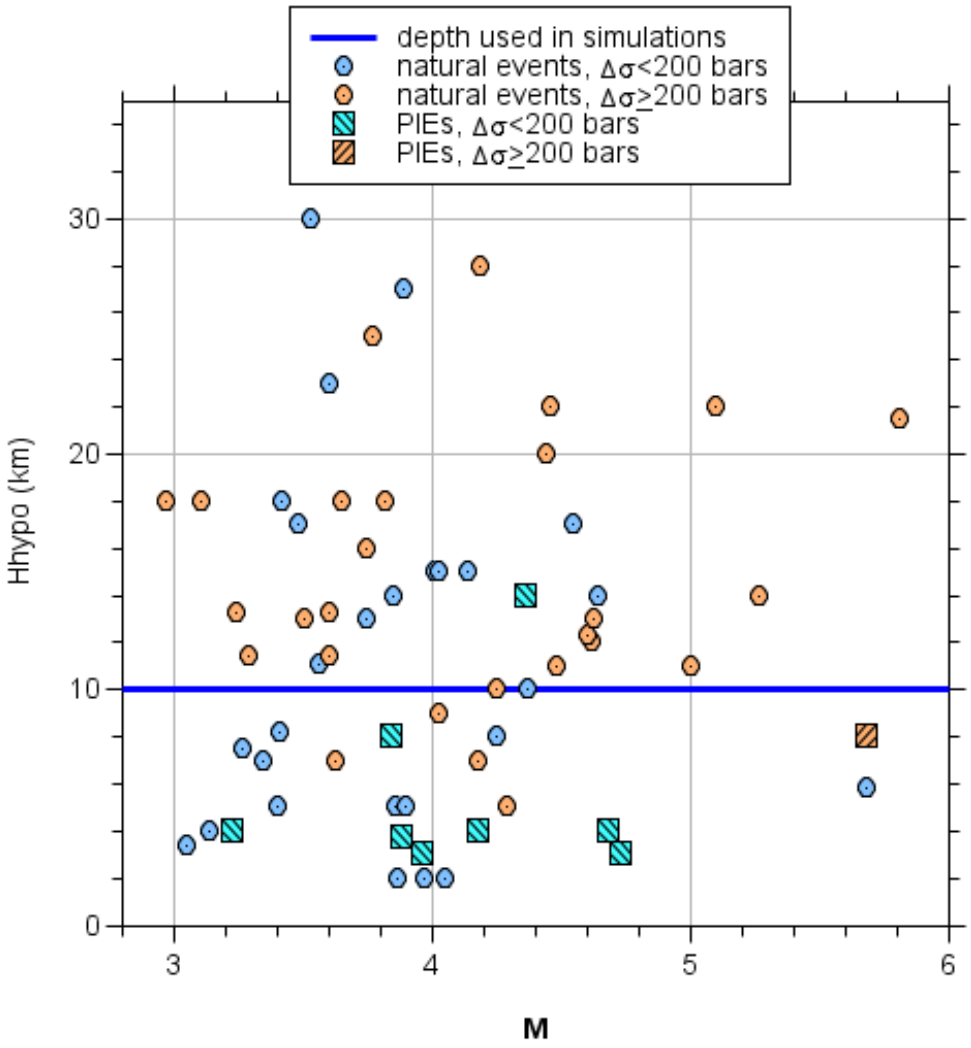

Figure 3.2 Magnitude-depth distribution of events for which YA15 determined stress parameters. The heavy blue line indicates the depth used in deriving the ground motions provided to the NGA-East project.

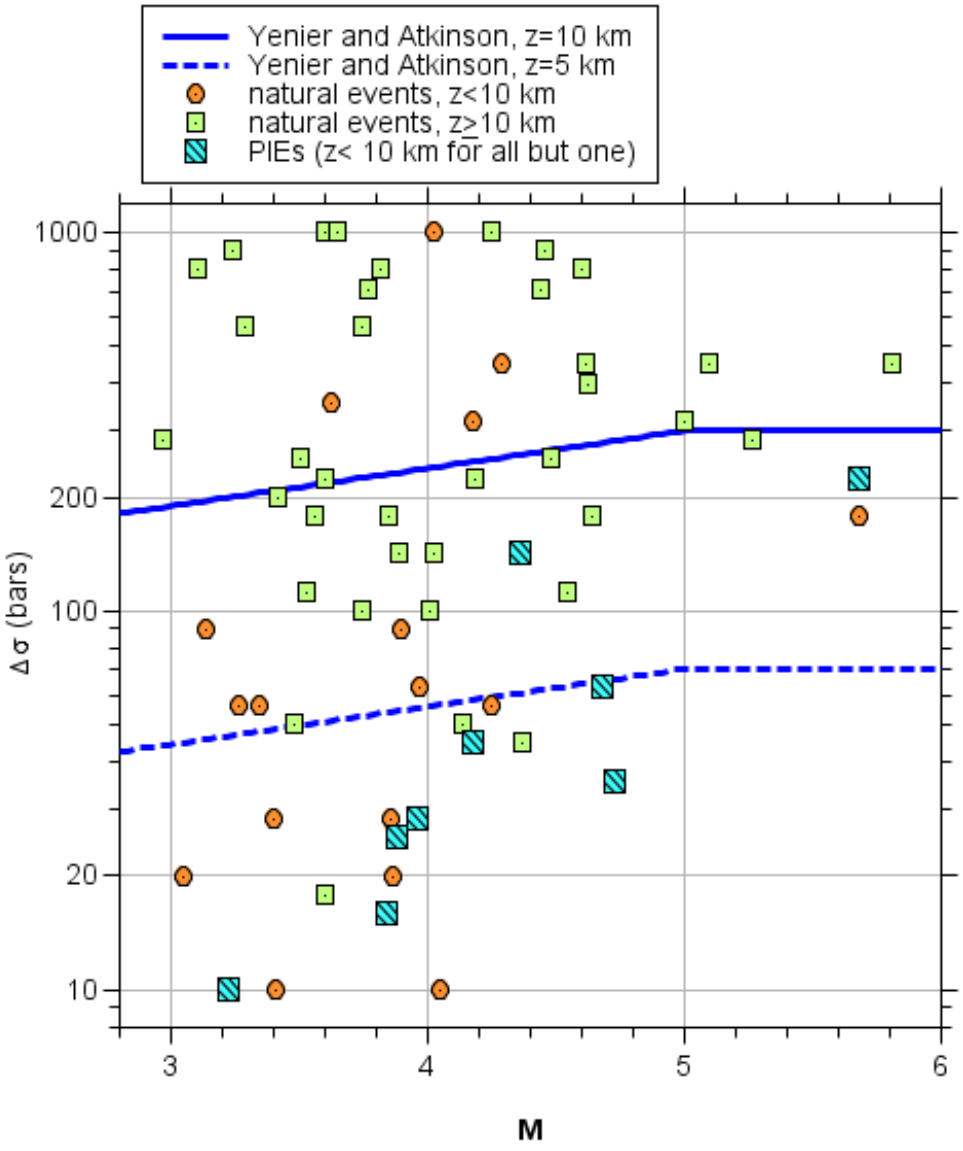

Figure 3.3 YA15 stress parameters as a function of magnitude. The lines are their equations.

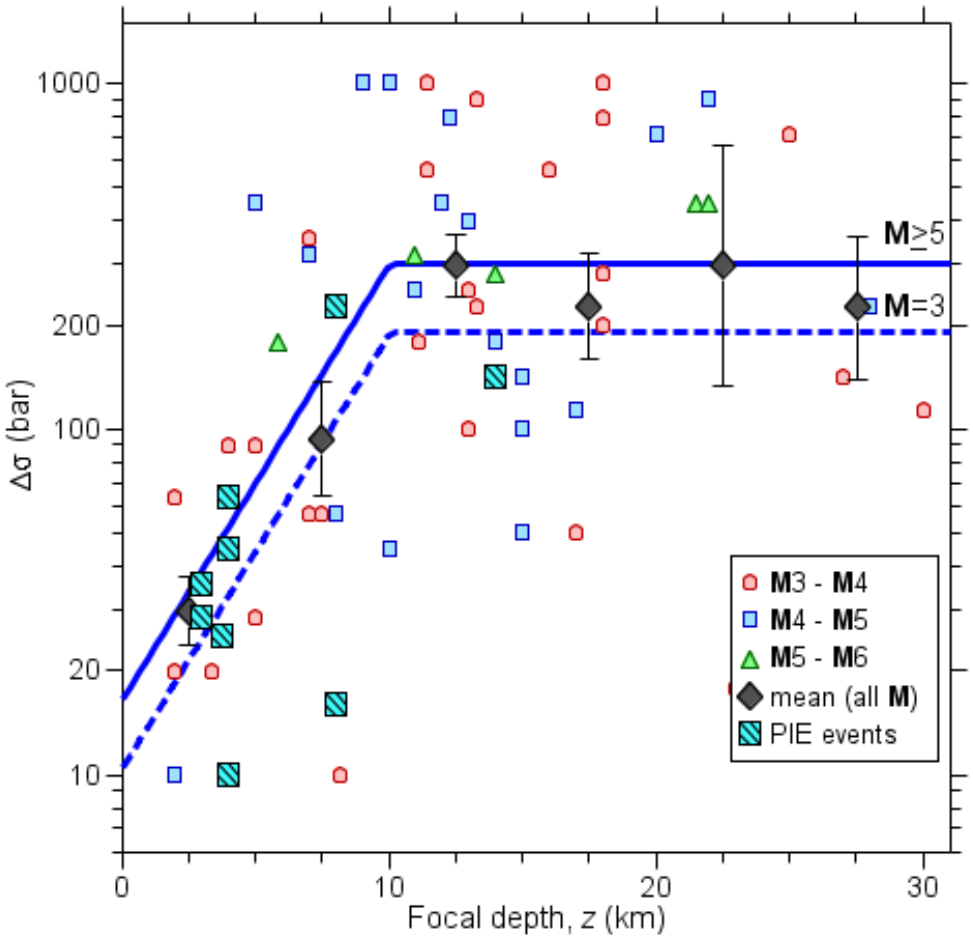

Figure 3.4 YA15 stress parameters as a function of focal depth. The lines are their equations.

Boatwright's Derived Stress Parameters

Dr. Boatwright provided spreadsheets containing the results of his analyses of a number of events in CENA [*personal communication*]. It is our understanding that he determined $\Delta\sigma$ by fitting both the shape of the FAS to determine the corner frequency, from which he determined $\Delta\sigma$. Figure 3.5 shows the magnitude-focal depth distribution of the events he used.

Boatwright's analysis of events was more restrictive than YA15 (DASG). He used events from southeastern Canada and northeastern U.S. He used no PIEs, and he subdivided the events into three regions, as indicated in Figure 3.5. The overall distribution with magnitude is about the same for the three regions, with eastern Quebec having a few more small magnitude events. Note that all but one of the northeastern U.S. events has focal depths less than 10 km; in contrast, most of the events in Quebec occur at depths greater than 10 km. This means that if there are regional differences in stress, it will be difficult to draw definitive conclusions about the depth variation of $\Delta\sigma$ for events in regions for which the depths do not span a large range.

There is little or no support in Figure 3.6 for a magnitude dependence in Quebec similar to that found by either YA15 or by DASG. Indeed, the results for events in eastern Quebec with depths greater than 10 km suggest a decrease, rather than an increase, of $\Delta\sigma$ with magnitude. The results for northeastern U.S. are somewhat scattered, but they could be taken as being broadly consistent with the YA15 and DASG magnitude dependence of $\Delta\sigma$. The distribution of $\Delta\sigma$ with focal depth is shown in Figure 3.7.

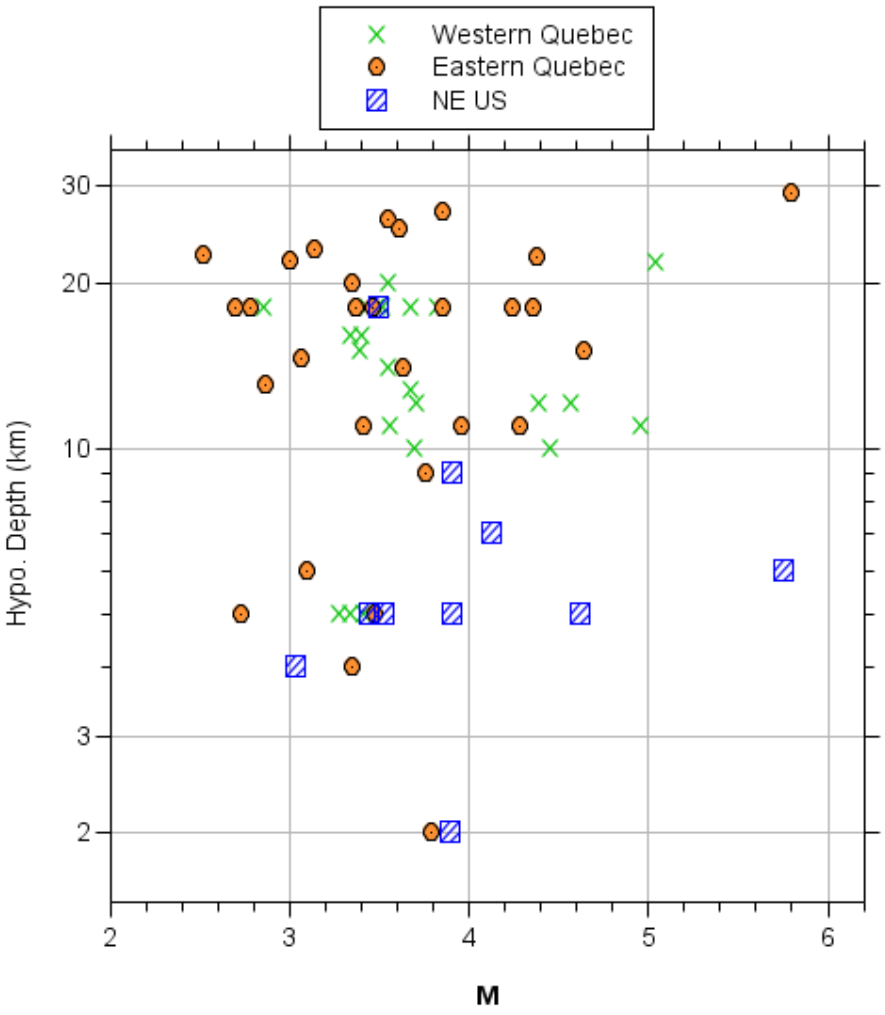

Figure 3.5 Magnitude-depth distribution of events for which Boatwright determined stress parameters.

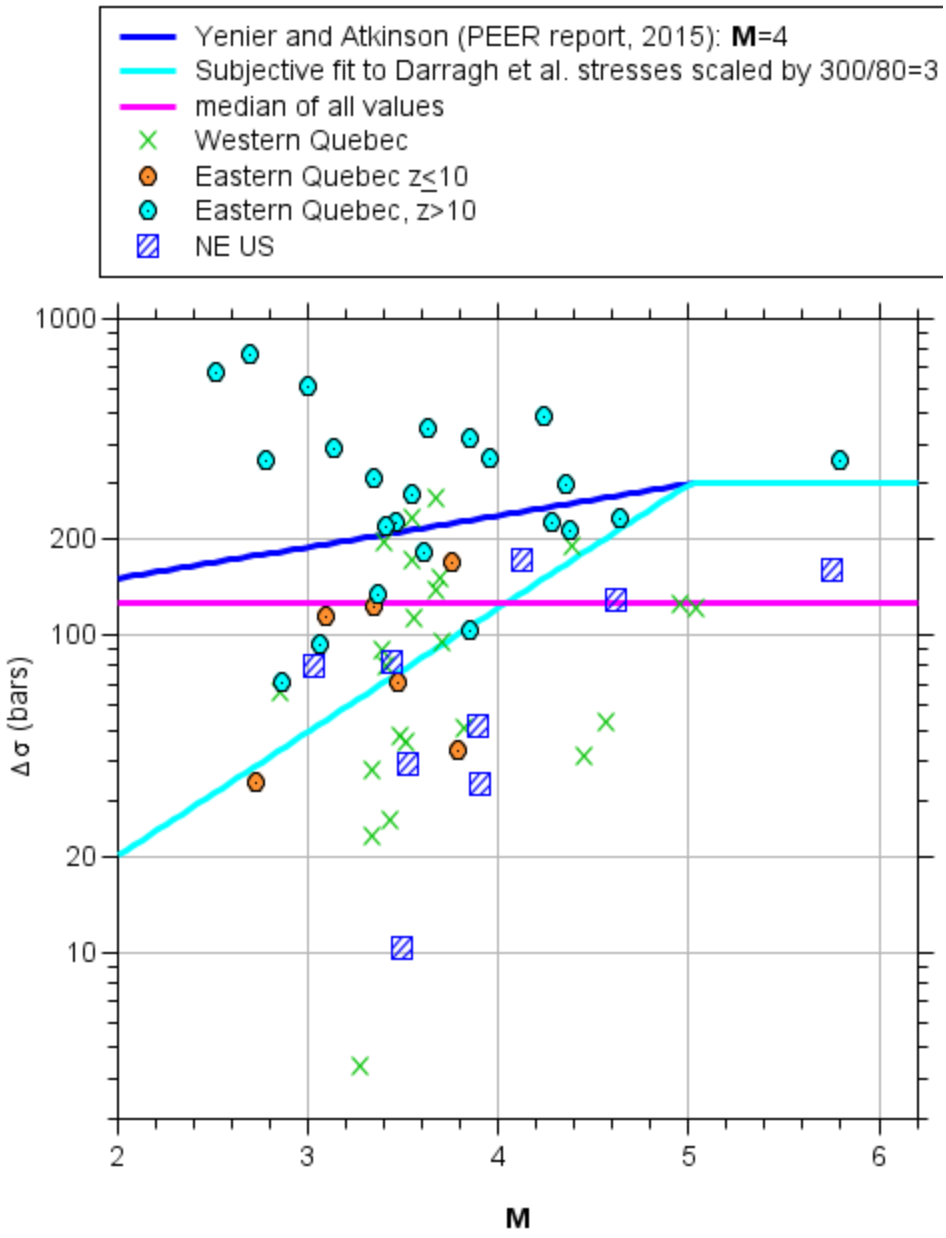

Figure 3.6 Boatwright's stress parameters as a function of magnitude. The eastern Quebec points are subdivided into events with focal depths less than and greater than 10 km. The lines are from Yenier and Atkinson for **M** = 4 and a subjective fit by David Boore to DASG values (see Section 3.2.2).

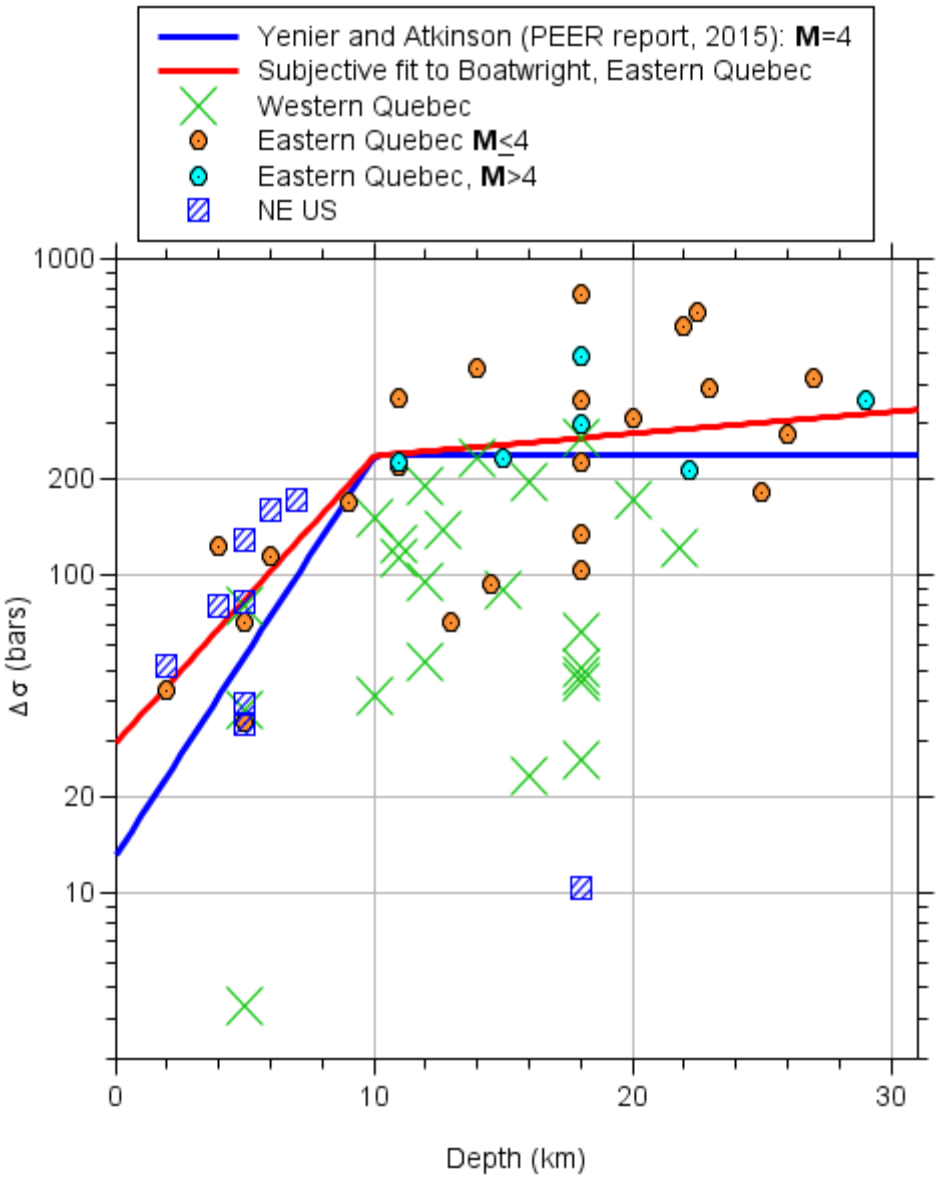

Figure 3.7 Boatwright's stress parameters as a function of focal depth. The eastern Quebec points are subdivided into events with magnitudes less than and greater than 4. The western Quebec symbols have been enlarged so that two of the values at a depth near 5 km can be seen. The lines are from Yenier and Atkinson for **M** = 4 and a subjective fit by David Boore to Boatwright's values.

The most striking results in Figure 3.7 are the low values of $\Delta\sigma$ for events in western Quebec. We note that none of the developers of GMMs for the NGA-East project have subdivided southeastern Canada as was done by Boatwright, and thus the regional differences shown in Figure 3.7 will be mapped into increased scatter in the stresses inverted from the NGA-East data by others. For depths less than 10 km, the northeastern U.S. and the eastern Quebec $\Delta\sigma$ are consistent with one another and also suggest a depth dependence similar to that found by YA15. It is interesting to note that the absolute levels of $\Delta\sigma$ as well as the trends with depth for the two studies are similar to one another, although the distance attenuation functions are quite different. This is contrary to what David Boore found in his own inversions (see Chapter 2 in the previous PEER report [2015]). This may be a result of both studies relying on spectral shape to determine corner frequencies from which $\Delta\sigma$ are derived. One other point: given the obvious regional differences of $\Delta\sigma$ in Quebec, it could be that the similarity of $\Delta\sigma$ for shallow events in northeastern U.S. and eastern Quebec is a coincidence. If so, this removes some support for the apparent depth dependence of $\Delta\sigma$.

DASG's Derived Stress Parameters

Darragh et al. (DASG) used data from Region 2 to determine their stress parameters. They fit the shape and the absolute levels of FAS to find simultaneously many of the model parameters, including source, path, and site parameters. Interestingly, they find a much lower κ (0.005 sec) for BC sites than used by YA15 (0.025 sec) (and perhaps by Boatwright, but this has not been verified). This may be a partial explanation for the large differences, shown later, in the absolute values of $\Delta\sigma$ found by DASG, compared with those found by the other two studies (whose values of $\Delta\sigma$ are similar to one another). The magnitude—focal depth distribution of the events used by DASG—is shown in Figure 3.8.

The most obvious feature in Figure 3.8 is that the majority of the events at depths less than 10 km are from PIEs. There is not an obvious correlation of focal depth and **M** for either the natural events or the PIEs. The similar H_{HYPO} distribution for natural events for stress parameter less than and greater than 20 bars suggests that there is not a strong dependence of $\Delta\sigma$ on focal depth (see later plot). (A note on notation: SP is the term used by DASG for the stress parameter; for consistency with the previous figures, we use $\Delta\sigma$ in the plots.) However, the events with $\Delta\sigma$ less than 20 bars are generally for small **M**, suggesting an **M** dependence of $\Delta\sigma$. This is shown in Figure 3.9.

Also, note that the events are not centered in the depth range used in the simulations. But excluding the PIEs, there does not appear to be a strong depth dependence to $\Delta\sigma$, so maybe this is not an issue.

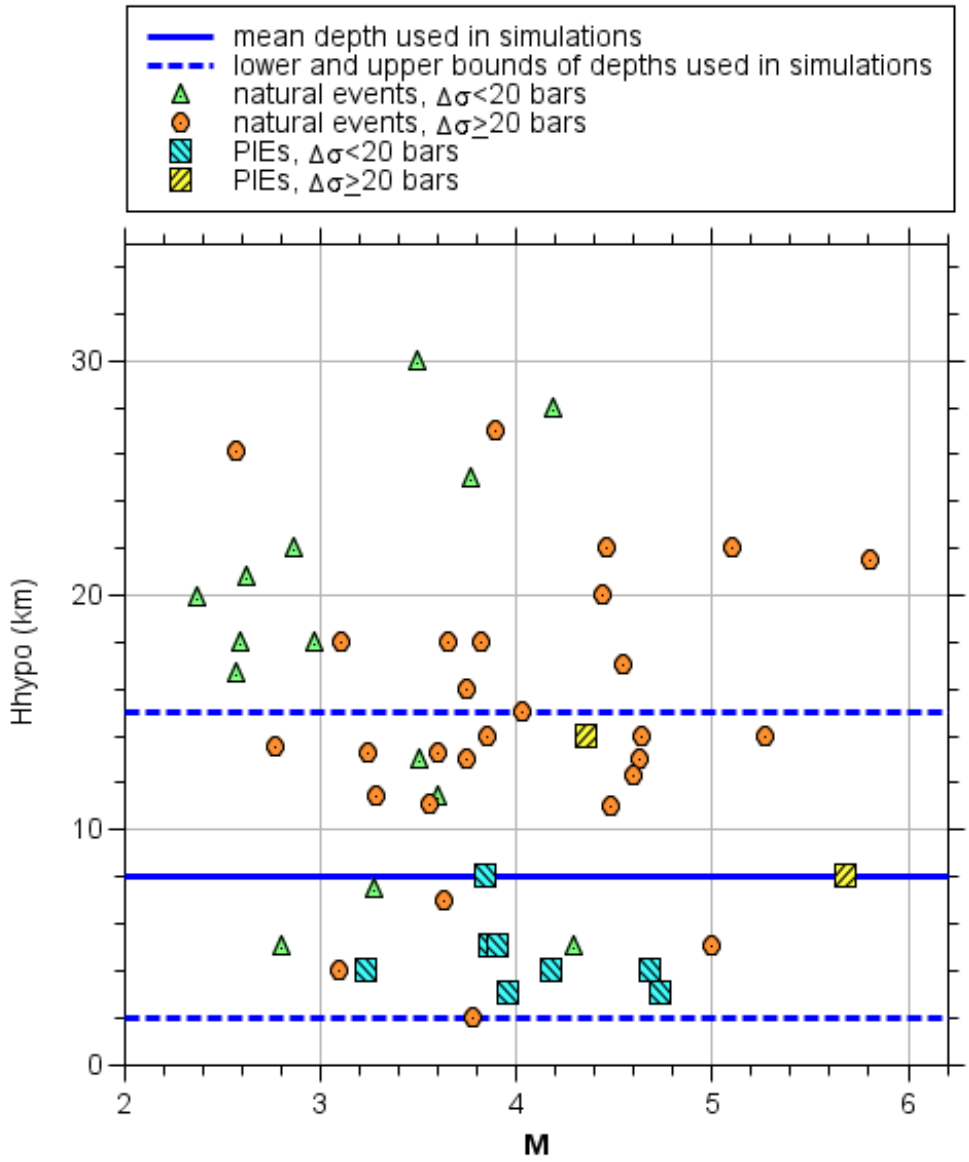

Figure 3.8 Magnitude-depth distribution of events for which Darragh et al. determined stress parameters. The horizontal blue lines show the depth range used in the simulations (it is our understanding that these depths were used to give a range of R_{RUP} for a given R_{JB}; no depth dependence of $\Delta\sigma$ was used in the simulations).

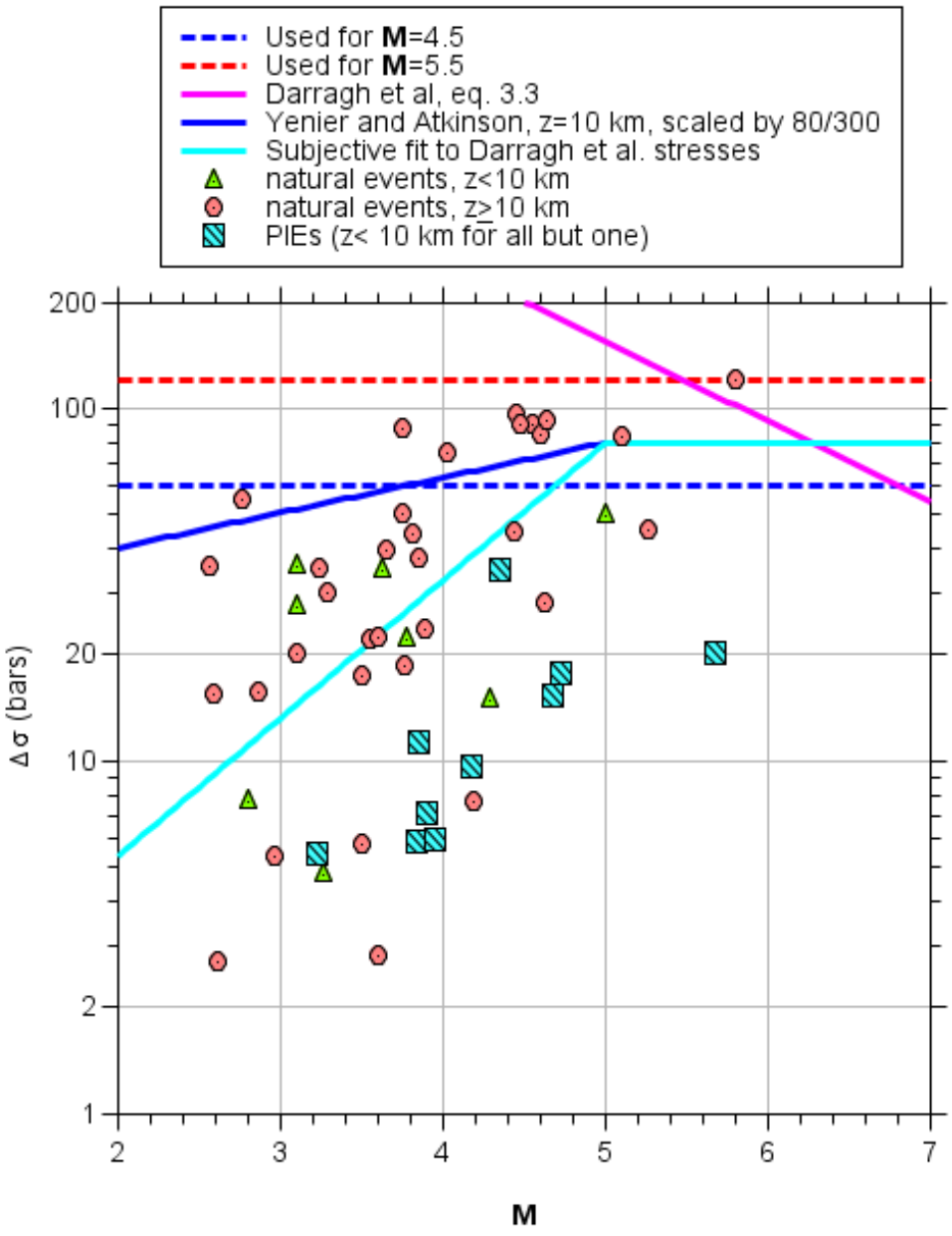

Figure 3.9 DASGs stress parameters as a function of magnitude. The lines are from YA15 for **M**4 and a subjective fit by D. Boore to DASG's values. Also shown by lines are the stressed used by DASG for **M**4.5 and **M**5.5, as well as for their magnitude-dependent stress model for larger magnitudes (the magenta line).

In addition to generally having the smallest values of $\Delta\sigma$, the **M** dependence of $\Delta\sigma$ is clearest for PIEs. The **M** dependence is not as clear for shallower natural events, but there are only two shallow (z < 10 km) natural events with **M** > 4, so it would difficult to conclude anything about a **M** dependence for shallow natural events. The case for an **M** dependence of $\Delta\sigma$ is somewhat stronger for the natural events with z > 10, but again the lack of many large events makes it difficult to draw firm conclusions. DASG realized this, so they used an **M** dependence of $\Delta\sigma$ from Western North America (WNA) data, centering it on their derived value of $\Delta\sigma$ for CENA natural events with a magnitude near 4.5. Figure 3.9 shows their **M**-dependent $\Delta\sigma$ for larger events.

Also shown in Figure 3.9 is the **M**-dependence found by YA15. Because of the large difference in the amplitudes of $\Delta\sigma$ from the two studies, the YA15 curve was adjusted downward by a factor of 80/300 in order for it to coincide at **M** = 5 (with the subjective relation between $\Delta\sigma$ and **M** for the DASG results). It appears that DASG's **M**-dependent $\Delta\sigma$ is stronger than found by YA15. The dependence of $\Delta\sigma$ on focal depth for the DASG study is shown in Figure 3.10.

There seems to be no depth dependence of $\Delta\sigma$ for small magnitude (**M** < 4) natural events, and there are too few larger natural events with focal depths less than 10 km to conclude anything about the depth dependence of $\Delta\sigma$ for larger, shallow events. On the other hand, excluding the smaller natural events, the depth dependence of the DASG's $\Delta\sigma$, including the PIEs, is roughly consistent with the depth dependence from the YA15 study (adjusted for the difference in absolute values of $\Delta\sigma$ between the two studies).

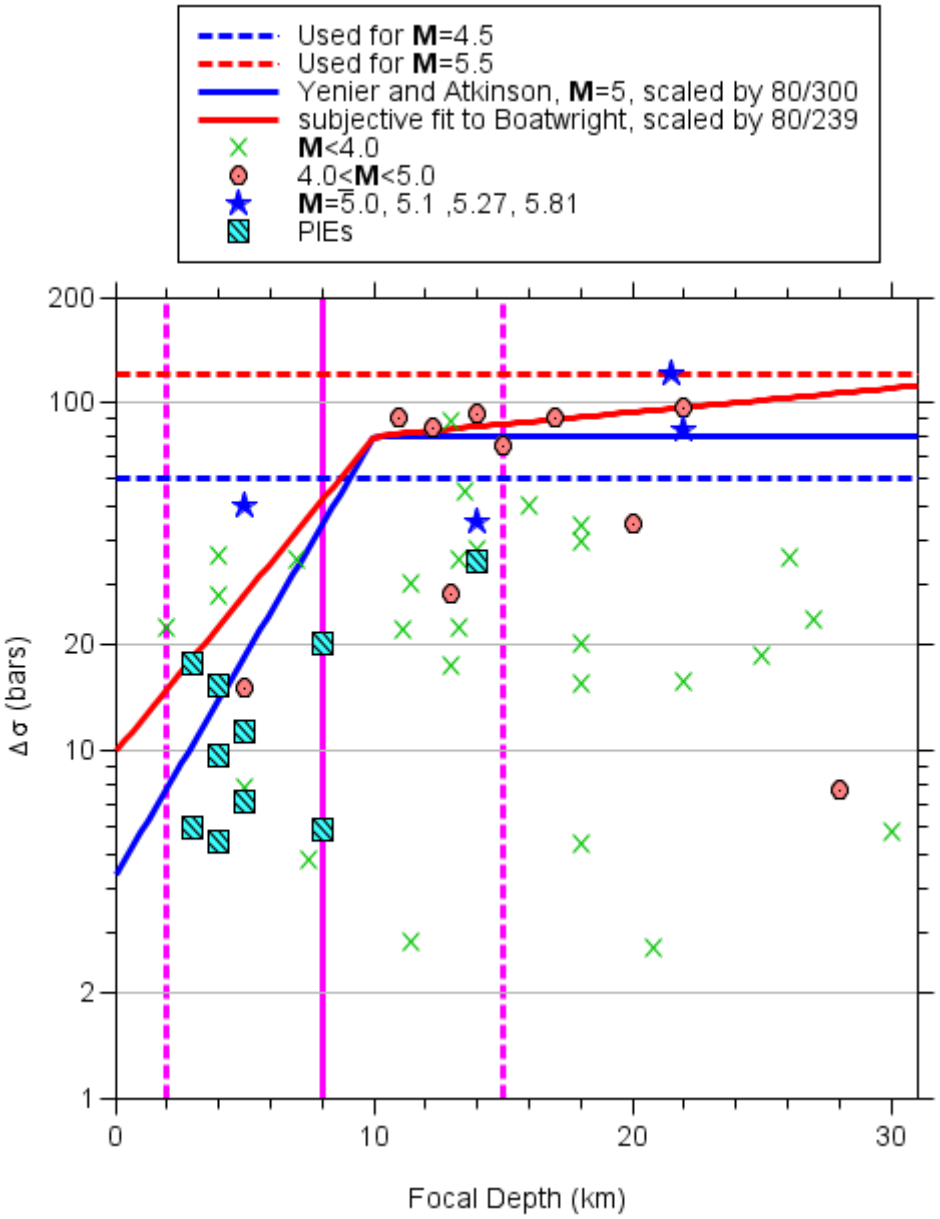

Figure 3.10 DASG's stress parameters as a function of focal depth. The solid lines are from Yenier and Atkinson for **M**4 and a subjective fit by D. Boore to Boatwright's values for eastern Quebec. Those lines were adjusted downward by the indicated factors to account for the differences in the values of $\Delta\sigma$ (see text for details). The horizontal dashed lines are values in DASG's depth-dependent $\Delta\sigma$ model for two magnitudes; the vertical magenta lines show the range of depths used in DASG's simulations (but they did not allow any depth dependence of $\Delta\sigma$ in their simulations—see caption to Figure 3.8).

3.2.2 Consequences of a Depth-Dependent Stress Parameter using the Point-Source Stochastic Model

The three studies of $\Delta\sigma$ reviewed in the previous section do not all reach the same conclusions about the magnitude and depth dependence of $\Delta\sigma$. We do find, however, that the evidence for an increasing $\Delta\sigma$ with depth for depths less than 10 km is fairly convincing. It seems that this increase is consistent both for natural events and PIEs. It does not seem to be a magnitude effect, as the depth distribution for a given range of magnitudes extends from shallow depths to over 20 km. The next steps for the analysis are to determine a depth dependence of $\Delta\sigma$ and then to use this dependence to do simulations of ground motions for varying depth but fixed values of R_{RUP}. Using simulations allows us to propagate those effects to a wider range of **M**, depth and distances, and to draw conclusions on the importance to ground motions of a depth dependence of $\Delta\sigma$.

The Stress Parameter–Depth Function, $\Delta\sigma(z)$

The selected stress parameter–depth function $\Delta\sigma(z)$ combines the YA15 function for depths less than 10 km and the subjective fit to Boatwright's data for deeper depths (these functions are shown in Figures 3.7 and 3.10). Because the simulations will use the Boatwright and Seekins [2011] (BS11) attenuation model and the other model parameters developed for the Boore GMMs (see Chapter 2 of the PEER NGA-East GMM report [2015]), the functions were adjusted to give the median value of 172 bars consistent with the GMM development [this value was obtained from inverting nine well-recorded earthquakes in Eastern North America (ENA)]. In the original work, this value of $\Delta\sigma$ was assigned to a depth of 13 km, which is the median value of the focal depths of the earthquakes used in the inversion. The selected $\Delta\sigma(z)$ function is shown in Figure 3.11; also shown in the figure are averages of the stress parameter over various ranges of depth, as discussed in the next section.

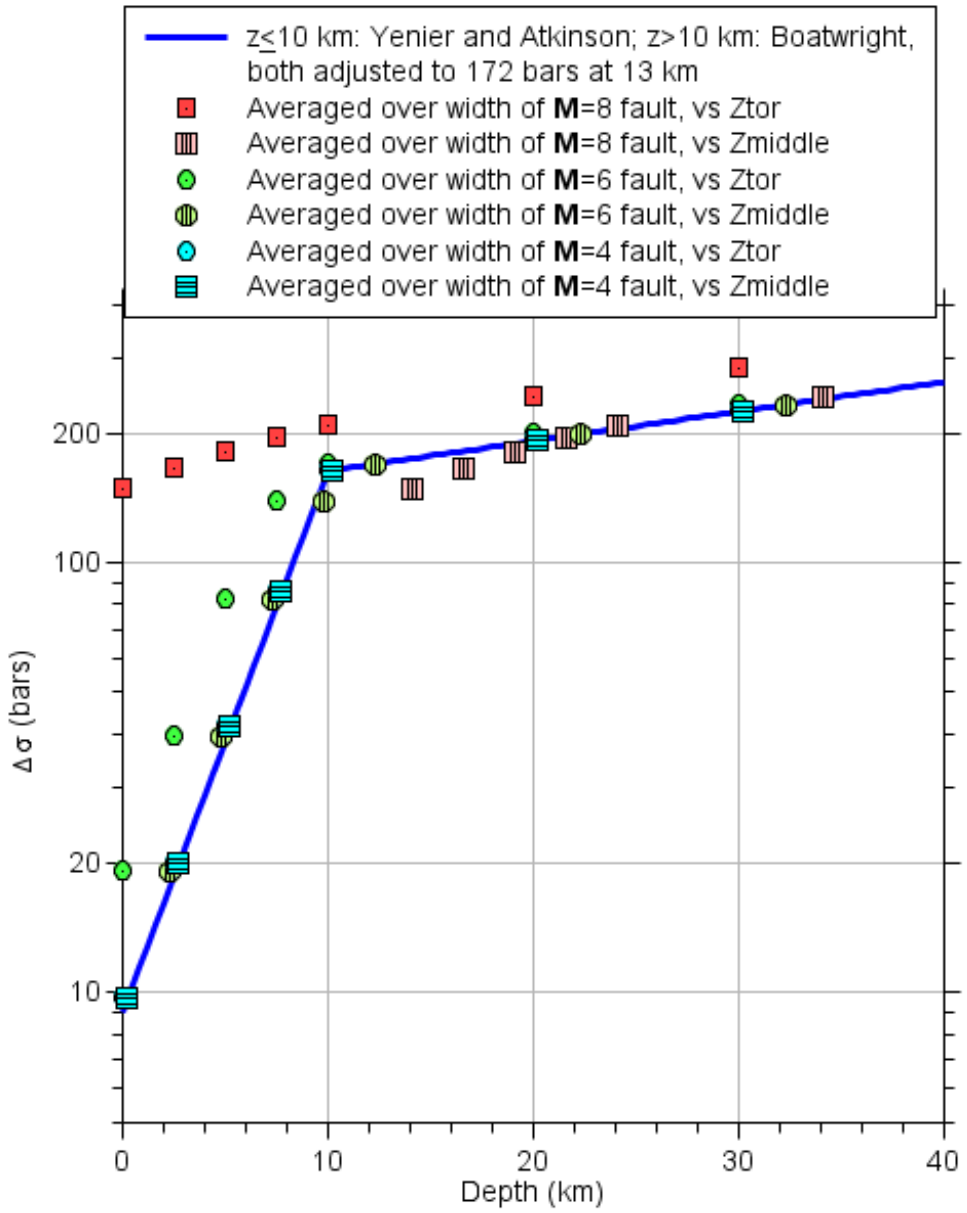

Figure 3.11 The stress parameter–depth function used in the simulations. Shown is the $\Delta\sigma(z)$ function from the inversions discussed earlier, as well as the stress parameters used in the simulations for three magnitudes (**M** = 4, 6, and 8); these parameters were derived by an averaging of a power of $\Delta\sigma(z)$ over the width of the fault for each magnitude.

Simulated Motions using SMSIM

The SMSIM stochastic-method program *tmrs_loop_rv_drvr* [Boore 2005] was used to simulate motions for $\Delta\sigma$ at a number of depths. In addition to $\Delta\sigma$, the other depth-dependent parameters were the source velocity and density, and the crustal amplifications. The velocity profile shown in Figure 5 of Boore and Thompson [2015] (BT15), for which V_{S30} is 3 km/sec, was used. The BT15 amplifications were modified by multiplying the values by the square root of the seismic impedance at each depth by that for the reference depth of 8 km used by BT15. This resulted in only small increases (less than 5%) of the crustal amplifications for depths less 8 km. We assumed no changes in the amplifications for sources at deeper depths (the BT15 model is constant below about 9 km).

The BT15 finite-fault adjustment factors for stable continental regions were used to convert R_{RUP} to the point-source distance R_{PS} (note that h on the left side of BT15's equation (3) for the finite-fault adjustment factor should be log$h$).

The motions were simulated for **M.**=.4, 5, 6, 7, and 8, R_{RUP} = 20 km and 200 km, and depths from 0 km to 30 km. Note that although a point-source simulation method was used, finiteness of the fault was accounted for in several ways. The most important aspect is that the stress parameter used for the simulations of motions for each magnitude was taken as an average of the $\Delta\sigma(z)$ over a fault width, assuming a dip of 45°. The fault widths were those used in the Graves and Pitarka [2015] simulations developed for the NGA-East median GMMs (Appendix 1B in the previous PEER report [2015]). They are given in Table 3.1.

Table 3.1 Fault widths (W) used in finding an average stress parameter (courtesy of R. Graves).

M	W (km)
4	0.8
5	2.5
6	6.5
7	16
8	40

Assuming that high-frequency motions from various points on the rupture surface add incoherency, and in view of the high-frequency portion of the FAS (above the corner frequency) where $\text{FAS} \approx \Delta\sigma^{2/3}$, the effective stress parameter was given by

$$\overline{\Delta\sigma(Z_{TOR},\mathbf{M})} = \left[\sqrt{\frac{1}{N}\sum_{i=1}^{n}\left(\Delta\sigma(z_i)^{2/3}\right)^2}\right]^{3/2} \tag{3.1}$$

where the sum is over depths spanned by the width of the fault, starting at the depth Z_{TOR}. The width depends on magnitude **M** (Table 3.1). The source velocity and density were taken from the Boore and Thompson [2015] (BT15) V_{S30} = 3 km/sec velocity model at a depth corresponding to

the midpoint of the fault width for each Z_{TOR}. This velocity and density were also used to adjust the BT15 crustal amplifications. In general the effect of using these **M**- and Z_{TOR}-dependent velocities and densities was small compared to the effect of averaging $\Delta\sigma$ over the fault width. One other modification to capture finite-fault effects was to use the BT15 finite-fault adjustment factor. As ratios of motions for a fixed R_{RUP} were of primary interest, the effect of the finite-fault adjustment to distance was minor.

Before showing the results, we note from Figure 3.11 that there is an over-a-factor-of-10 increase in $\Delta\sigma$ from 0 to 10 km for small earthquakes. This will obviously result in a large increase in the simulated ground motions. For example, equation A10a in Boore [1983] shows that

$$\log PGA \approx 0.8 \log \Delta\sigma \tag{3.2}$$

therefore, an increase of a factor of 10 in $\Delta\sigma$ will result in an increase factor of more than 6 in ground motions.

The ratios of motions (PSA) at different Z_{TOR} depths z to those at Z_{TOR} = 10 km are shown in Figures 3.12–3.16 (one magnitude per figure). Because of the changing corner frequency with magnitude and stress parameter, the ratios are period dependent. As magnitude increases, the period range of essentially constant ratios increases. There is little difference in the ratios for R_{RUP} = 20 km and 200 km, as expected (as all parameters related to the path are being held constant, and the figures only show ratios of motions).

Although the figures above contain a complete summary of the results, what is often wanted is an idea of what change of motions with depth occurs for a fixed period and magnitude. To satisfy this desire, Figure 3.17 shows that dependence for T = 0.2 sec and magnitudes of **M** = 4, 5, 6, 7, and 8.

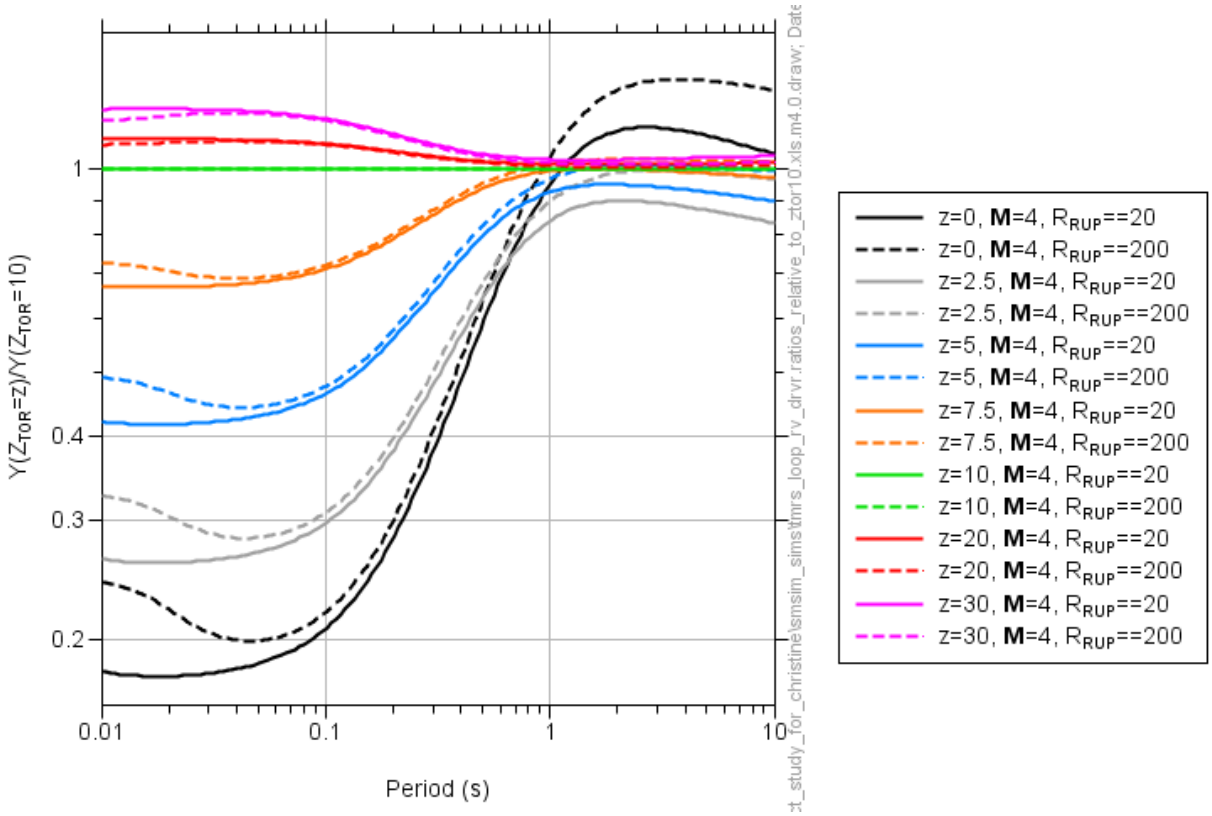

Figure 3. 12 Ratio of simulated motions from point sources at depths z (in km) and 10 km, for **M** = 4 and two values of R_{RUP}: (20 km and 200 km). The relation between $\Delta\sigma$ and z discussed above was used in choosing the $\Delta\sigma$ to be used for the point source at each depth z.

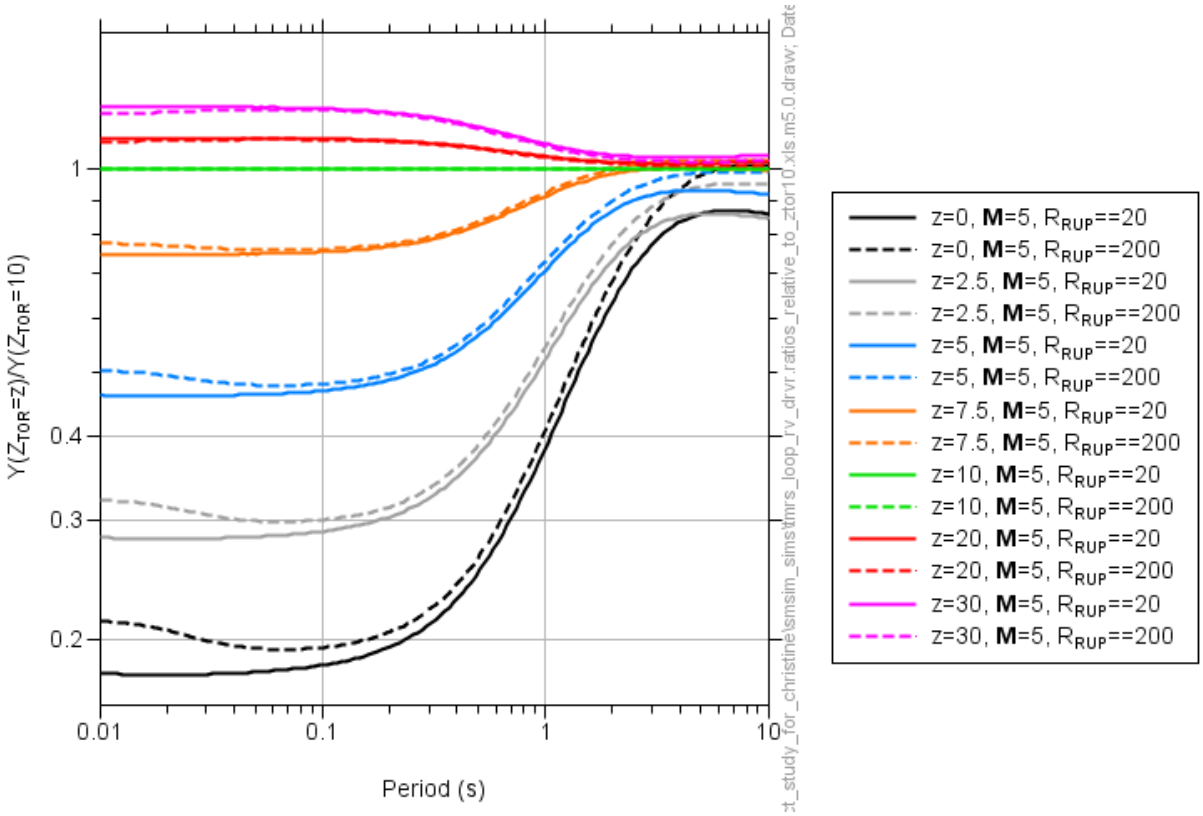

Figure 3.13 Ratio of simulated motions from point sources at depths z (in km) and 10 km for **M** = 5 and two values of R_{RUP} (20 km and 200 km). The relation between $\Delta\sigma$ and z discussed above was used in choosing the $\Delta\sigma$ to be used for the point source at each depth z.

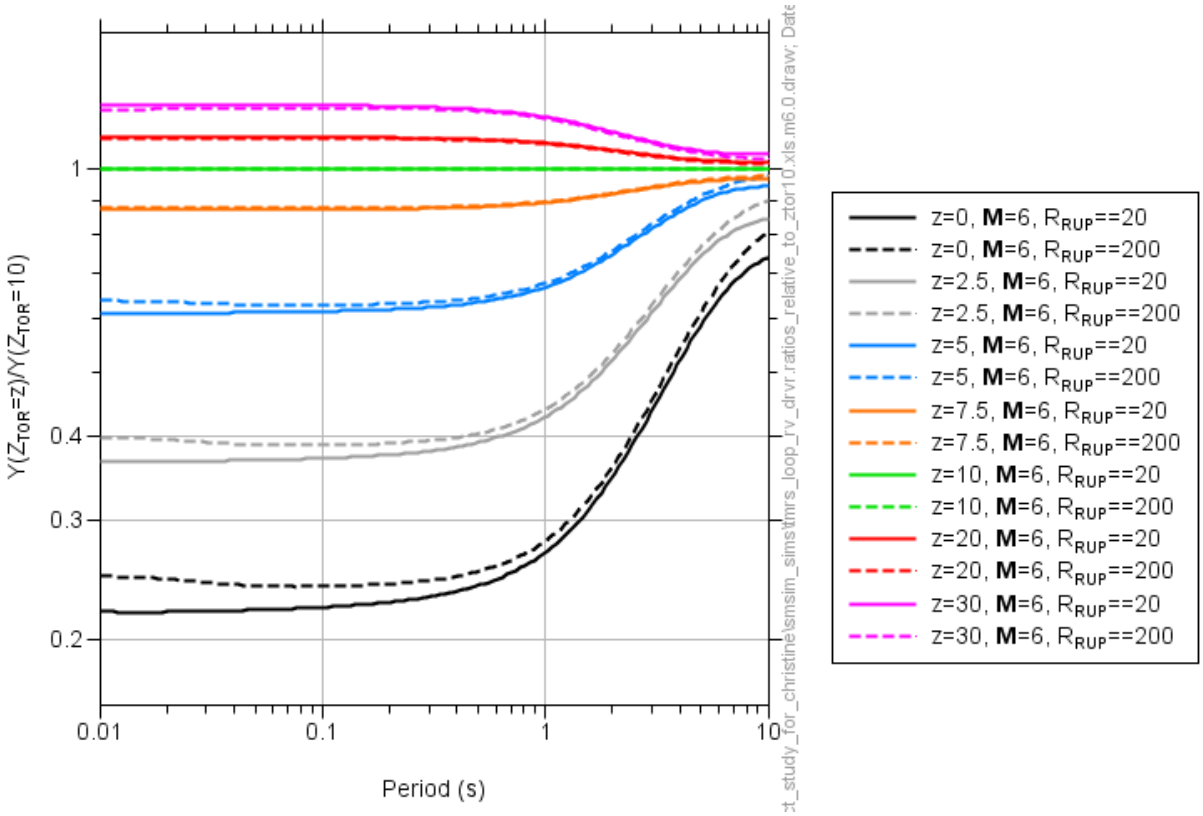

Figure 3.14 Ratio of simulated motions from point sources at depths z (in km) and 10 km for **M** = 6 and two values of R_{RUP} (20 km and 200 km). The relation between $\Delta\sigma$ and z discussed above was used in choosing the $\Delta\sigma$ to be used for the point source at each depth z.

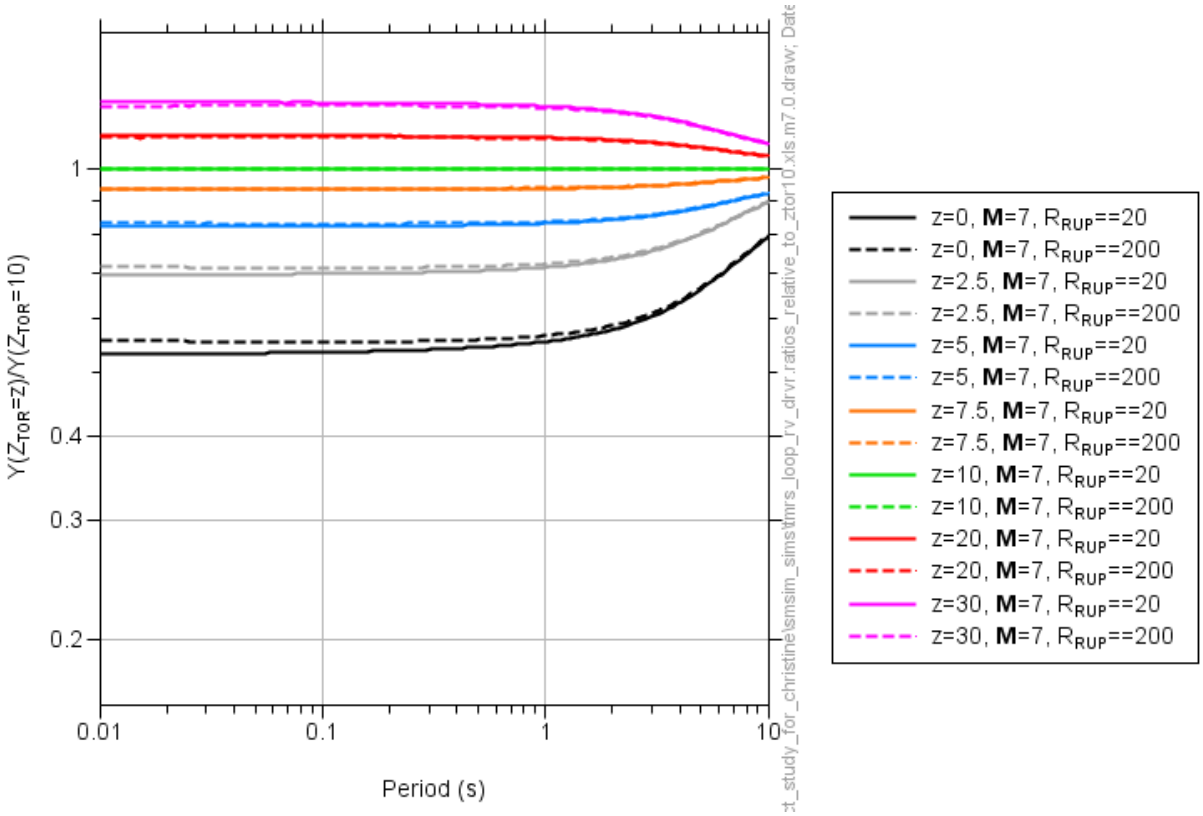

Figure 3.15 Ratio of simulated motions from point sources at depths z (in km) and 10 km for **M** = 7 and two values of R_{RUP} (20 km and 200 km). The relation between $\Delta\sigma$ and z discussed above was used in choosing the $\Delta\sigma$ to be used for the point source at each depth z.

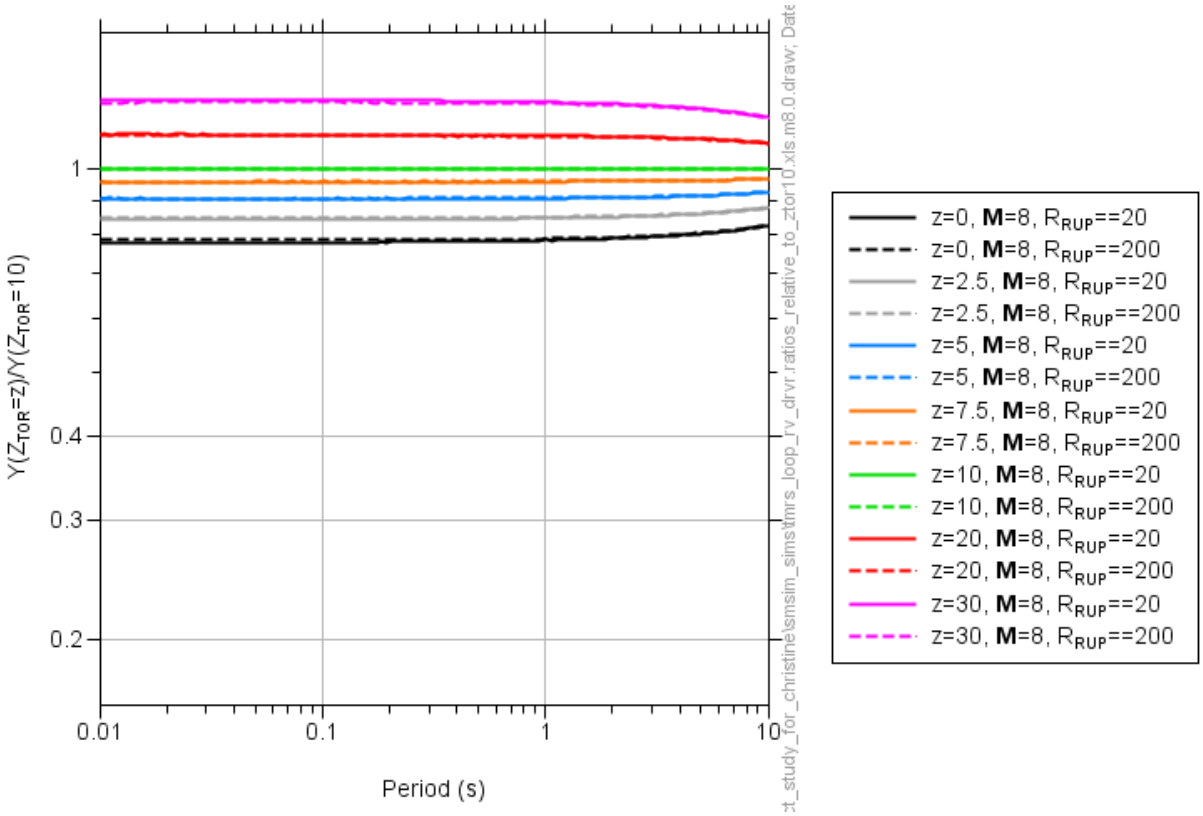

Figure 3.16 Ratio of simulated motions from point sources at depths *z* (in km) and 10 km for **M**=8 and two values of R_{RUP} (20 km and 200 km). The relation between $\Delta\sigma$ and z discussed above was used in choosing the $\Delta\sigma$ to be used for the point source at each depth *z*.

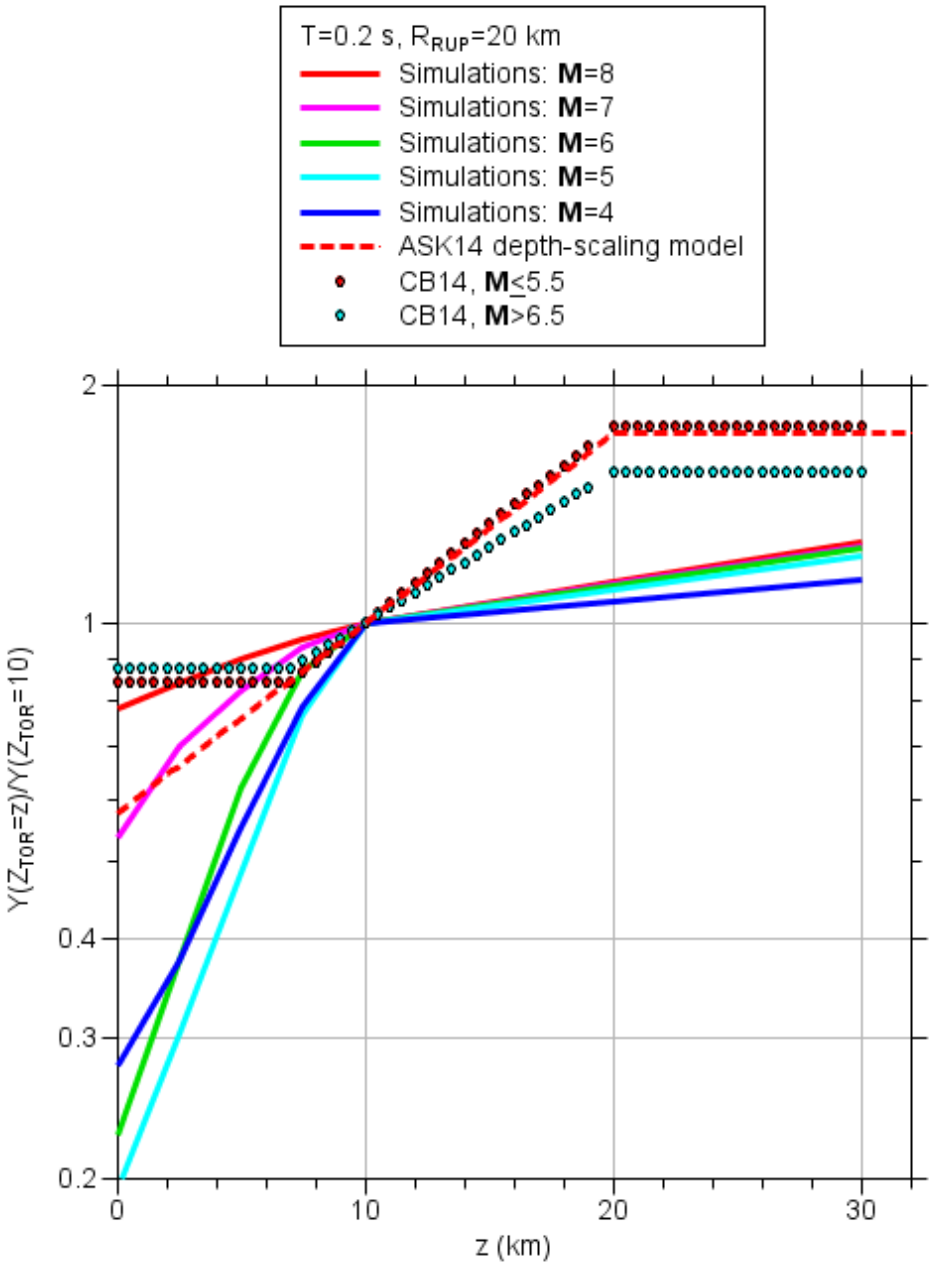

Figure 3.17 Ratio of simulated $T = 0.2$ sec response spectra from point sources at the indicated depth $Z_{TOR} = z$ and $Z_{TOR} = 10$ km for **M**=4, 5, 6, 7, and 8, and $R_{RUP} = 20$ km. The stress parameter used in the simulations was from an average of $\Delta\sigma(z)$ over the fault width for each magnitude event.

Figure 3.17 also compares the results with those from two NGA-West2 models (Abrahamson et al. [ASK14] and Campbell and Bozorgnia [CB14]). The models show a much weaker depth dependence to the motions for depths less than 10 km for small events, and most show a stronger dependence at greater depths. For larger events and depths less than about 10 km, the simulated depth dependence is somewhat similar to scaling shown by the NGA-West2 models (especially ASK14).

Discussion

There appears to be a depth dependence to the stress parameter for small events at depths less than about 10 km. This includes almost all PIEs and some natural earthquakes, as seen in Figures 3.2, 3.5, and 3.8, and in Figure 3.18, made from the complete 18 November 2014 NGA-East flatfile [Goulet et al. 2014].

If the depth dependence $\Delta\sigma$ found in the inversion studies reviewed above, there is a significant depth dependence to ground motions for depths less than 10 km that is not captured in the NGA-East ground-motion models. On the other hand, this depth dependence might only be of practical importance for shallow, small-magnitude events. As the figure above shows, most natural events occur at depths greater than 10 km, even those with small magnitudes. For this reason, although the effect of the depth variation on ground motions is substantial, it is primarily of importance mostly for PIEs.

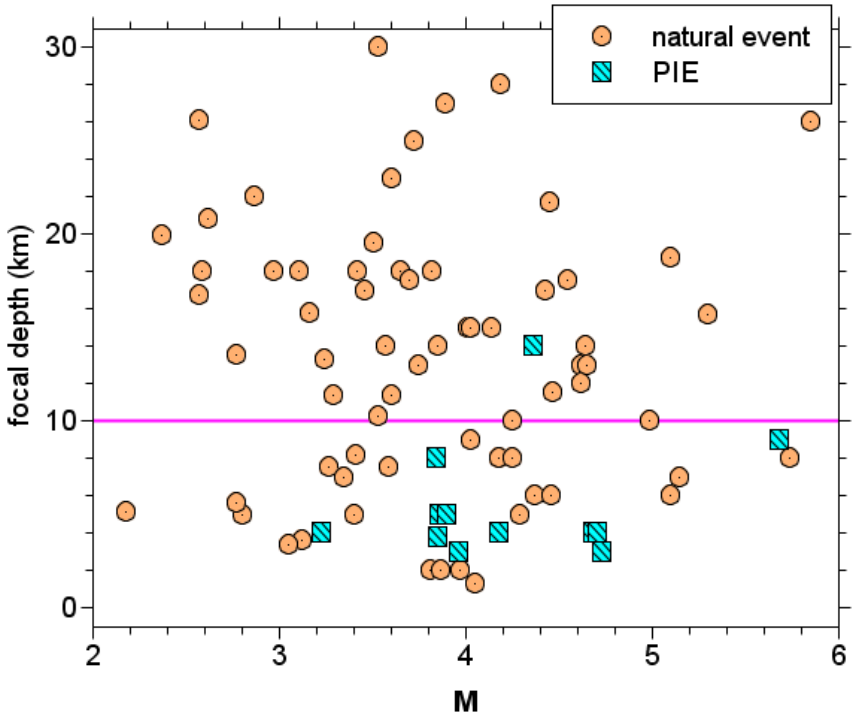

Figure 3.18 Focal depth—magnitude scatterplot for events in the 18 November 2014 NGA-East database flatfile [Goulet et al. 2014].

3.3 EXISTING SOURCE-DEPTH MODELS

The distribution of depth for **M** > 5.5 in the NGA-East database is not well populated. Therefore the scaling of ground motion with source depth for **M** > 5.5 cannot be derived empirically from the NGA-East data. Rather, existing models developed for data-rich regions are used as the basis for the development of a model appropriate for CENA. This section presents existing models for source-depth scaling, which will be used to guide the development of a source-depth adjustment model for CENA. There are four source-depth scaling models presented here: three from NGA-West2 [Bozorgnia et al., 2014]: Chiou and Youngs [2014] (CY14), Campbell and Bozorgnia [2014] (CB14), and Abrahamson, Silva and, Kamai [2014] (ASK14), and one from the PEER NGA-East Median GMM [2015]. The four source-depth scaling models are not all a function of the same source-depth metric (CY14 Z_{TOR}, ASK14 Z_{TOR}, CB14 Z_{HYP} and, PEER NGA-East Z_{HYP}). This can present challenges when comparing them to one another. However, if the magnitude ranges these are applicable to is taken into consideration, informed decisions can be made. Additionally, we present a model for the expected value of Z_{TOR} as a function of **M**, which will be considered when centering the proposed source-depth adjustment model.

Chiou and Youngs 2014

The CY14 model, which predicts peak ground-motion values and PSA values for a range of frequencies, includes a source-depth scaling model that is magnitude dependent. The basic form of this GMM, including depth scaling is:

$$\ln\left(y_{ref,ij}\right) = f_{RV} + f_{NM} + f_{Z_{TOR}} + f_{\delta} + f_{\mathbf{M}} + f_{geom} + f_{\gamma} + f_{D} + f_{HW} \tag{3.3}$$

where $y_{ref.ij}$ is the predicted ground-motion intensity measure for the i^{th} event at the j^{th} station for the reference site condition, f_{RV} is the reverse mechanism scaling model, f_{NM} is the normal mechanism scaling model, f_{ZTOR} is the source-depth scaling model, f_{δ} is the fault-dip scaling model, $f_{\mathbf{M}}$ is the magnitude scaling model, f_{geom} is the geometrical spreading model, f_{γ} is the anelastic attenuation model, f_D is the directivity model, and f_{HW} is the hanging-wall model. The source-depth scaling model is given by:

$$f_{Z_{TOR}} = f_{Z_{TOR},\mathbf{M}} \Delta Z_{TORi} \tag{3.4}$$

where $f_{Z_{TOR},\mathbf{M}}$ is the magnitude-dependent scaling factor, and ΔZ_{TORi} is the centered Z_{TOR}. The magnitude-dependent scaling factor, $f_{Z_{TOR},\mathbf{M}}$, is given by,

$$f_{Z_{TOR},\mathbf{M}} = \left\{ c_7 + \frac{c_{7b}}{\cosh\left[2 \cdot \max\left(\mathbf{M}_i - 4.5, 0\right)\right]} \right\} \tag{3.5}$$

where c_7 and c_{7b} are frequency-dependent coefficients. ΔZ_{TORi} is given by,

$$\Delta Z_{TORi} = Z_{TORi} - E(Z_{TOR}) \tag{3.6}$$

where $E(Z_{TORi})$ is the mean Z_{TOR} as a function of both magnitude and earthquake focal mechanism. For reverse and reverse-oblique mechanisms, $E(Z_{TORi})$ is given by,

$$E\left[Z_{TOR}\right] = \max\left[2.704 - 1.226\max\left(\mathbf{M} - 5.849, 0\right), 0\right]^2 \tag{3.7}$$

and for strike–slip and normal mechanisms $E(Z_{TORi})$ is given by,

$$E(Z_{TOR}) = \max\left[2.673 - 1.136\max\left(\mathbf{M} - 4.790, 0\right), 0\right]^2 \tag{3.8}$$

Abrahamson, Silva, and Kamai 2014

The ASK14 model, which predicts peak ground-motion values and PSA values for a range of frequencies, includes a source-depth scaling model that is magnitude independent. The basic form of this GMM, including depth scaling, is:

$$\ln\left(y_{ij}\right) = f_B + f_{RV} + f_{NM} + f_{AS} + f_{VS} + f_{HW} + f_{Z_{TOR}} + f_{Z_1} + f_{Reg} \tag{3.9}$$

where y_{ij} is the predicted ground-motion intensity measure for the i^{th} event at the j^{th} station, f_B is the base model, which includes magnitude and distance scaling, f_{AS} is the aftershock scaling model, f_{VS} is the nonlinear site response model, f_{z1} is the soil-depth model, and f_{Reg} is the regional adjustment model to the site response model and the anelastic attenuation for Taiwan, China, and, Japan. The source-depth scaling model is given by:

$$f_{Z_{TOR}} = \begin{cases} a_{15}\frac{Z_{TOR}}{20} & \text{for } Z_{TOR} < 20 \text{ km} \\ a_{15} & \text{for } Z_{TOR} \geq 20 \text{ km} \end{cases} \tag{3.10}$$

where a_{15} is a frequency-dependent coefficient.

Campbell and Bozorgnia 2014

The CB14 model, which predicts peak ground-motion values and PSA values at a range of frequencies, includes a source-depth scaling model that is magnitude dependent. The basic form of this GMM, including depth scaling, is:

$$\ln\left(y_{ij}\right) = f_{\mathbf{M}} + f_{geom} + f_{flt} + f_{HW} + f_{VS} + f_{sed} + f_{Z_{HYP}} + f_{\delta} + f_{\gamma} \tag{3.11}$$

where, f_{flt} is the style of faulting model, f_{sed} is the basin response model, and, $f_{Z_{HYP}}$ is the source-depth scaling model. The source-depth scaling model is given by:

$$f_{Z_{HYP}} = f_{Z_{HYP},H} f_{Z_{HYP},\mathbf{M}} \tag{3.12}$$

where $f_{Z_{HYP},H}$ is the centered hypocentral depth (Z_{HYP}) given by,

$$f_{Z_{HYP},H} = \begin{cases} 0 & Z_{HYP} \leq 7 \\ Z_{HYP} - 7 & 7 < Z_{HYP} \leq 20 \\ 13 & Z_{HYP} > 20 \end{cases} \tag{3.13}$$

and $f_{Z_{HYP},\mathbf{M}}$ is the magnitude-dependent scaling factor given by,

$$f_{Z_{HYP},M} = \begin{cases} c_{17} & \mathbf{M} \le 5.5 \\ \left[c_{17} + (c_{18} - c_{17})(\mathbf{M} - 5.5)\right] & 5.5 < \mathbf{M} \le 6.5 \\ c_{18} & \mathbf{M} > 6.5 \end{cases} \quad (3.14)$$

where c_{17} and c_{18} are frequency-dependent coefficients.

PEER NGA-East Median GMM

The PEER NGA-East Median GMM, described in detail in the previous PEER report [2015], included Z_{HYP} as a predictive parameter in the empirical portion of the model. The empirical portion of this model was developed on the FAS of acceleration; thus the source-depth scaling model was not developed specifically for PSA or other peak ground motions. The source depth-scaling portion of the FAS GMM is given by

$$f_{Z_{TOR},FAS} = c_9 \frac{Z_{HYP}}{20} \quad (3.15)$$

where c_9 is a frequency-dependent coefficient. This coefficient is not directly comparable to the source-depth scaling factors of the NGA-West2 models. To make a more direct comparison, the PEER team predicted PSA for a range of oscillator frequencies from 0.1–100 Hz, Z_{HYP} = 5, 10, 20, and 30 km, **M** = 5, R_{RUP} = 20 km, and V_{S30} = 760 m/sec. These were then fit to a simple model, given by

$$f_{Z_{TOR}} = b_9' \frac{Z_{HYP}}{20} \quad (3.16)$$

where b_9' is a frequency-dependent coefficient. This coefficient is more comparable to the NGA-West2 source-depth scaling factors.

Comparisons of Source-Depth Scaling Models

These four models are not all directly comparable (two have magnitude-dependent scaling, two are based on Z_{TOR}), but in order to illustrate how the NGA-East depth-scaling adjustment model will behave, it is important to know how similar/different they are from one another. Figure 3.19 shows a comparison of their depth-scaling factors ($f_{Z_{TOR},\mathbf{M}}$ for CY14, $a_{15}/20$ for ASK14, $f_{Z_{HYP},\mathbf{M}}$ for CB14 and, $b_9'/20$ for PEER NGA-East) for various magnitudes as a function of frequency. These scale factors represent how much the natural log of the median prediction of ground motion would change given a unit change in source-depth parameter (either Z_{TOR} or Z_{HYP}).

For **M** ≥ 6.5, the source-depth scaling factors are comparable; the magnitude-dependent models stop changing (CB14) or change very little (CY14) above this magnitude. However at **M**5, the range of scale factors between models is a factor of two or greater for frequencies above 10 Hz. The PEER source-depth scale factor compares reasonably with the three NGA-West2 scale factors. Similar to the ASK14 model, the PEER source-depth scale factor is not magnitude-dependent. This is driven by the fact that the distribution of depth for **M** > 5.5 in the NGA-East database is not well populated.

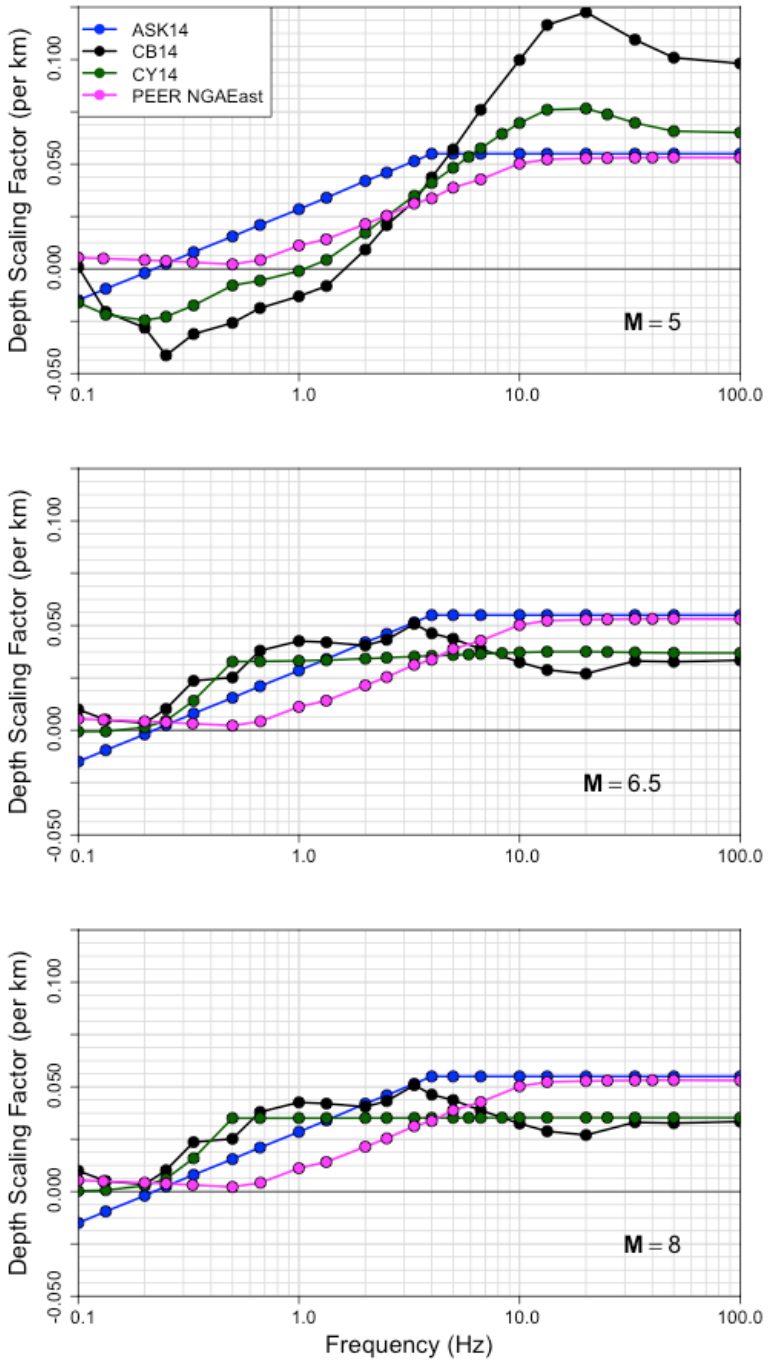

Figure 3.19 Source-depth model scale factors for the three NGA-West2 models and the implied source-depth scaling factor from the PEER NGA-East model: CY14 in dark green, ASK14 in blue and, CB14 in black, PEER in magenta (top **M** = 5.0, middle **M** = 6.5, and bottom **M** = 8.0).

3.4 DEVELOPMENT OF SOURCE-DEPTH ADJUSTMENT MODEL

This section presents a simplified model for adding source-depth scaling to the NGA-East median GMMs, including a source-depth scaling and its proposed model centering. The formulation of this model is based on the models presented in the previous section. The model developed here is parameterized with Z_{TOR}. The main motivation for choosing Z_{TOR} is that it is a less computationally intensive parameter to integrate into PSHA computations.

3.4.1 Source-Depth Scaling

The shape of the three NGA-West2 source-depth scaling models with frequency and magnitude guides the proposed source-depth adjustment model. Additionally, the proposed model is constrained by the source-depth scaling implied by PEER NGA-East Median GMM [2015].

The proposed source-depth adjustment model for the suite of NGA-East median GMMs is given by

$$f_{Z_{TOR}} = f_{Z_{TOR},\mathbf{M}}\, f_{Z_{TOR},Z} \tag{3.17}$$

where $f_{Z_{TOR},\mathbf{M}}$ is the magnitude-dependent source-depth scaling factor, and $f_{Z_{TOR},Z}$ is the centered Z_{TOR}. The magnitude-dependent source-depth scaling factor, $f_{Z_{TOR},M}$, is given by

$$f_{Z_{TOR},\mathbf{M}} = \begin{cases} b_1 & \mathbf{M} \le 5.0 \\ b_1 + \dfrac{b_2(\mathbf{M}-5.0)}{1.5} & 5 < \mathbf{M} \le 6.5 \\ b_1 + b_2 & 6.5 < \mathbf{M} \end{cases} \tag{3.18}$$

where b_1 and b_2 are frequency-dependent coefficients, see Table 3.2. The coefficients b_1 and b_2 were set by averaging the three NGA-West2 models over the range of low to intermediate frequencies and by following the PEER model at high frequencies. The threshold of high and low frequency was magnitude-dependent, reflecting the magnitude-dependence trends from two of the NGA-West2 models. The functional form was selected to offer a simple, smooth transition between the source-depth scaling factor for **M**5 and **M** 6.5. Figure 3.20 shows the average of the NGA-West2 models for the full frequency range and for **M**5 and **M**6.5, as well as the proposed model. Figure 3.21 shows the proposed source-depth scale factors plotted against frequency for a range of **M**.

For all magnitudes, the average of the NGA-West2 source-depth scaling factors was taken for the proposed model between 0.33 and 5 Hz. For simplicity, the source-depth scale factors are flat at frequencies above 5 Hz and below 0.33 Hz to avoid adopting a more complicated shape that is not informed by NGA-East data. Above 5.0 Hz the proposed model was held constant at the 5-Hz value. This constraint was imposed because 5.0 Hz is where the average of the NGA-West2 models reaches the level of scale factor implied by the PEER model at high frequencies. Below 0.33 Hz the proposed model was set at the NGA-West2 average for all the frequencies below 0.33 Hz, allowing the model to go to negative values. The same rule was applied to all magnitudes. Table 3.1 provides the model coefficients for Equation (3.18).

Table 3.2 Coefficients for proposed model [Equation (3.18)].

Frequency/GMIM	b_1	b_2
0.10	-0.01653	0.0173
0.13	-0.01653	0.0173
0.20	-0.01653	0.0173
0.25	-0.01653	0.0173
0.33	-0.01351	0.02875
0.50	-0.00607	0.03055
0.67	-0.00111	0.03174
1.00	0.00479	0.02996
1.33	0.01003	0.02646
2.00	0.02279	0.0161
2.50	0.03069	0.00821
3.33	0.03958	-0.00069
4.00	0.04658	-0.00768
5.00	0.05346	-0.01457
5.88	0.05346	-0.01457
6.67	0.05346	-0.01457
8.33	0.05346	-0.01457
10.00	0.05346	-0.01457

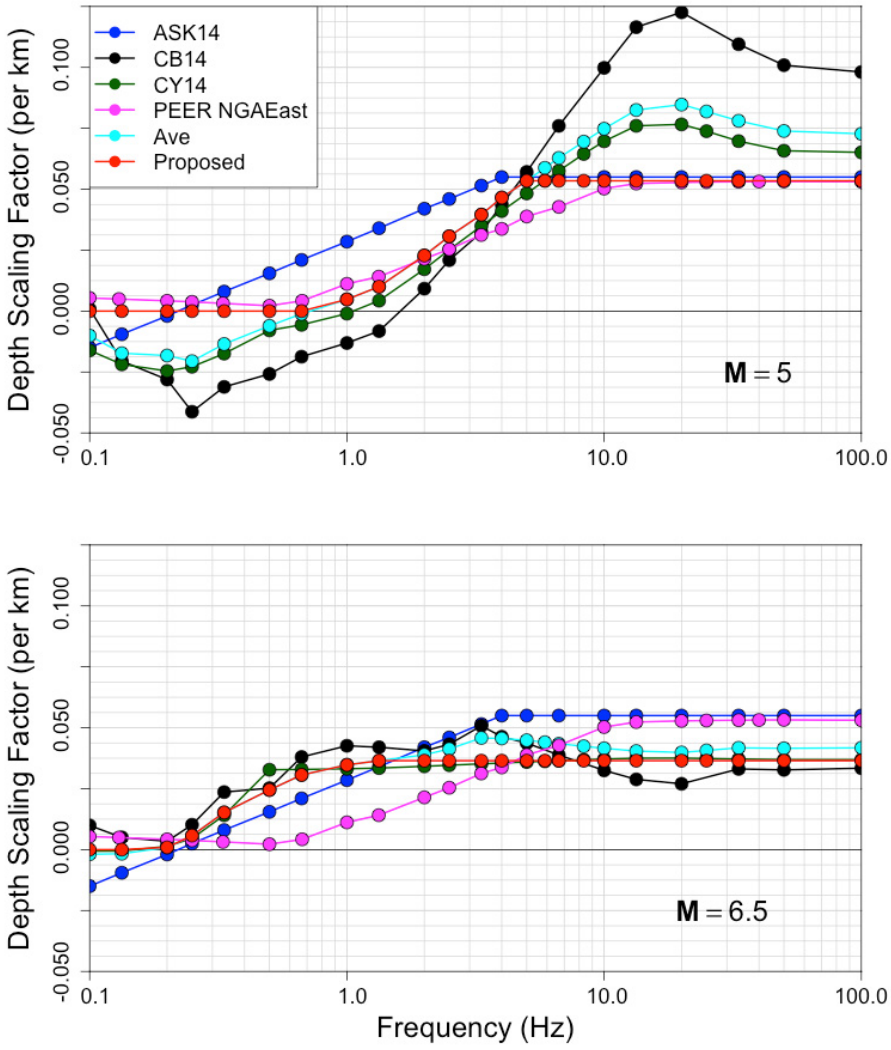

Figure 3.20 Source-depth model scaling factors for the average of the three NGA-West2 models (cyan) and the proposed source-depth adjustment model (red). The NGA-West2 models and the implied source-depth scaling factor from the PEER NGA-East model are included for comparison: CY14 in dark green, ASK14 in blue and, CB14 in black, and PEER NGA-East in magenta (top **M** = 5.0 and bottom **M** = 6.5).

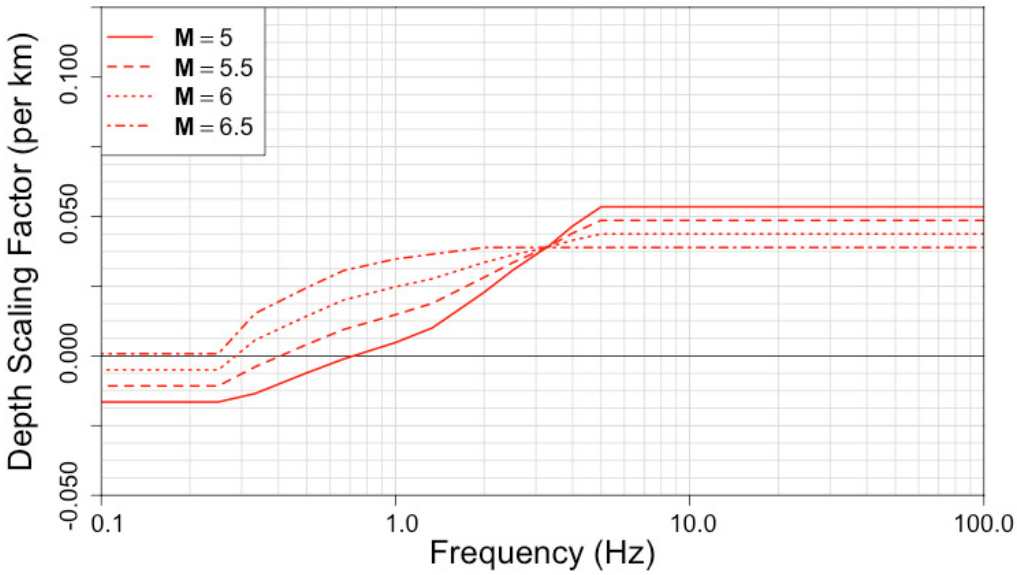

Figure 3.21 Proposed source-depth model scale factors for **M** = 5.0, 5.5, 6.0, and 6.5.

3.4.2 Centering of Source-Depth Adjustment Model

The mechanism for centering the source-depth adjustment model is required for its implementation in PSHA. A result of selecting Z_{TOR} as the source-depth metric is that large magnitude events will have shallow Z_{TOR}. In other words, large magnitude events will tend to rupture the entire seismogenic thickness of the crust, and thus have Z_{TOR} that are close to 0 km. If the source-depth adjustment model is centered on Z_{TOR} values not compatible with the magnitude and data used in the median GMM development, then the resulting ground motions could be adjusted in an inappropriate way. Therefore a magnitude-dependent centering is recommended for application. The form of the recommended centered Z_{TOR} model, ΔZ_{TOR}, is adopted from CY14, given by,

$$\Delta Z_{TOR} = Z_{TOR} - E(Z_{TOR}) \tag{3.19}$$

where $E(Z_{TOR})$ is the magnitude-dependent centering depth (magnitude-dependent expected Z_{TOR}), and Z_{TOR} is the actual depth-to-top-of-rupture of the earthquake source, as provided in a SSC model. Based on the results presented in Section 3.2, the recommendation is to cap the depth adjustment to a maximum of 10 km ΔZ_{TOR} (i.e., provide the maximum depth-effect adjustments when ΔZ_{TOR} reaches 10 km).

The median NGA-East GMMs did not explicitly include a depth term, requiring the model development described above. Rather, the GMMs are deemed applicable to the *expected* range of depths in CENA. Separate tasks are currently underway to (1) quantify the depth ranges from the CEUS SSC and (2) further evaluate the impact of differences in median GMM depth assumptions. The results of these tasks will be documented in the NGA-East project final report. Meanwhile, the interim model described below was developed to address this issue, and is recommended for use.

CEUS SSC-Based Magnitude Dependence of Z_{TOR} (Interim Model)

A relationship to predict the mean Z_{TOR} as a function of magnitude was developed [Youngs, *personal communication*, 2015] based on: rupture geometries from NUREG-2115 Chapter 5, earthquake source depths from the NGA-East database, a distribution of hypocentral depth ratios from Chiou and Youngs [2008], and the rupture-area relationship from Somerville [2014]. This relationship was originally developed to convert median GMMs that used R_{JB} to R_{RUP}. The relationship is used here to help guide how the source-depth adjustment model is centered. The development of this model is as follows

1. An average hypocentral depth of 10 km is assumed for CENA. This assumption is based on the average of hypocentral depths in the NGA-East flatfile, 12 km, and the mode of the hypocentral depth distribution published in Chapter 5 of NUREG-2115, 8 km.
2. A dip angle for events in CENA is assumed to be 75° for strike–slip and 45° for reverse earthquakes. This is based on Table 5.4-1 of NUREG-2115, which states that the default characteristics of CENA earthquakes are a mixture of strike-slip and reverse at a ratio of 2 to 1 with median dip angles of 75° and 45°, respectively.
3. The location of the hypocenter and down dip on the rupture plane is defined based on the distribution of the fractional depth from the top of rupture of the hypocenter given in Appendix B of Chiou and Youngs [2008]. The mean of this distribution is used and is 0.6375 for strike–slip and 0.628 for reverse earthquakes.
4. The thickness of the seismogenic crust in CENA is assumed to be 17 km. This is the central branch of the of the seismogenic thickness logic tree in NUREG-2115.
5. Rupture area as a function of magnitude is assumed to follow the Somerville [2014] relationship. The rupture aspect ratio is assumed to be 1:1 (from Table 5.4-1 of NUREG-2115).
6. Using a hypocenter depth of 10 km, the specified dips, average hypocenter depth ratios, rupture area relationship, and aspect ratio, the nominal depth to the top and bottom of ruptures is calculated a range of magnitude from **M** = 4.0–8.0.

The results of this model are summarized in Table 3.3 and plotted in Figure 3.22 along with $E(Z_{TORi})$, the mean Z_{TOR} used for centering in the CY14 source-depth scaling model. Based on the assumptions listed above, Z_{TOR} reaches 0 before the bottom of the rupture reaches the full seismogenic thickness of the crust. Therefore, for large-magnitude events the mean value of Z_{TOR} reaches 0. The two relationships plotted in Figure 3.20 have significantly different shapes. For strike–slip events both relationships predict a 0 Z_{TOR} at similar magnitudes (~6.7) but have differing predictions below this magnitude. For reverse earthquakes, the relationships have similar predictions in the **M** = 6.0–6.7 range but differ outside that range.

Table 3.3 Magnitude dependence of Z_{TOR} from the CEUS SSC (interim model).

M	Z_{TOR} strike–slip (km)	Z_{TOR} reverse (km)	Z_{TOR} average (km)
4	9.54	9.67	9.60
4.1	9.48	9.63	9.55
4.2	9.42	9.58	9.50
4.3	9.35	9.53	9.44
4.4	9.27	9.47	9.37
4.5	9.18	9.41	9.29
4.6	9.08	9.34	9.21
4.7	8.97	9.25	9.11
4.8	8.84	9.16	9.00
4.9	8.70	9.06	8.88
5	8.54	8.95	8.74
5.1	8.36	8.82	8.59
5.2	8.16	8.67	8.42
5.3	7.94	8.51	8.22
5.4	7.69	8.33	8.01
5.5	7.40	8.13	7.77
5.6	7.09	7.90	7.49
5.7	6.73	7.64	7.19
5.8	6.33	7.35	6.84
5.9	5.88	7.03	6.46
6	5.38	6.67	6.03
6.1	4.82	6.26	5.54
6.2	4.19	5.81	5.00
6.3	3.48	5.30	4.39
6.4	2.68	4.72	3.70
6.5	1.79	4.08	2.93
6.6	0.79	3.36	2.07
6.7	0.00	2.55	1.27
6.8	0.00	1.64	0.82
6.9	0.00	0.61	0.31
7	0.00	0.00	0.00
7.1	0.00	0.00	0.00
7.2	0.00	0.00	0.00
7.3	0.00	0.00	0.00
7.4	0.00	0.00	0.00
7.5	0.00	0.00	0.00
7.6	0.00	0.00	0.00
7.7	0.00	0.00	0.00
7.8	0.00	0.00	0.00
7.9	0.00	0.00	0.00
8	0.00	0.00	0.00
8.1	0.00	0.00	0.00
8.2	0.00	0.00	0.00

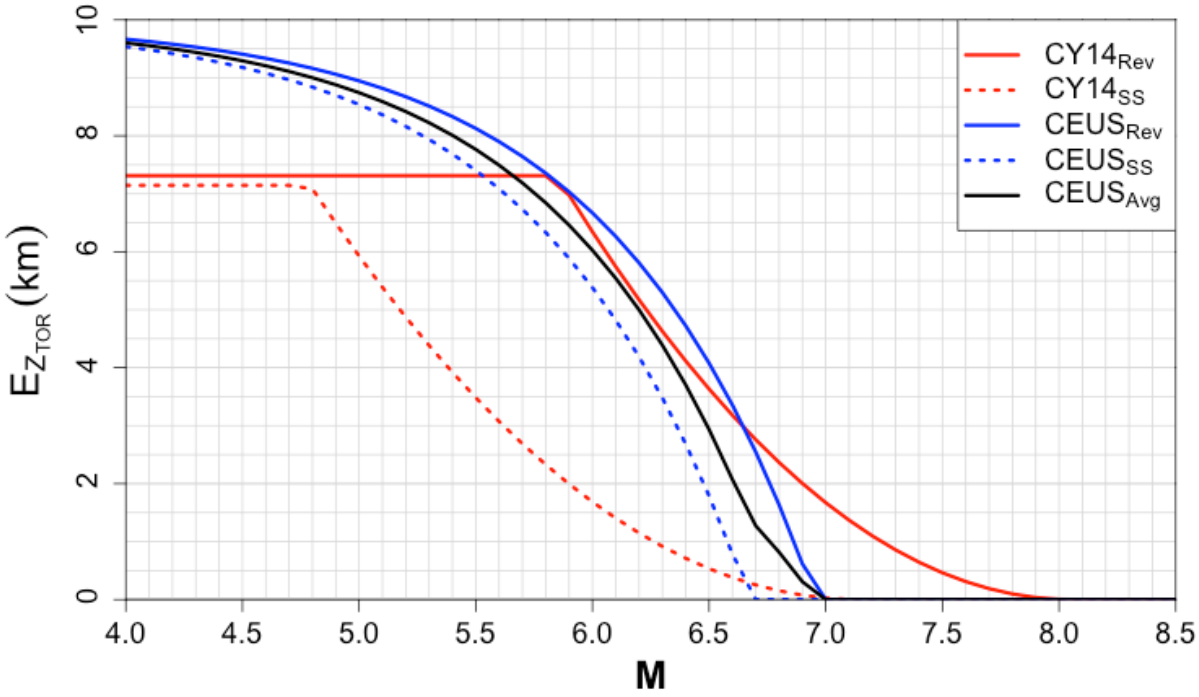

Figure 3.22 Expected values of Z_{TOR} from NGA-West2 (Chiou and Youngs [2014]) and for the CEUS region.

4 Adjustment for Gulf Coast and Mississippi Embayment Region

Justin Hollenback

Pacific Earthquake Engineering Research Center
University of California, Berkeley

Walter J. Silva

Pacific Engineering and Analysis
El Cerrito, California

Robert B. Darragh

Pacific Engineering and Analysis
El Cerrito, California

Norman A. Abrahamson

Pacific Gas & Electric Company
San Francisco, California

4.1 INTRODUCTION

This chapter summarizes the development of a pair models for adjusting the suite of NGA-East GMMs [PEER 2015] to be applicable in the Gulf Coast/Mississippi Embayment (Gulf Coast, GC) region. The NGA-East regionalization task [Dreiling et al. 2014] confirmed that the Gulf Coast region (Region 1) had crustal properties leading to significantly different ground motions when compared to the other three regions in CENA (Section 1.3.3, Figure 1.1). These findings are consistent with previously published work by EPRI [1993, 2004], although the specific geographic boundaries of the various regions are not exactly the same in all the studies.

The NGA-East GMMs were developed for the vast CENA region that excludes the Gulf Coast, referred to as the mid-continent (MC) region, with most models developed or calibrated using Region 2 data (Figure 1.1). This chapter provides alternate models for adjusting the median GMMs to be applicable for use in the Gulf Coast. The two models adopt slightly different approaches. One uses an empirically based approach and models differences in ground motions between data collected in the Gulf Coast region and the PEER NGA-East median ground

motions (developed for the mid-continent, using data from Region 2). The other is a theoretical-based approach using the point-source stochastic model, which is constrained by data inversions from the Gulf Coast region.

Both suites of adjustments are provided in the form of ratios of PSA, which are defined as:

$$f(\theta) = \frac{PSA_{GC}}{PSA_{MC}} \tag{4.1}$$

where PSA_{GC} and PSA_{MC} are the PSA values from the GC and MC regions, respectively, and θ is the set of predictive parameters. The two development groups for GC adjustment models are the PEER group (authors of Chapter 11, PEER [2015]) and, DASG (authors of Chapter 3 in the previous PEER report [2015]). Both of these adjustment models are described in later sections of this chapter. The ratios from each group are provided in Electronic Appendix B in tabular form. To adjust ground-motion values from the mid-continent to the Gulf Coast region requires multiplying the original median GMM predictions by the Gulf Coast ratios provided in the appendix.

The Gulf Coast models can be used as-is when the complete path (source, travel path, and site) is contained in the Gulf Coast. Rules for the treatment of paths including a regional boundary crossing (between the mid-continent and the Gulf Coast) are being developed in a separate task. The recommendations for boundary crossing cases will be published in the final NGA-East report.

4.1.1 Overview of Available Gulf Coast Data in the NGA-East Database

The data available in the NGA-East database [Goulet et al. 2014] that are in Path Region 1 (both the earthquake source and the site located in the GC) are relatively sparse. Figure 4.1 shows the magnitude and distance ranges covered in the NGA-East database for the GC region.

Table 4.1 lists the events that occurred in the GC region along with the respective moment magnitudes (**M**), hypocentral depths (Z_{HYP}) in kilometers, whether or not the event was designated as "Potentially Induced" by the USGS, the range of rupture distances (R_{RUP}) in kilometers, and the range of average shear-wave velocities in the upper 30 m of the site (V_{S30}) in meters per second.

In addition to limited coverage of observed ground motion in magnitude and distance, the number of records available is dependent on the frequency of PSA. Figure 4.2 shows the number of events, stations, and records available at each frequency of PSA. The paucity of data made the development of GMM models directly from the GC region data difficult. Instead, the NGA-East team favored developing two models to provide adjustments to the existing GMMs for applicability to the GC, effectively borrowing the correlations built into the median GMMs for the MC region. With these two new models, which can be applied to any of the existing GMMs for the GC region, the complete CENA region can be covered, providing the same range of epistemic uncertainty as the GMMs for the MC. The two models are described in detail below.

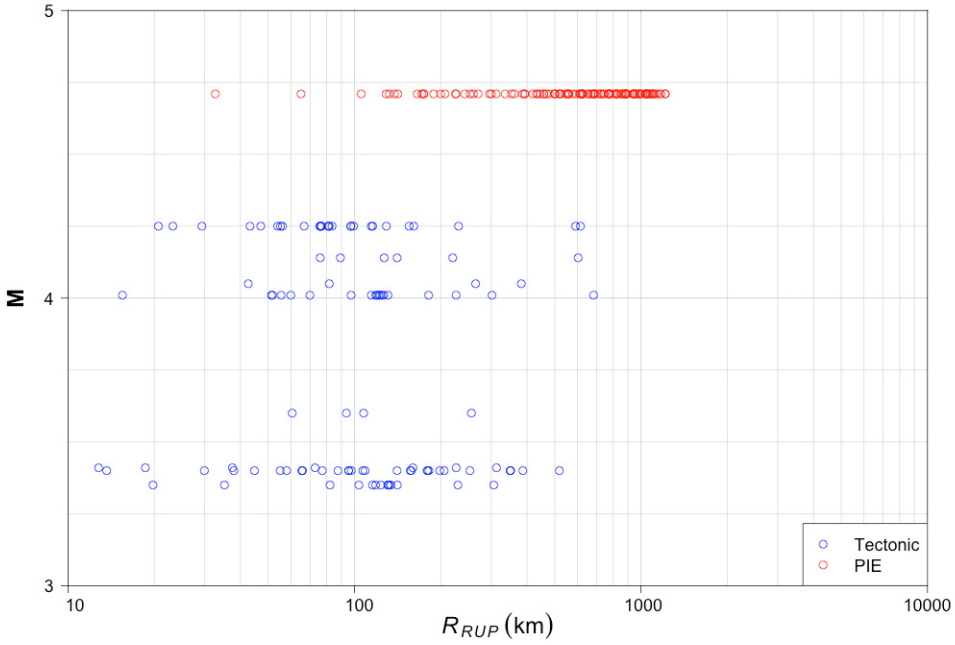

Figure 4.1 Magnitude (**M**) and rupture distance (R_{RUP}) ranges for records in the NGA-East database from Path Region 1 (i.e., both the earthquake source and the site are located in the GC region).

Table 4.1 Summary of events recorded in Region 1 (GC), including station distance and site conditions. All events used for the PEER model development; only events marked with * next to the EQ I.D. used for the DASG model.

EQ Name	EQ I.D.	M	Z_{HYP} (km)	PIE	R_{RUP} (km)	V_{S30} (m/sec)
Blytheville 2003-04-30	22	3.6	23	No	60.62 - 255.93	235.2 - 1288
Bardwell 2003-06-06	23	4.05	1.25	No	42.58 - 382.1	235.2 - 1288
MilliganRdg 2005-02-10	31	4.14	15	No	75.91 - 603.34	235.2 - 1288
ShadyGrove 2005-05-01	33*	4.25	8	No	20.68 - 614.84	185 - 1288
Miston 2005-06-02	34*	4.01	15	No	15.49 - 683.17	185 - 1288
Ridgely 2006-09-07	38*	3.35	7	No	19.8 306.21	185 - 1288
Marston 2006-10-18	41*	3.41	8.2	No	12.79 - 313.1	210 - 1288
Whiting 2010-03-02	58*	3.4	5	No	13.64 - 518.85	160 - 1288
Comal 2011-10-20	92*	4.71	4	Yes	32.68 - 1216.91	217.6 - 1288

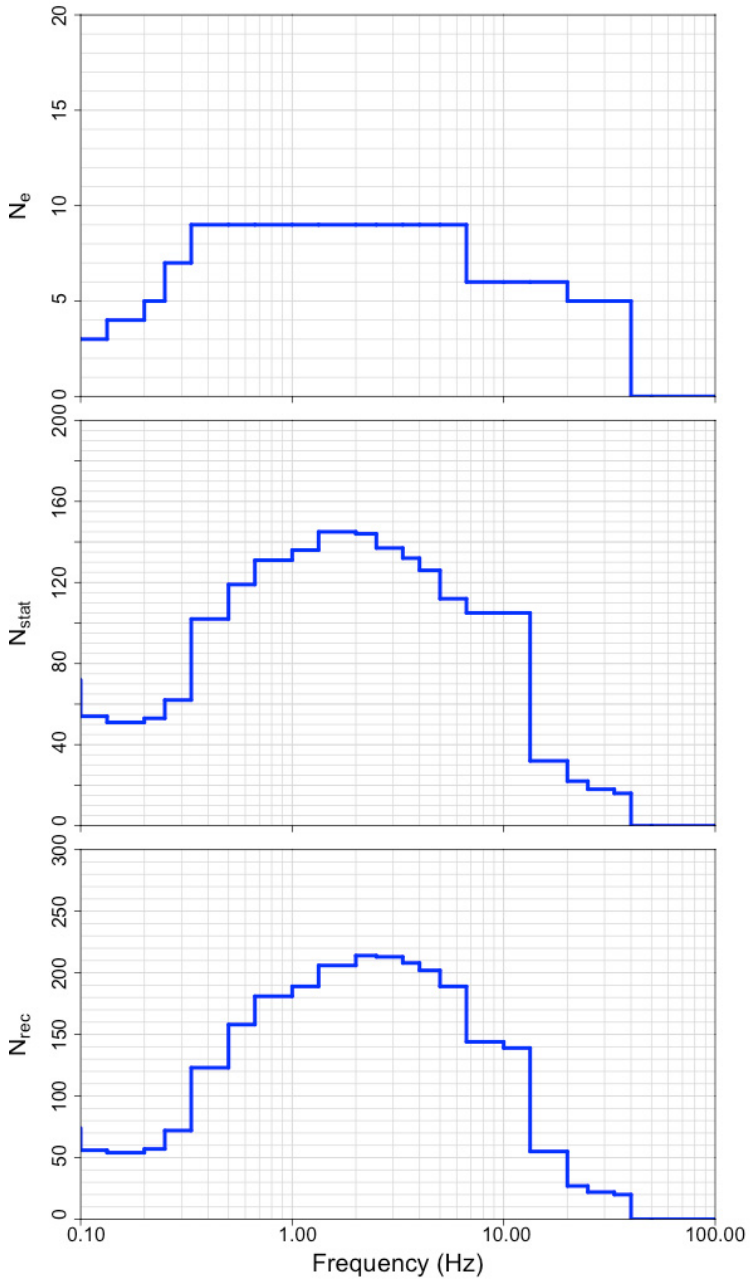

Figure 4.2 Number of events (N_e), stations (N_{stat}) and, records (N_{rec}) per frequency of PSA for Region 1 (GC).

4.2 PEER GULF COAST ADJUSTMENT MODEL

The PEER Gulf Coast adjustment model (PEER GC) is based on observed differences between the PEER NGA-East median GMM and data from Path Region 1 (GC) in the NGA-East database. This model, similar to traditional GMMs, is fit one frequency at a time. The main motivation of this approach was to derive an adjustment model that was empirically driven.

4.2.1 Overview of PEER NGA-East Median GMM

The PEER NGA-East median GMM is described in detail in the NGA-East Median GMM Report [PEER 2015] and is summarized briefly here. The primary feature of the model is that it is empirically derived on the FAS of acceleration for the limited magnitude, distance, and frequency range provided in the NGA-East database. The model is then extended to frequencies above and below the band limitations present in the data using simple point-source shapes and extrapolated to large-magnitude and close-distance earthquakes using finite-fault simulations from the Southern California Earthquake Center (SCEC) broadband platform. All of the extrapolation and extension is performed on the FAS of acceleration. Random vibration theory (RVT) is then used to predict PSA for any magnitude–distance combination; RVT is a technique that uses the frequency content of a recorded ground motion to calculate the peak response of single-degree-of-freedom damped oscillators. This technique required the development of a calibrated duration model. The PEER NGA-East median GMM is a model that predicts PSA and PGA for CENA Region 2 out to 400 km and for **M** = 4–8.2.

4.2.2 Selection of Data

The PEER modeling group selected all events in the GC region for the analysis, which includes eight tectonic events and one event designated "potentially induced" by the USGS. Records used in analysis were limited to $R_{RUP} \leq 400$ km. No limits were specified for V_{S30} in order to retain as many records as possible and to be consistent with the MC PEER NGA-East GMM. Figure 4.3 shows the numbers of events, stations, and records used plotted against frequency. This plot illustrates the amount of data that is lost by screening records based on distance.

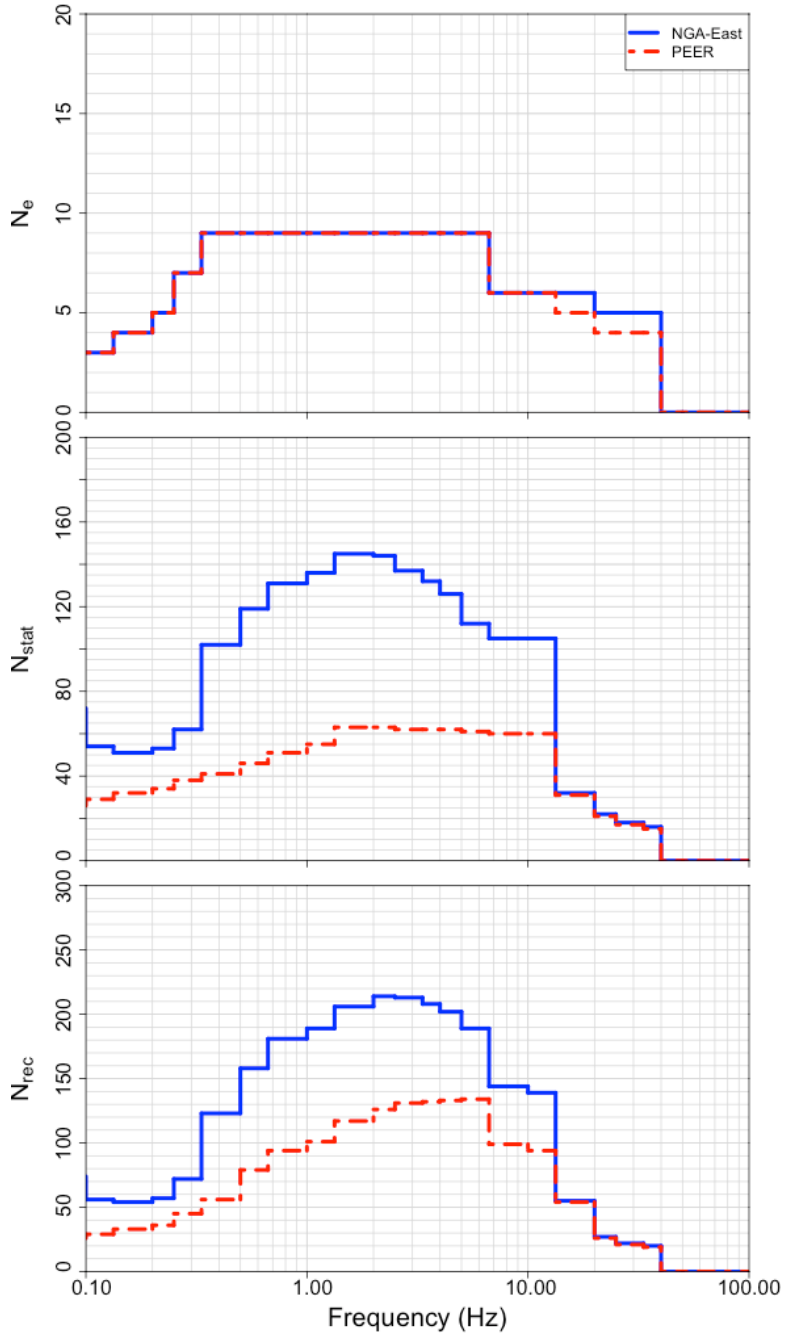

Figure 4.3 Comparison of the number of events (N_e), stations (N_{stat}), and records (N_{rec}) available per PSA frequency from the NGA-East database (solid blue line) and the subset of records used by the PEER modeling group (dashed red line).

4.2.3 Model Development

The PEER GC adjustment model is an empirically-based model. It was derived by modeling the total residual of the selected ground-motion records from the GC region relative to the PEER NGA-East median GMM. The total residual is defined as:

$$\delta_{1,i,j} = \ln\left(y_1\right)_{i,j} - \ln\left[Y_2\left(\mathbf{M}_i, Z_{HYP,i}, R_{RUP,i,j}, V_{S30,j}\right)\right]_{i,j}$$
$$\delta_{1,i,j} = \ln\left[\frac{y_1}{Y_2\left(\mathbf{M}_i, Z_{HYP,i}, R_{RUP,i,j}, V_{S30,j}\right)}\right]_{i,j} \quad (4.2)$$

where $\delta_{1,i,j}$ is the total residual of GC data from event *i* and station *j*, $y_{1i,j}$ is the observed PSA of GC data, and $Y_{2,i,j}$ is the median estimate of PSA at event *i* and station *j* using the PEER NGA-East median GMM. The total residuals are plotted against R_{RUP} in Figure 4.4 for PSA at frequencies 0.5, 1.0, 5.0, and 10.0 Hz.

The total residuals, $\delta_{1,i,j}$, plotted against R_{RUP} (Figure 4.4) reveal two prominent trends that are common across frequency:

1. The slope of the locally weighted least-squares fit (red curve) does not deviate much from 0 for $R_{RUP} \leq 100$ km.
2. Beyond 100 km, the slope of the locally weighted least-squares fit is generally linear and is negative with respect to R_{RUP}.

Based on these observations the following functional was selected to fit to $\delta_{1,i,j}$.

$$\Delta_1 = \begin{cases} c_0 & R_{RUP} < 100 \text{ km} \\ c_0 + c_7'\left(R_{RUP} - 100\right) & R_{RUP} \geq 100 \text{ km} \end{cases} \quad (4.3)$$

where Δ_1 is the predicted geometric difference in the ground motion between Regions 1 and 2, which is equivalent to the natural log of the PSA ratio in Equation (4.1), and c_0 and c_7' are empirically-derived model coefficients. This functional form assumes that any differences present between the two regions is entirely attributable to a difference in the linear distance attenuation and ignores any potential differences related to source or site effects. This somewhat simplistic assumption is required because of the sparse nature of the data available.

The coefficients in Equation (4.3) were obtained using mixed-effects regression and included a random effect on the coefficient c_0 grouped by event (the between-event residual). Regression was applied in two different ways:

- Empirical Model 1 (EM1): Forcing the fixed effect $c_0 = 0$ (fixed effect is known *a priori*) and solving for the random effects on c_0 and the fixed effect c_7.
- Empirical Model 2 (EM2): Allowing the fixed effect c_0 to be a free parameter in the regression along with the event terms and the fixed effect c_7'.

The fitting of the data was performed in these two ways in an attempt to deal with the sparse amount of data from $R_{RUP} < 100$ km. These data have a large influence on the coefficient c_0 but may not be representative of real differences in ground motion between the two regions.

Figures 4.5 and 4.6 show the model coefficients plotted against frequency for the two regressed models EM1 and EM2 as well as those for the proposed model discussed below. Figure 4.7 shows the between-event residuals for frequencies 0.5, 1.0, 5.0, and 10 Hz for the same models.

Figure 4.7 shows that the between-event residuals for EM1 for 5.0 and 10.0 Hz are significantly different from those of EM2 and exhibit non-zero average trend. This lack of centering causes τ_1 to be larger for EM1 than for EM2 (Figure 4.8), which has a non-zero c_0 term.

Figures 4.9 and 4.10 show the within-event residuals for a range of frequencies of PSA and for EM1 and EM2, respectively. In general for both models, the within-event residuals show no significant trend with R_{RUP}. Figure 4.11 shows that there are negligible differences in the within-event residuals between the two models. This trend is also observed in Figure 4.6, which shows negligible differences in the model coefficient c_7' with frequency.

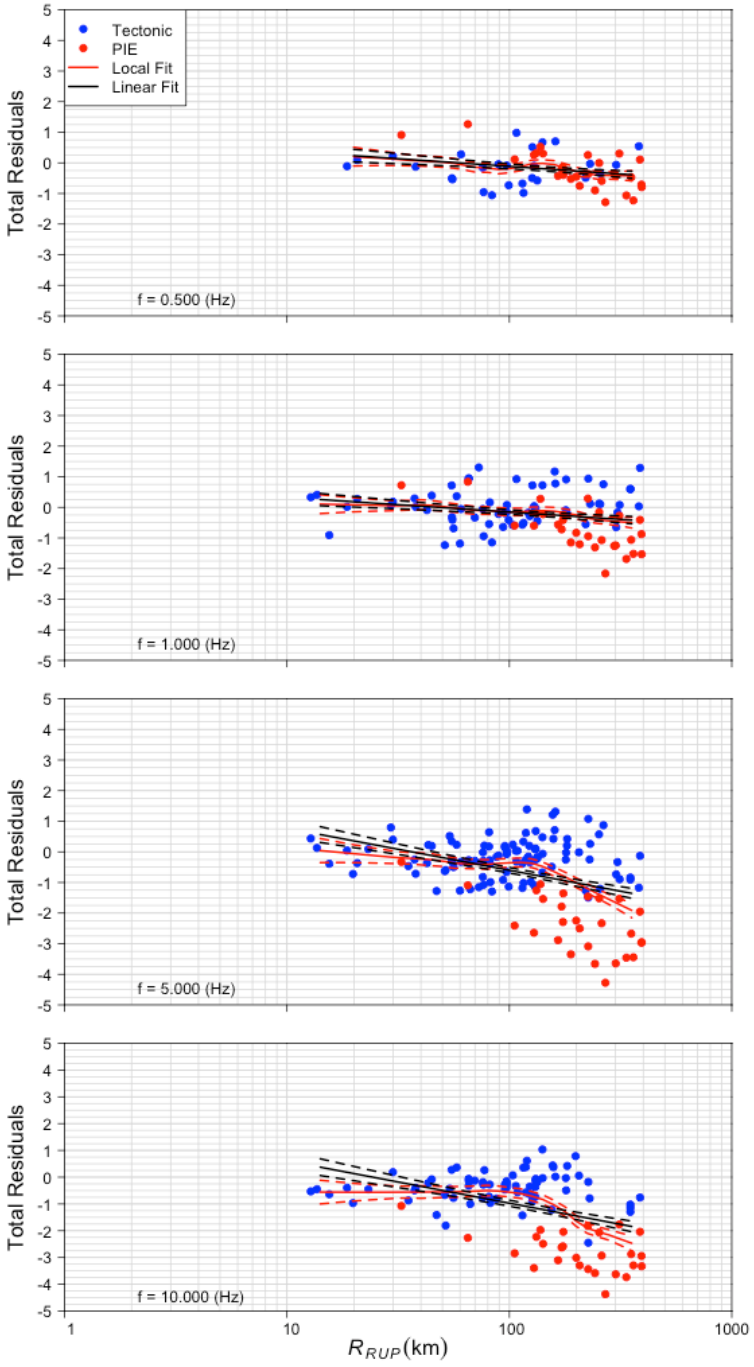

Figure 4.4 Total residuals plotted against rupture distance for PSA at frequencies 0.5, 1.0, 5.0, and 10.0 Hz. Blue points are observations from tectonic events, and red points are observations from PIE. The black lines represent a linear fit to the data with ± standard error in dashed lines. The red lines represent a locally weighted least-squares fit to the data with ± standard error in dashed lines.

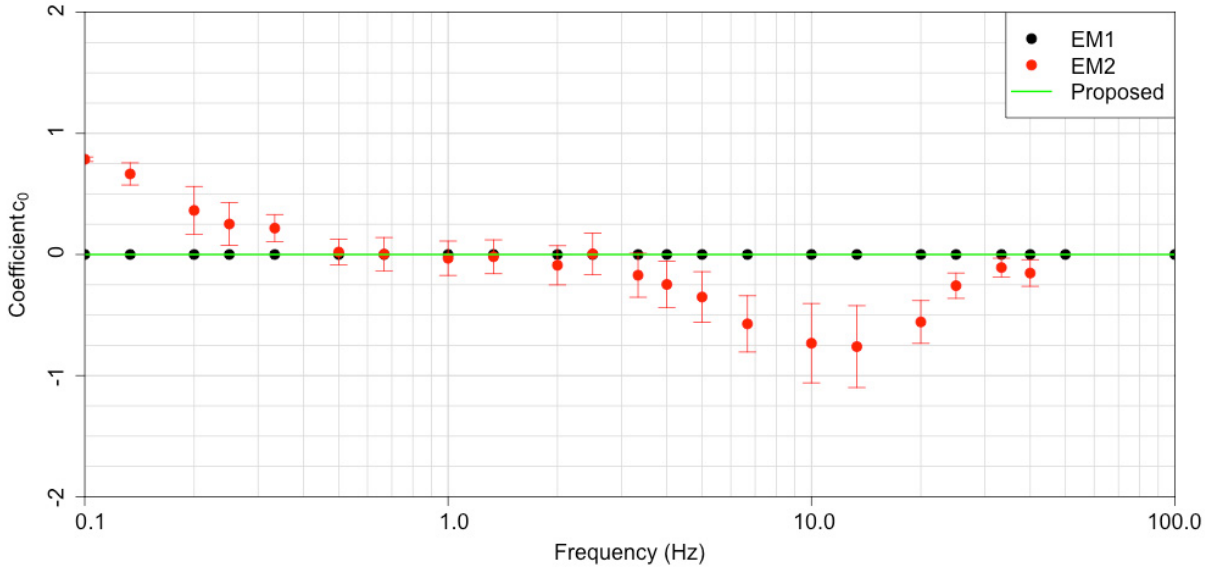

Figure 4.5 Comparison of model constant, c_0, for EM1 (black), EM2 (red), and the proposed model (green) plotted against frequency of PSA. Note that coefficient c_0 value is equal to zero for EM1 and the proposed model.

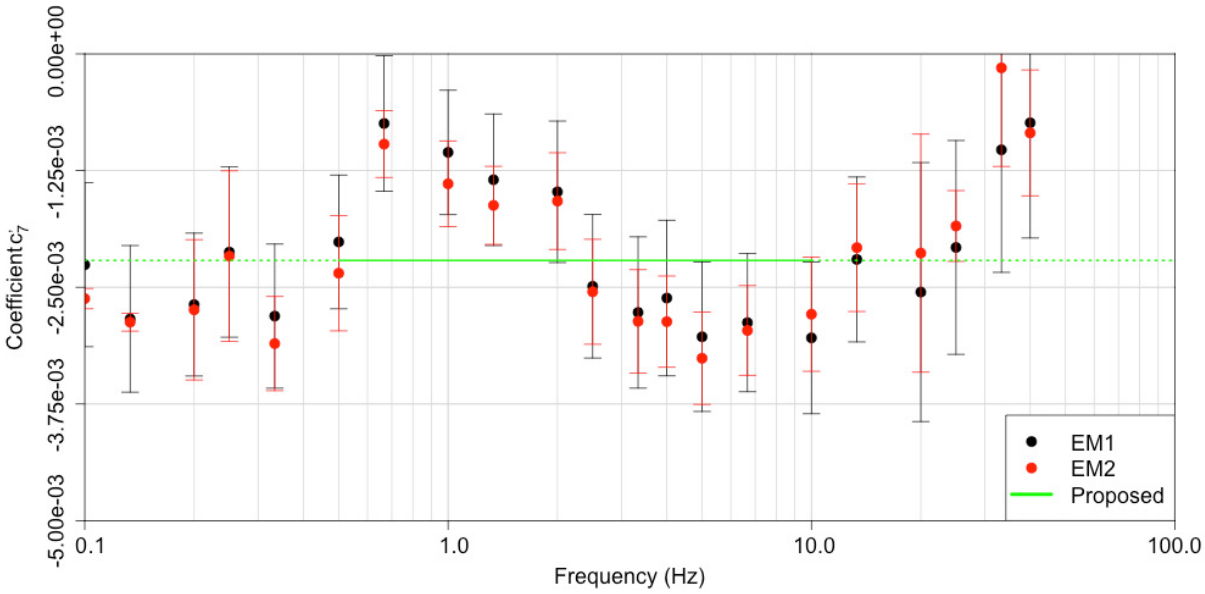

Figure 4.6 Comparison of model coefficient, c_7', for EM1 (black), EM2 (red), and the proposed model (green) plotted against frequency of PSA. The c_7' for the proposed model are taken as the average of points from EM1, taken in the 0.5–10 Hz range, where the data is deemed more reliable.

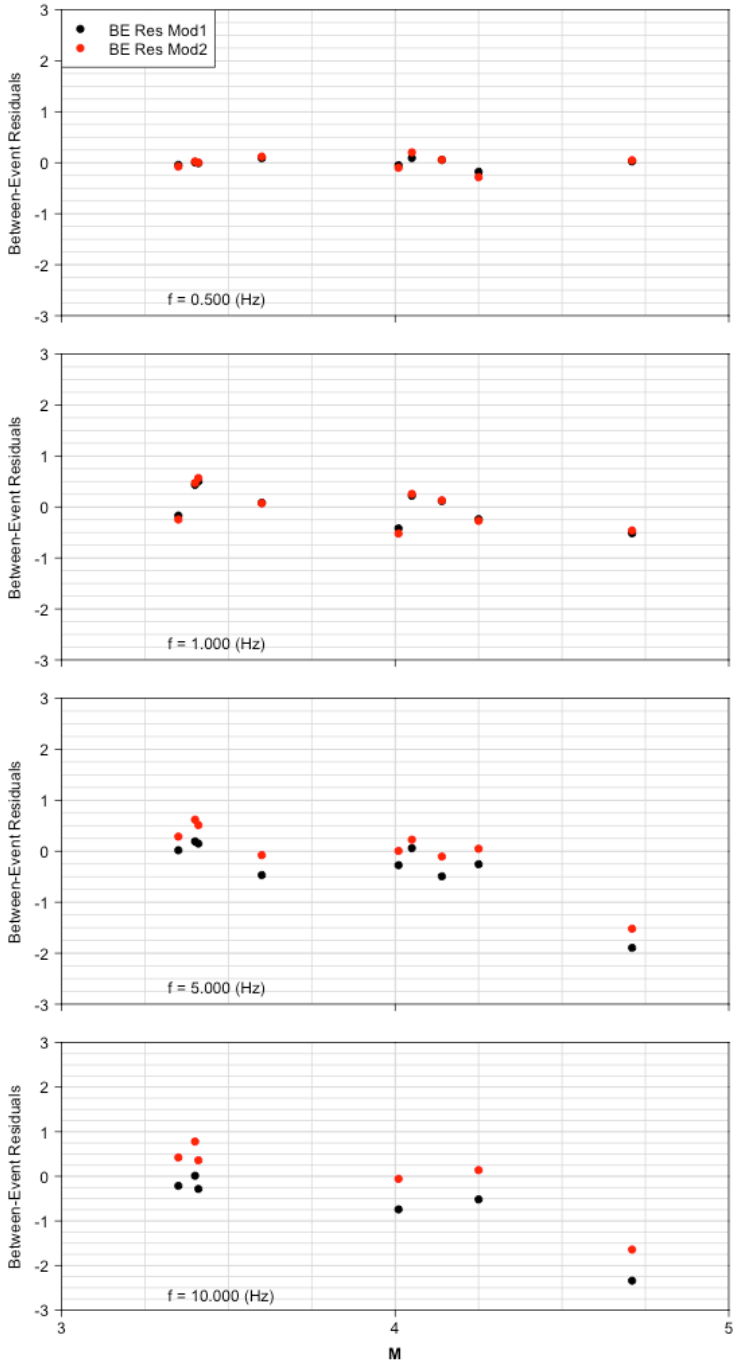

Figure 4.7 **B**etween-event residuals for EM1 (black points) and EM2 (red points) plotted against magnitude for PSA at frequencies 0.5, 1.0, 5.0, and 10.0 Hz. The largest event (**M**4.71) is a PIE, all other events are tectonic.

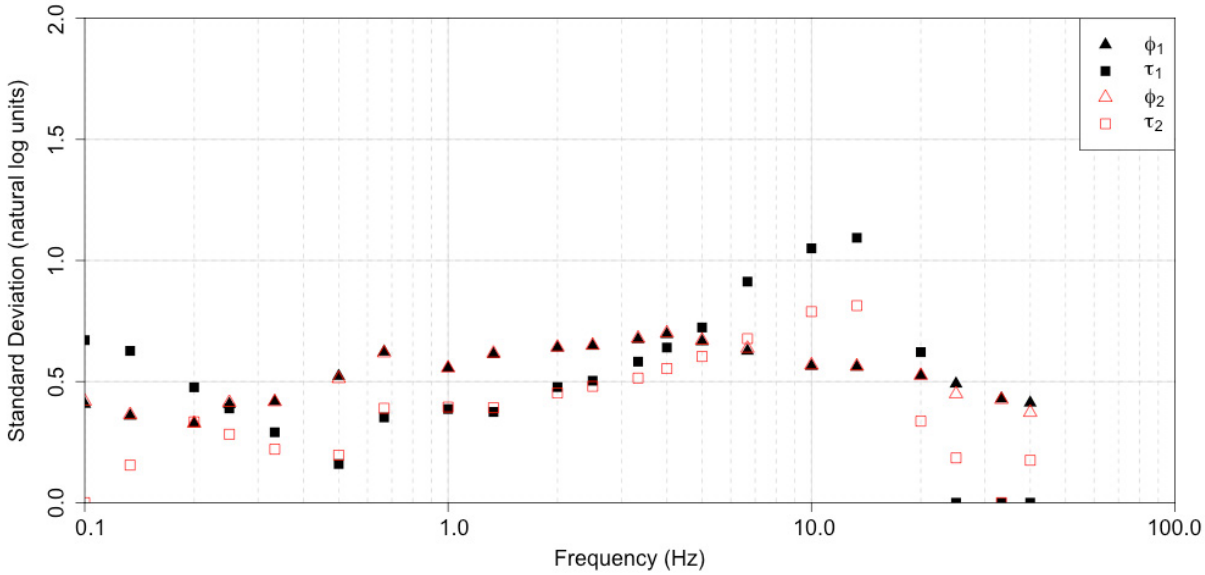

Figure 4.8 Between-event (squares), and within-event (triangles) standard deviations for EM1 (solid black points) and EM2 (open red points) plotted against frequency of PSA.

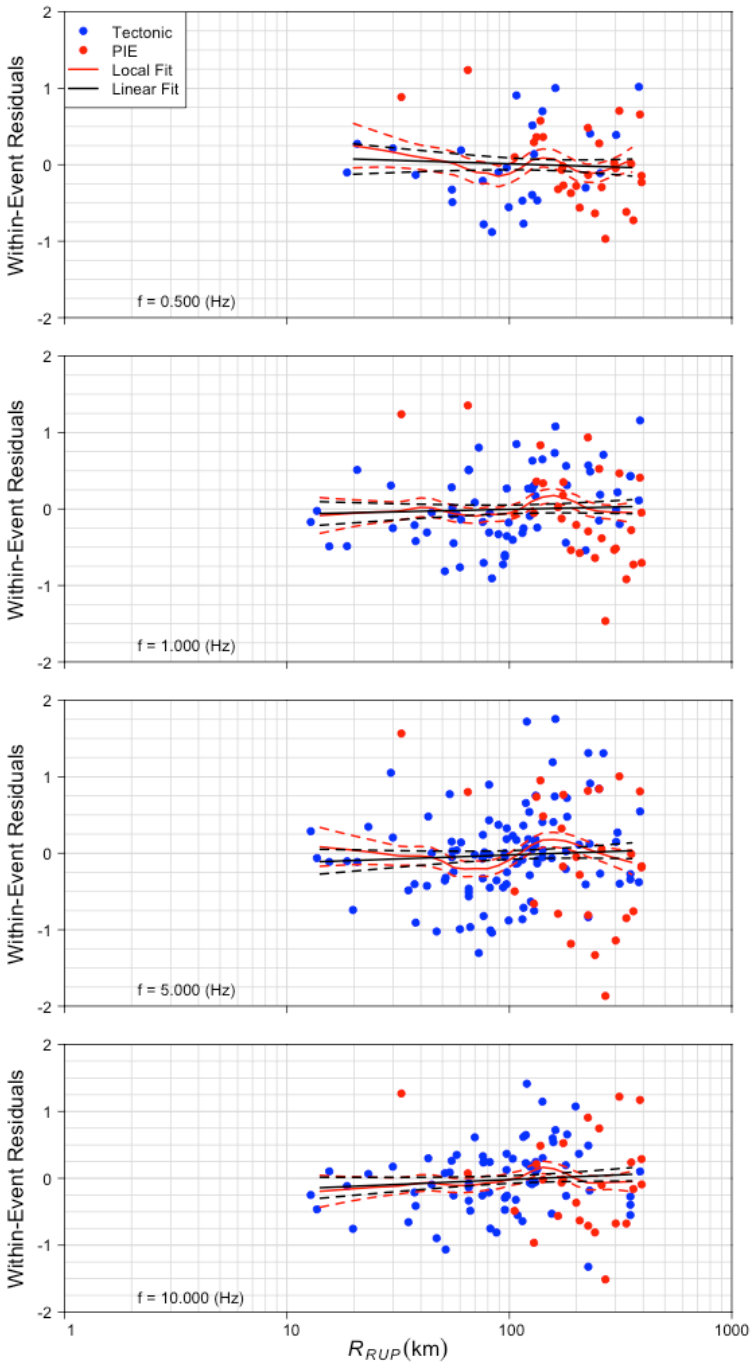

Figure 4.9 Model 1 within-event residuals plotted against rupture distance for PSA at frequencies 0.5, 1.0, 5.0, and 10.0 Hz. Blue points are observations from tectonic events, and red points are observations from PIE.

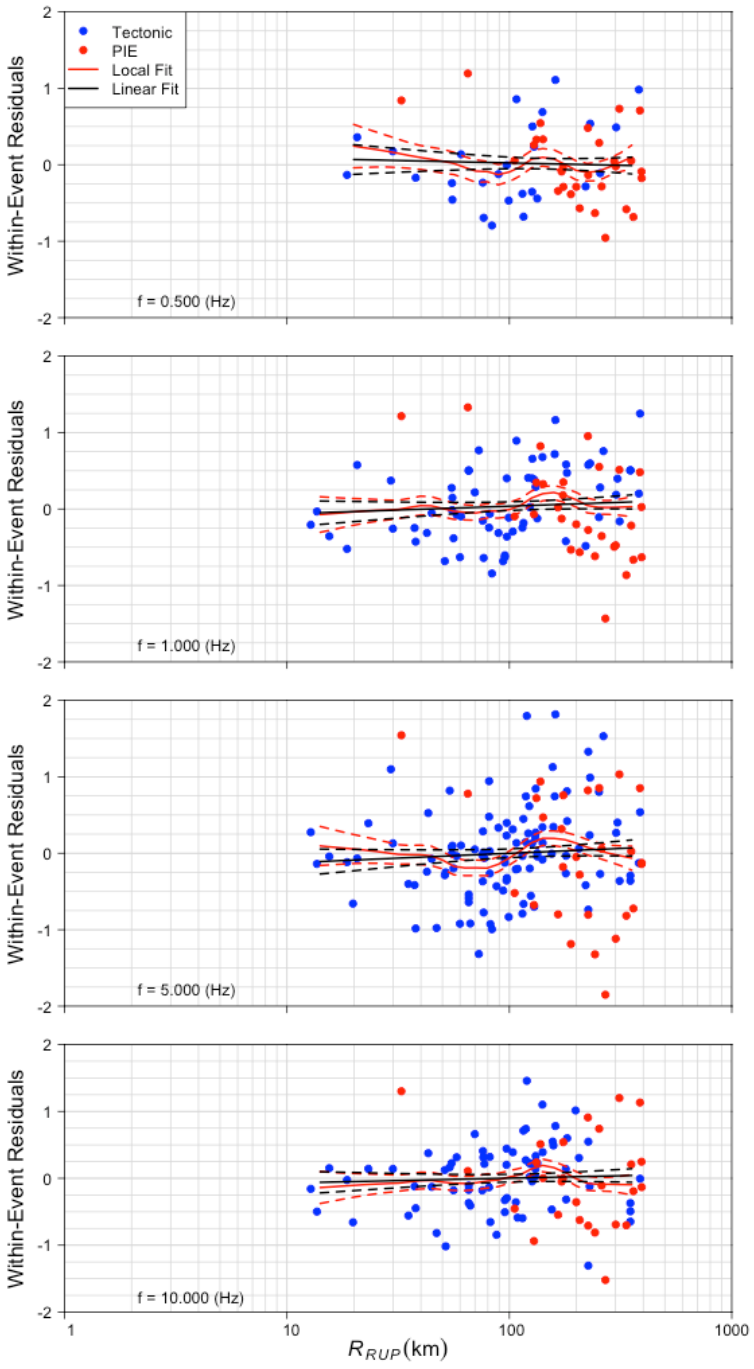

Figure 4.10 Model 2 within-event residuals plotted against rupture distance for PSA at frequencies 0.5, 1.0, 5.0, and 10.0 Hz. Blue points are observations from tectonic events, and red points are observations from PIE.

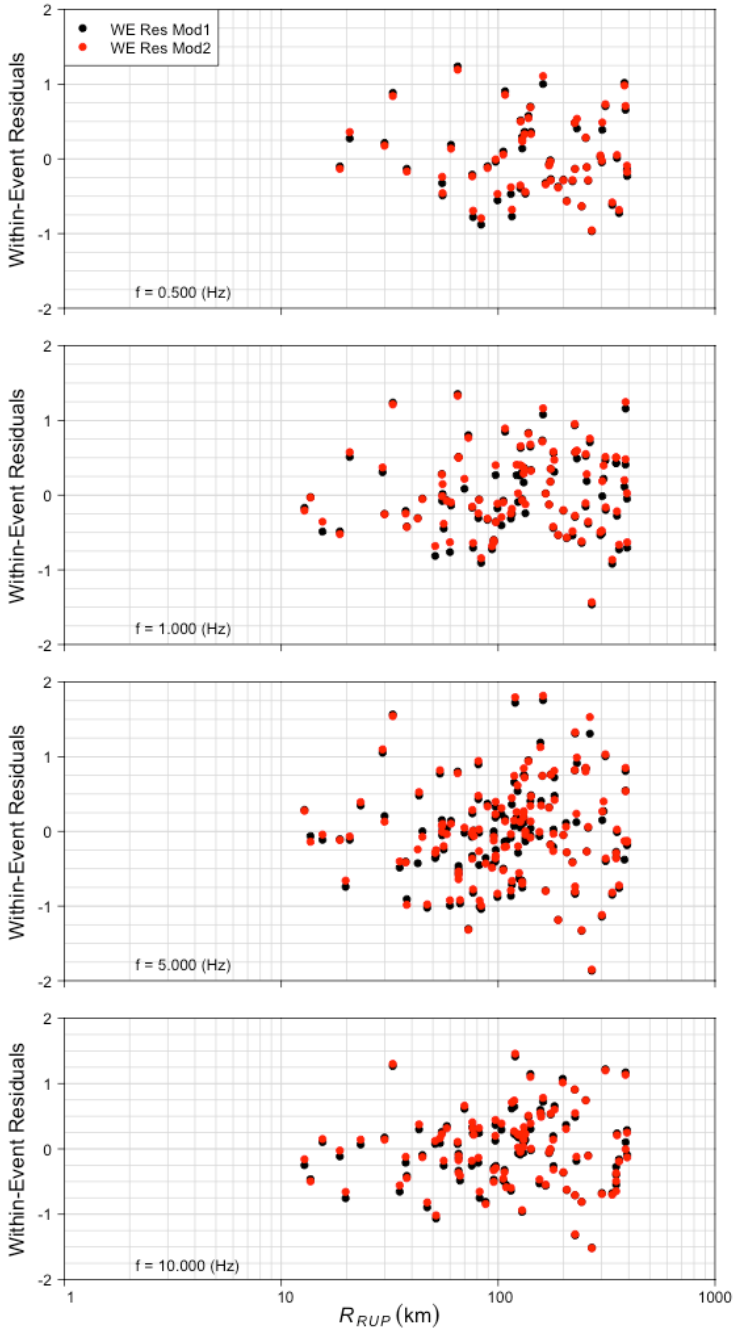

Figure 4.11 Within-event residuals for EM1 (black points) and EM2 (red points) plotted against rupture distance for PSA at frequencies 0.5, 1.0, 5.0, and 10.0 Hz.

The computed residuals for the Gulf Coast records show a dip in the mean residuals in the vicinity of 10 Hz, which is visible in the c_0 trends in EM2 (Figure 4.5). This dip is attributed to a systematic site effect. The ground-motion residuals were computed with respect to the mid-continent model. Systematic differences in ground motions will manifest themselves as trends in the mean event terms. Such trends can be attributed to systematic differences in the earthquake

source between Gulf Coast earthquakes and mid-continent earthquakes, or systematic differences in site effects between the two regions for the same V_{S30} classification, or both. Random-effects regression cannot distinguish between the two. Because the dip in mean residuals is somewhat narrow banded, it is judged to be much more likely to be due to differences in the average site effect rather than average differences in the earthquake sources (i.e., differences in stress parameter); it should not be used to model differences in ground motions for hard-rock site conditions.

Based on these observations and interpretations, a new proposed model was developed based on EM1 where:

1. The coefficient c_0 follows the shape of EM1 for the whole frequency range (fixed at 0).
2. The coefficient c_7' is the average of c_7' across EM1 and across frequency from 0.5 to 10 Hz.

This proposed model is shown on Figures 4.5 and 4.6 and provides apparent advantages over the fully regressed EM1 for several reasons. First, there is a relatively large drop in the number of records available below 0.5 Hz. In the low-frequency range, there is also potentially a data truncation issue, where only larger ground motions have high enough signal-to-noise ratio to pass through record processing. Second, above 40 Hz there is not sufficient data to empirically model the differences in ground motions. Third, the averaging of c_7' is selected to be over a frequency range where the data is relatively plentiful. Averaging was preferred given the lack of information beyond the 0.5–10 Hz band to inform the modeling of the complex shape apparent in Figure 4.6. Although the simplification might not reflect potentially real trends in the deviation of linear attenuation with frequency, it was selected to represent an average adjustment. Figure 4.12 shows comparisons of the PSA ratios for all three models plotted against R_{RUP} for a range of frequencies of PSA.

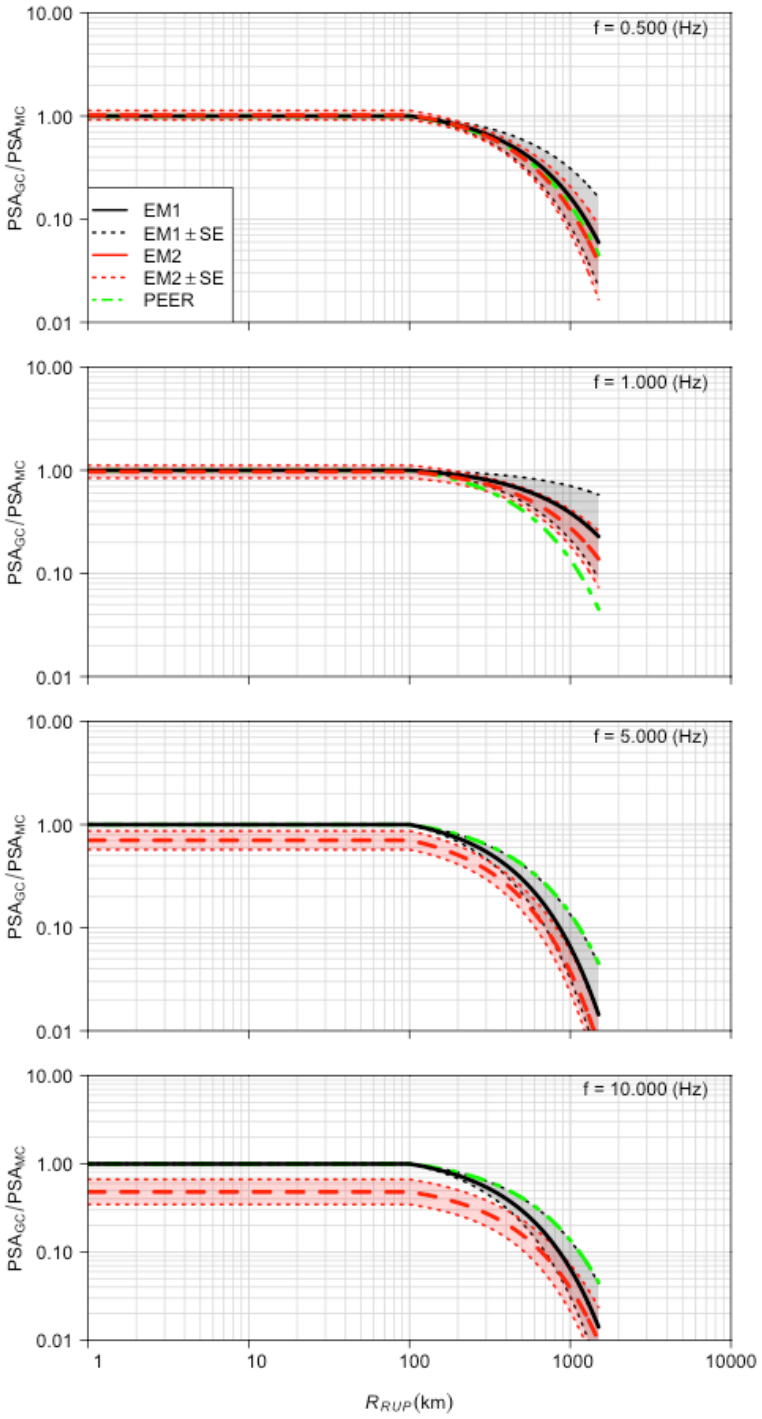

Figure 4.12 Gulf Coast adjustment ratios from EM (black), EM2 (red), and the proposed model (green) plotted against rupture distance for PSA at frequencies 0.5, 1.0, 5.0, and 10.0 Hz.

4.3 DASG GULF COAST ADJUSTMENT MODEL

The Gulf Coast model developed by Darragh, Abrahamson, Silva, and Gregor (DASG) is based on point-source stochastic simulations, as was their original model presented in Chapter 3 of the previous PEER report [2015]. The input parameters are inverted for using the NGA-East data from Path Region 1. These simulations are then used to update the DASG median GMM developed for use in Region 2. The ratio of the PSA predictions from these two GMMs is then calculated [Equation (4.1)] for a range of frequencies, magnitude, and distance. These ratios are the DASG GC adjustment model and are provided for a range of frequencies and R_{RUP} as an electronic appendix to this document.

4.3.1 Overview of DASG NGA-East Median GMM

The DASG NGA-East Median GMM is describe in detail in the NGA-East Median GMM Report [PEER 2015] and is summarized briefly here. The approach provides a suite of four separate GMMs, all of which are based on point-source stochastic simulations. The four sets of models are grouped into single- and double-corner point source models. Within each group there is a constant stress parameter model and a magnitude-dependent stress parameter model. The methodology can be summarized in three steps:

1. Invert recorded data for a subset of point source parameters: stress parameter, Q_o, and κ.
2. Generate simulations of ground-motion intensity measures PSA (for a range of oscillator frequencies), PGA, and PGV beyond the magnitude and distance range covered by the empirical data.
3. Parameterize the simulations into equations and generate PSA for required magnitude and distances.

The inversions were performed on the FAS of acceleration for the frequency range of 0.5–20 Hz. The results of the inversion were used to generate simulated values of PSA, PGA, and PGV for **M** from 4.5 to 8.5, an R_{JB} from 1 to 1000 km, and for the NGA-East Project reference site condition. The results of the four sets of simulations were fit to a simple functional form used to predict PSA at any magnitude distance combination. As was the case for the PEER models, the original DASG GMMs were developed using data from Region 2 (CNA) but were deemed applicable to the larger mid-continent region.

4.3.2 Updated Point-Source Inversions

To generate an updated suite of models for the Gulf Coast, inversions for the DASG mid-continent model were re-ran using NGA-East data from Path Region 1. Six events were selected for the inversions, one of which was designated as PIE (Table 4.1). The same crustal amplifications were used for the inversions of Region 1 data as was used for Region 2 data. The results from these inversions provide approximately a 50% reduction in Q_o from that of Region 2. This updated Q_o was used to generate point source stochastic simulations, which were used to develop the adjustment for the linear distance attenuation coefficient of the mid-continent model.

4.3.3 PSA Ratio Model

Ratios of the DASG model updated for GC to the original DASG CNA model were calculated for all four DASG models and for a range of PSA frequencies, magnitude, and distances. These ratios are plotted in Figure 4.13 for various frequencies, for **M** = 4.0, 5.0, 6.0, 7.0, and 8.0, and for all four DASG models against R_{RUP}. There is very little difference in the ratio between the four DASG models, and there is no difference in the ratios with varying magnitudes. This lack of variation with magnitude is expected since the only adjustment to the DASG models for the GC predictions was on the linear distance attenuation term. For application, it is recommended that the average ratio across the four DASG models be used. This is plotted in Figure 4.13 in blue.

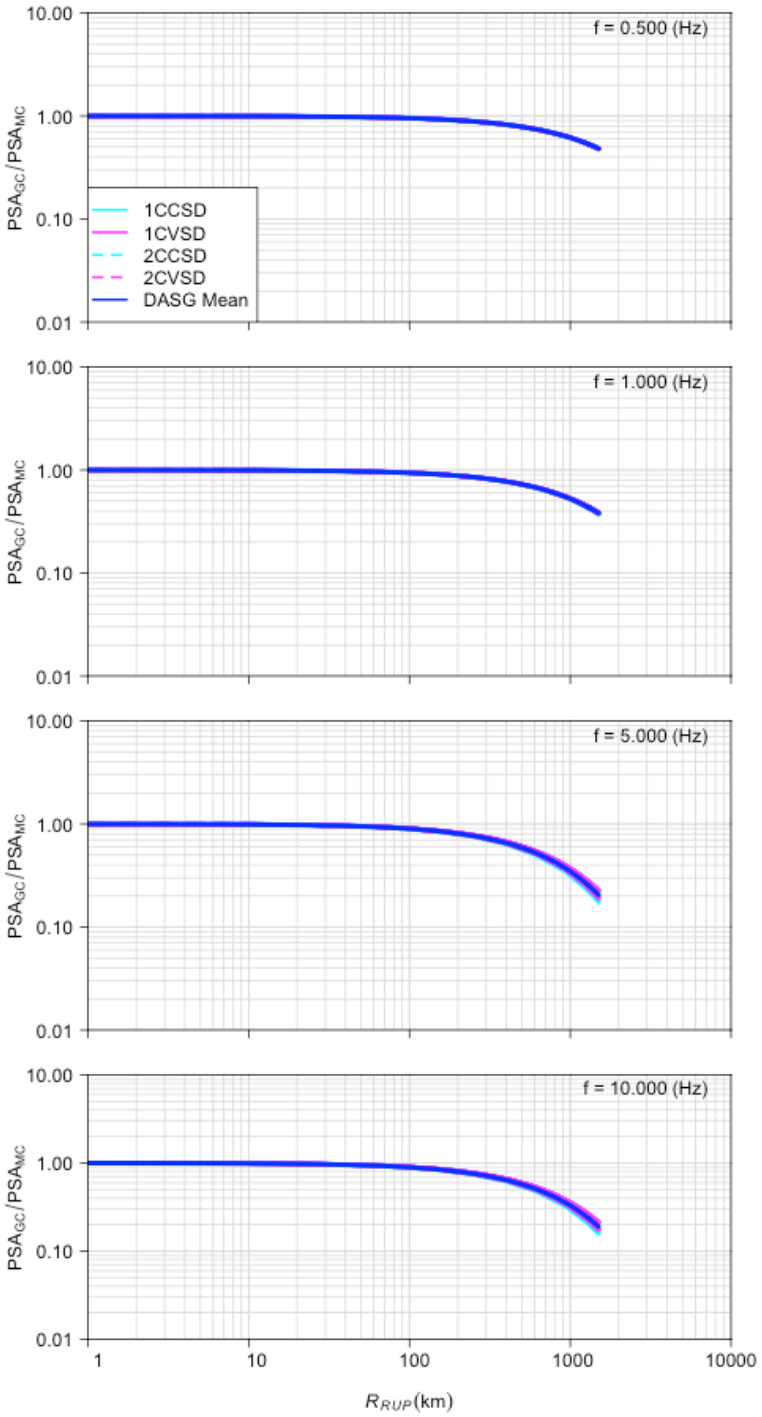

Figure 4.13 Gulf Coast adjustment ratios of the four DASG models along with the mean DASG ratios (solid blue) plotted against rupture distance for PSA at frequencies 0.5, 1.0, 5.0, and 10.0 Hz.

4.4 COMPARISON OF GULF COAST ADJUSTMENT MODELS

Figure 4.14 compares the PEER GC adjustment model with the DASG GC adjustment model. The two models show substantial differences, especially at low frequencies and large distances. At 0.5 Hz and 1000 km there is approximately a factor-of-five difference between the two adjustment models. This large difference in the models is partly a result of the difference in approach each group took in developing their adjustment models and partly due to the lack of quality data for Region 1 in the NGA-East Database. With this lack of data, a large range in median adjustments appears appropriate for application.

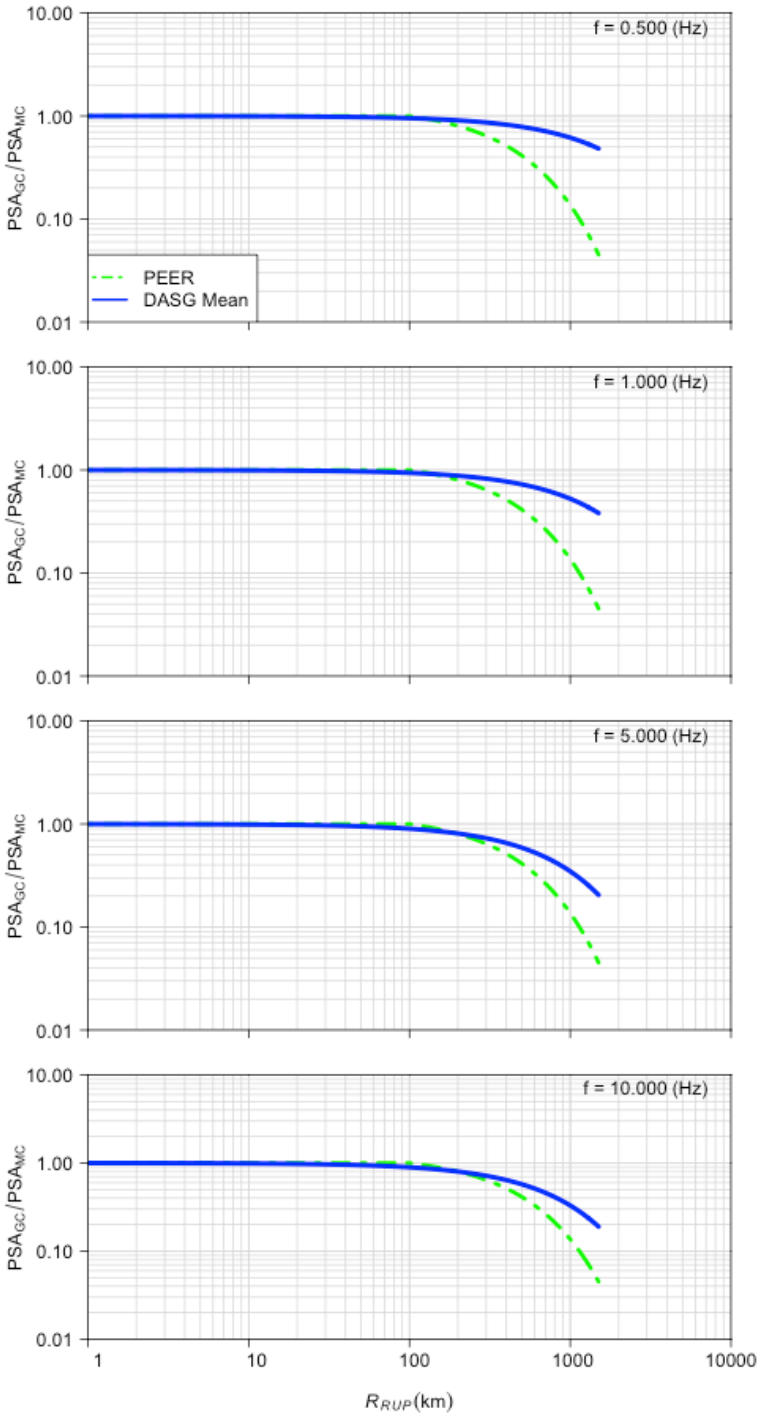

Figure 4.14 Comparison of Gulf Coast adjustment ratios between DASG model (blue) and the PEER model (green) plotted against distance for PSA at frequencies 0.5, 1.0, 5.0, and 10.0 Hz.

REFERENCES

Abrahamson N.A., Silva W.J, Kamai R. (2014). Summary of the ASK14 ground-motion relation for active crustal regions, *Earth. Spectra,* 30(3): 1025–1055.

Boatwright J., Seekins L. (2011). Regional spectral analysis of three moderate earthquakes in northeastern North America, *Bull. Seismol. Soc. Am.,* 101(4): 1769–1782.

Boore D.M. (1983). Stochastic simulation of high-frequency ground motions based on seismological models of the radiated spectra, *Bull. Seismol. Soc. Am*., 73: 1865–1894.

Boore D.M. (2003). Prediction of ground motion using the stochastic method, *Pure Appl. Geophys*. 160: 635–676.

Boore D.M. (2005). SMSIM—Fortran programs for simulating ground motions from earthquakes: Version 2.3—A revision of OFR 96-80-A, U.S. Geological Survey open-file report, *U. S. Geological Survey Open-File Report 00-509*, revised 15 August 2005, 55 pgs.

Boore D.M. (2010). Orientation-independent, non geometric-mean measures of seismic intensity from two horizontal components of motion, *Bull. Seismol. Soc. Am.,* 100: 1830–1835.

Boore D.M. (2012). Updated determination of stress parameters for nine well-recorded earthquakes in Eastern North America, *Seismol. Res. Lett.,* 83: 190–199.

Boore D.M., Campbell K.W., Atkinson G.M. (2010). Determination of stress parameters for eight well-recorded earthquakes in eastern North America, *Bull. Seismol. Soc. Am.,* 100: 1632–1645.

Boore D.M., Thompson E.M. (2015). Revisions to some parameters used in stochastic-method simulations of ground motion, *Bull. Seismol. Soc. Am.,* Vol. 105 (in press).

Bozorgnia Y., Abrahamson N.A., Al Atik L., Ancheta T.D., Atkinson G.M., Baker J., Baltay A., Boore D.M, Campbell K.W., Chiou B.-S.J., Darragh R.B., Day S., Donahue J., Graves R.W., Gregor N., Hanks T., Idriss I.M., Kamai R., Kishida T., Kottke A., Mahin S.A., Rezaeian S., Rowshandel B., Seyhan E., Shahi S., Shantz T., Silva W.J., Spudich P., Stewart J.P., Watson-Lamprey J., Wooddell K.E., Youngs R.R. (2014). NGA-West2 research project, *Earthq. Spectra*, 30(3): 973–987.

Campbell K.W., Bozorgnia Y. (2014). NGA-West2 ground motion model for the average horizontal components of PGA, PGV, and 5% damped linear acceleration response spectra, *Earthq. Spectra,* 30(3): 1087–1115.

Chiou B.S.-J., Youngs R.R. (2008). NGA model for average horizontal component of peak ground motion and response spectra, *PEER Report No. 2008/09*, Pacific Earthquake Engineering Research Center, University of California, Berkeley, CA.

Chiou B.-S.J., Youngs R.R. (2014). Update of the Chiou and Youngs NGA model for the average horizontal component of peak ground motion and response spectra, *Earthq. Spectra,* 30(3): 1117–1153.

Dreiling J., Isken M.P., Mooney W.D., Chapman M.C., Godbee R.W. (2014). *NGA-East* regionalization report: comparison of four crustal regions within central and eastern north america using waveform modeling and 5%-damped pseudo-spectral acceleration response, *PEER Report No. 2014/15*, Pacific Earthquake Engineering Research Center, University of California, Berkeley, CA.

EPRI (1993). Guidelines for determining design basis ground motions, *EPRI TR-102293*, Vol 1–5, Electric Power Research Institute, Palo Alto, CA.

EPRI (2004). CEUS ground motion project final report. *Technical Report 100968,*. Electric Power Research Institute, Dominion Energy, Glen Allen, VA, Entergy Nuclear, Jackson, MS, and Exelon Generation Company, Kennett Square, PA. Palo Alto, CA.

EPRI/DOE/NRC (2012). Technical Report: Central and Eastern United States Seismic Source Characterization for Nuclear Facilities, NUREG-2115.

Goulet C.A., Kishida T. Ancheta T D., Cramer C.H., Darragh R.B., Silva W.J., Hashash Y.M.A., Harmon J., Stewart J.P., Wooddell K.E., Youngs R.R. (2014). PEER NGA-East database, *PEER Report No. 2014/17,* Pacific Earthquake Engineering Research Center, University of California, Berkeley, CA.

Graves R.W., Pitarka A. (2015). Refinements to the Graves and Pitarka (2010) broadband ground motion simulation method, *Seismol. Res. Lett.*, 86(1): 75–80.

Hashash Y.M.A., Kottke A.R., Stewart J.P., Campbell K.W., Kim B., Rathje E.M., Silva W.J. (2014). Reference rock site condition for central and eastern North America, *Bull. Seismol. Soc. Am*., 104: 684–701.

PEER (2015). NGA-East: Median Ground-Motion Models for the Central and Eastern North America Region, *PEER Report No. 2015/04*, Pacific Earthquake Engineering Research Center, University of California, Berkeley, CA.

Power M., Chiou B.-S.J., Abrahamson N.A., Bozorgnia Y., Shantz T., Roblee C. (2008). An overview of the NGA project, *Earthq. Spectra*, 24: 3–21: 160–166.

Somerville P. (2014). Scaling relations between seismic moment and rupture area of earthquakes in stable continental regions, *PEER Report No. 2014/14*, Pacific Earthquake Engineering Research Center, University of California, Berkeley, CA.

Yenier E., Atkinson G.M. (2015). Regionally-adjustable generic ground-motion prediction equation based on equivalent point-source simulations: Application to Central and Eastern North America, *Bull. Seismol. Soc. Am.*, accepted for publication.

Electronic Appendix A

The adjusted median GMM tables are included as an electronic appendix to this report. There is one Excel workbook per GMM, with each worksheet corresponding to a specific GMIM. The tabulated data reflect all the adjustments described in Chapter 2.

A.1 Adjusted Model Output for B_A04

A.2 Adjusted Model Output for B_AB14

A.3 Adjusted Model Output for B_AB95

A.4 Adjusted Model Output for B_BCA10D

A.5 Adjusted Model Output for B_BS11

A.6 Adjusted Model Output for B_SGD02

A.7 Adjusted Model Output for DASG 1CVSP

A.8 Adjusted Model Output for DASG 1CCSP

A.9 Adjusted Model Output for DASG 1CVSP

A.10 Adjusted Model Output for DASG 2CCSP

A.11 Adjusted Model Output for YA15

A.12 Adjusted Model Output for PZCT_M1SS

A.13 Adjusted Model Output for PZCT_M2ES

A.14 Adjusted Model Output for Frankel

A.15 Adjusted Model Output for SP15

A.16 Model Output for ANC15 – no adjustment performed

A.17 Model Output for Graizer – only spectral shape adjustment performed

A.18 Adjusted Model Output for HA15

A.19 Adjusted Model Output for PEER_EX

A.20 Adjusted Model Output for PEER_GP

Electronic Appendix B

The two Gulf Coast adjustment models described in Chapter 4 are provided below in Excel workbooks.

B.1 PEER Gulf Coast Adjustment Model

B.2 DASG Mean Gulf Coast Adjustment Model

PEER REPORTS

PEER reports are available as a free PDF download from http://peer.berkeley.edu/publications/peer_reports_complete.html. Printed hard copies of PEER reports can be ordered directly from our printer by following the instructions at http://peer.berkeley.edu/publications/peer_reports.html. For other related questions about the PEER Report Series, contact the Pacific Earthquake Engineering Research Center, 325 Davis Hall mail code 1792, Berkeley, CA 94720. Tel.: (510) 642-3437; Fax: (510) 665-1655; Email: peer_editor@berkeley.edu

PEER 2015/08 *NGA-East: Adjustments to Median Ground-Motion Models for Central and Eastern North America.* August 2015.

PEER 2015/07 *NGA-East: Ground-Motion Standard-Deviation Models for Central and Eastern North America.* Linda Al Atik. June 2015.

PEER 2015/06 *Adjusting Ground-Motion Intensity Measures to a Reference Site for which V_{S30} = 3000 m/sec.* David M. Boore. May 2015.

PEER 2015/05 *Hybrid Simulation of Seismic Isolation Systems Applied to an APR-1400 Nuclear Power Plant.* Andreas H. Schellenberg, Alireza Sarebanha, Matthew J. Schoettler, Gilberto Mosqueda, Gianmario Benzoni, and Stephen A. Mahin. April 2015.

PEER 2015/04 *NGA-East: Median Ground-Motion Models for the Central and Eastern North America Region.* April 2015.

PEER 2015/03 *Single Series Solution for the Rectangular Fiber-Reinforced Elastomeric Isolator Compression Modulus.* James M. Kelly and Niel C. Van Engelen. March 2015.

PEER 2015/02 *A Full-Scale, Single-Column Bridge Bent Tested by Shake-Table Excitation.* Matthew J. Schoettler, José I. Restrepo, Gabriele Guerrini, David E. Duck, and Francesco Carrea. March 2015.

PEER 2015/01 *Concrete Column Blind Prediction Contest 2010: Outcomes and Observations.* Vesna Terzic, Matthew J. Schoettler, José I. Restrepo, and Stephen A Mahin. March 2015.

PEER 2014/20 *Stochastic Modeling and Simulation of Near-Fault Ground Motions for Performance-Based Earthquake Engineering.* Mayssa Dabaghi and Armen Der Kiureghian. December 2014.

PEER 2014/19 *Seismic Response of a Hybrid Fiber-Reinforced Concrete Bridge Column Detailed for Accelerated Bridge Construction*. Wilson Nguyen, William Trono, Marios Panagiotou, and Claudia P. Ostertag. December 2014.

PEER 2014/18 *Three-Dimensional Beam-Truss Model for Reinforced Concrete Walls and Slabs Subjected to Cyclic Static or Dynamic Loading.* Yuan Lu, Marios Panagiotou, and Ioannis Koutromanos. December 2014.

PEER 2014/17 *PEER NGA-East Database.* Christine A. Goulet, Tadahiro Kishida, Timothy D. Ancheta, Chris H. Cramer, Robert B. Darragh, Walter J. Silva, Youssef M.A. Hashash, Joseph Harmon, Jonathan P. Stewart, Katie E. Wooddell, and Robert R. Youngs. October 2014.

PEER 2014/16 *Guidelines for Performing Hazard-Consistent One-Dimensional Ground Response Analysis for Ground Motion Prediction.* Jonathan P. Stewart, Kioumars Afshari, and Youssef M.A. Hashash. October 2014.

PEER 2014/15 *NGA-East Regionalization Report: Comparison of Four Crustal Regions within Central and Eastern North America using Waveform Modeling and 5%-Damped Pseudo-Spectral Acceleration Response.* Jennifer Dreiling, Marius P. Isken, Walter D. Mooney, Martin C. Chapman, and Richard W. Godbee. October 2014.

PEER 2014/14 *Scaling Relations between Seismic Moment and Rupture Area of Earthquakes in Stable Continental Regions*. Paul Somerville. August 2014.

PEER 2014/13 *PEER Preliminary Notes and Observations on the August 24, 2014, South Napa Earthquake*. Grace S. Kang (Editor), Stephen A. Mahin (Editors). September 2014.

PEER 2014/12 *Reference-Rock Site Conditions for Central and Eastern North America: Part II – Attenuation (Kappa) Definition*. Kenneth W. Campbell, Youssef M.A. Hashash, Byungmin Kim, Albert R. Kottke, Ellen M. Rathje, Walter J. Silva, and Jonathan P. Stewart. August 2014.

PEER 2014/11 *Reference-Rock Site Conditions for Central and Eastern North America: Part I - Velocity Definition*. Youssef M.A. Hashash, Albert R. Kottke, Jonathan P. Stewart, Kenneth W. Campbell, Byungmin Kim, Ellen M. Rathje, Walter J. Silva, Sissy Nikolaou, and Cheryl Moss. August 2014.

PEER 2014/10 *Evaluation of Collapse and Non-Collapse of Parallel Bridges Affected by Liquefaction and Lateral Spreading*. Benjamin Turner, Scott J. Brandenberg, and Jonathan P. Stewart. August 2014.

PEER 2014/09 *PEER Arizona Strong-Motion Database and GMPEs Evaluation*. Tadahiro Kishida, Robert E. Kayen, Olga-Joan Ktenidou, Walter J. Silva, Robert B. Darragh, and Jennie Watson-Lamprey. June 2014.

PEER 2014/08 *Unbonded Pretensioned Bridge Columns with Rocking Detail*. Jeffrey A. Schaefer, Bryan Kennedy, Marc O. Eberhard, John F. Stanton. June 2014.

PEER 2014/07 *Northridge 20 Symposium Summary Report: Impacts, Outcomes, and Next Steps*. May 2014.

PEER 2014/06 *Report of the Tenth Planning Meeting of NEES/E-Defense Collaborative Research on Earthquake Engineering*. December 2013.

PEER 2014/05 *Seismic Velocity Site Characterization of Thirty-One Chilean Seismometer Stations by Spectral Analysis of Surface Wave Dispersion.* Robert Kayen, Brad D. Carkin, Skye Corbet, Camilo Pinilla, Allan Ng, Edward Gorbis, and Christine Truong. April 2014.

PEER 2014/04 *Effect of Vertical Acceleration on Shear Strength of Reinforced Concrete Columns.* Hyerin Lee and Khalid M. Mosalam. April 2014.

PEER 2014/03 *Retest of Thirty-Year-Old Neoprene Isolation Bearings.* James M. Kelly and Niel C. Van Engelen. March 2014.

PEER 2014/02 *Theoretical Development of Hybrid Simulation Applied to Plate Structures.* Ahmed A. Bakhaty, Khalid M. Mosalam, and Sanjay Govindjee. January 2014.

PEER 2014/01 *Performance-Based Seismic Assessment of Skewed Bridges.* Peyman Kaviani, Farzin Zareian, and Ertugrul Taciroglu. January 2014.

PEER 2013/26 *Urban Earthquake Engineering. Proceedings of the U.S.-Iran Seismic Workshop.* December 2013.

PEER 2013/25 *Earthquake Engineering for Resilient Communities: 2013 PEER Internship Program Research Report Collection.* Heidi Tremayne (Editor), Stephen A. Mahin (Editor), Jorge Archbold Monterossa, Matt Brosman, Shelly Dean, Katherine deLaveaga, Curtis Fong, Donovan Holder, Rakeeb Khan, Elizabeth Jachens, David Lam, Daniela Martinez Lopez, Mara Minner, Geffen Oren, Julia Pavicic, Melissa Quinonez, Lorena Rodriguez, Sean Salazar, Kelli Slaven, Vivian Steyert, Jenny Taing, and Salvador Tena. December 2013.

PEER 2013/24 *NGA-West2 Ground Motion Prediction Equations for Vertical Ground Motions.* September 2013.

PEER 2013/23 *Coordinated Planning and Preparedness for Fire Following Major Earthquakes.* Charles Scawthorn. November 2013.

PEER 2013/22 *GEM-PEER Task 3 Project: Selection of a Global Set of Ground Motion Prediction Equations.* Jonathan P. Stewart, John Douglas, Mohammad B. Javanbarg, Carola Di Alessandro, Yousef Bozorgnia, Norman A. Abrahamson, David M. Boore, Kenneth W. Campbell, Elise Delavaud, Mustafa Erdik and Peter J. Stafford. December 2013.

PEER 2013/21 *Seismic Design and Performance of Bridges with Columns on Rocking Foundations.* Grigorios Antonellis and Marios Panagiotou. September 2013.

PEER 2013/20 *Experimental and Analytical Studies on the Seismic Behavior of Conventional and Hybrid Braced Frames.* Jiun-Wei Lai and Stephen A. Mahin. September 2013.

PEER 2013/19 *Toward Resilient Communities: A Performance-Based Engineering Framework for Design and Evaluation of the Built Environment.* Michael William Mieler, Bozidar Stojadinovic, Robert J. Budnitz, Stephen A. Mahin and Mary C. Comerio. September 2013.

PEER 2013/18 *Identification of Site Parameters that Improve Predictions of Site Amplification.* Ellen M. Rathje and Sara Navidi. July 2013.

PEER 2013/17 *Response Spectrum Analysis of Concrete Gravity Dams Including Dam-Water-Foundation Interaction.* Arnkjell Løkke and Anil K. Chopra. July 2013.

PEER 2013/16 *Effect of hoop reinforcement spacing on the cyclic response of large reinforced concrete special moment frame beams.* Marios Panagiotou, Tea Visnjic, Grigorios Antonellis, Panagiotis Galanis, and Jack P. Moehle. June 2013.

PEER 2013/15 *A Probabilistic Framework to Include the Effects of Near-Fault Directivity in Seismic Hazard Assessment.* Shrey Kumar Shahi, Jack W. Baker. October 2013.

PEER 2013/14 *Hanging-Wall Scaling using Finite-Fault Simulations.* Jennifer L. Donahue and Norman A. Abrahamson. September 2013.

PEER 2013/13 *Semi-Empirical Nonlinear Site Amplification and its Application in NEHRP Site Factors.* Jonathan P. Stewart and Emel Seyhan. November 2013.

PEER 2013/12 *Nonlinear Horizontal Site Response for the NGA-West2 Project.* Ronnie Kamai, Norman A. Abramson, Walter J. Silva. May 2013.

PEER 2013/11 *Epistemic Uncertainty for NGA-West2 Models.* Linda Al Atik and Robert R. Youngs. May 2013.

PEER 2013/10 *NGA-West 2 Models for Ground-Motion Directionality.* Shrey K. Shahi and Jack W. Baker. May 2013.

PEER 2013/09 *Final Report of the NGA-West2 Directivity Working Group.* Paul Spudich, Jeffrey R. Bayless, Jack W. Baker, Brian S.J. Chiou, Badie Rowshandel, Shrey Shahi, and Paul Somerville. May 2013.

PEER 2013/08 *NGA-West2 Model for Estimating Average Horizontal Values of Pseudo-Absolute Spectral Accelerations Generated by Crustal Earthquakes.* I. M. Idriss. May 2013.

PEER 2013/07 *Update of the Chiou and Youngs NGA Ground Motion Model for Average Horizontal Component of Peak Ground Motion and Response Spectra.* Brian Chiou and Robert Youngs. May 2013.

PEER 2013/06 *NGA-West2 Campbell-Bozorgnia Ground Motion Model for the Horizontal Components of PGA, PGV, and 5%-Damped Elastic Pseudo-Acceleration Response Spectra for Periods Ranging from 0.01 to 10 sec.* Kenneth W. Campbell and Yousef Bozorgnia. May 2013.

PEER 2013/05 *NGA-West 2 Equations for Predicting Response Spectral Accelerations for Shallow Crustal Earthquakes.* David M. Boore, Jonathan P. Stewart, Emel Seyhan, Gail M. Atkinson. May 2013.

PEER 2013/04 *Update of the AS08 Ground-Motion Prediction Equations Based on the NGA-West2 Data Set.* Norman Abrahamson, Walter Silva, and Ronnie Kamai. May 2013.

PEER 2013/03 *PEER NGA-West2 Database.* Timothy D. Ancheta, Robert B. Darragh, Jonathan P. Stewart, Emel Seyhan, Walter J. Silva, Brian S.J. Chiou, Katie E. Wooddell, Robert W. Graves, Albert R. Kottke, David M. Boore, Tadahiro Kishida, and Jennifer L. Donahue. May 2013.

PEER 2013/02 *Hybrid Simulation of the Seismic Response of Squat Reinforced Concrete Shear Walls.* Catherine A. Whyte and Bozidar Stojadinovic. May 2013.

PEER 2013/01 *Housing Recovery in Chile: A Qualitative Mid-program Review.* Mary C. Comerio. February 2013.

PEER 2012/08 *Guidelines for Estimation of Shear Wave Velocity.* Bernard R. Wair, Jason T. DeJong, and Thomas Shantz. December 2012.

PEER 2012/07 *Earthquake Engineering for Resilient Communities: 2012 PEER Internship Program Research Report Collection.* Heidi Tremayne (Editor), Stephen A. Mahin (Editor), Collin Anderson, Dustin Cook, Michael Erceg, Carlos Esparza, Jose Jimenez, Dorian Krausz, Andrew Lo, Stephanie Lopez, Nicole McCurdy, Paul Shipman, Alexander Strum, Eduardo Vega. December 2012.

PEER 2012/06 *Fragilities for Precarious Rocks at Yucca Mountain.* Matthew D. Purvance, Rasool Anooshehpoor, and James N. Brune. December 2012.

PEER 2012/05 *Development of Simplified Analysis Procedure for Piles in Laterally Spreading Layered Soils.* Christopher R. McGann, Pedro Arduino, and Peter Mackenzie–Helnwein. December 2012.

PEER 2012/04 *Unbonded Pre-Tensioned Columns for Bridges in Seismic Regions.* Phillip M. Davis, Todd M. Janes, Marc O. Eberhard, and John F. Stanton. December 2012.

PEER 2012/03 *Experimental and Analytical Studies on Reinforced Concrete Buildings with Seismically Vulnerable Beam-Column Joints.* Sangjoon Park and Khalid M. Mosalam. October 2012.

PEER 2012/02 *Seismic Performance of Reinforced Concrete Bridges Allowed to Uplift during Multi-Directional Excitation.* Andres Oscar Espinoza and Stephen A. Mahin. July 2012.

PEER 2012/01 *Spectral Damping Scaling Factors for Shallow Crustal Earthquakes in Active Tectonic Regions.* Sanaz Rezaeian, Yousef Bozorgnia, I. M. Idriss, Kenneth Campbell, Norman Abrahamson, and Walter Silva. July 2012.

PEER 2011/10 *Earthquake Engineering for Resilient Communities: 2011 PEER Internship Program Research Report Collection.* Eds. Heidi Faison and Stephen A. Mahin. December 2011.

PEER 2011/09 *Calibration of Semi-Stochastic Procedure for Simulating High-Frequency Ground Motions.* Jonathan P. Stewart, Emel Seyhan, and Robert W. Graves. December 2011.

PEER 2011/08 *Water Supply in regard to Fire Following Earthquake.* Charles Scawthorn. November 2011.

PEER 2011/07 *Seismic Risk Management in Urban Areas. Proceedings of a U.S.-Iran-Turkey Seismic Workshop.* September 2011.

PEER 2011/06 *The Use of Base Isolation Systems to Achieve Complex Seismic Performance Objectives.* Troy A. Morgan and Stephen A. Mahin. July 2011.

PEER 2011/05 *Case Studies of the Seismic Performance of Tall Buildings Designed by Alternative Means.* Task 12 Report for the Tall Buildings Initiative. Jack Moehle, Yousef Bozorgnia, Nirmal Jayaram, Pierson Jones, Mohsen Rahnama, Nilesh Shome, Zeynep Tuna, John Wallace, Tony Yang, and Farzin Zareian. July 2011.

PEER 2011/04 *Recommended Design Practice for Pile Foundations in Laterally Spreading Ground.* Scott A. Ashford, Ross W. Boulanger, and Scott J. Brandenberg. June 2011.

PEER 2011/03 *New Ground Motion Selection Procedures and Selected Motions for the PEER Transportation Research Program.* Jack W. Baker, Ting Lin, Shrey K. Shahi, and Nirmal Jayaram. March 2011.

PEER 2011/02 *A Bayesian Network Methodology for Infrastructure Seismic Risk Assessment and Decision Support.* Michelle T. Bensi, Armen Der Kiureghian, and Daniel Straub. March 2011.

PEER 2011/01 *Demand Fragility Surfaces for Bridges in Liquefied and Laterally Spreading Ground.* Scott J. Brandenberg, Jian Zhang, Pirooz Kashighandi, Yili Huo, and Minxing Zhao. March 2011.

PEER 2010/05 *Guidelines for Performance-Based Seismic Design of Tall Buildings.* Developed by the Tall Buildings Initiative. November 2010.

PEER 2010/04 *Application Guide for the Design of Flexible and Rigid Bus Connections between Substation Equipment Subjected to Earthquakes.* Jean-Bernard Dastous and Armen Der Kiureghian. September 2010.

PEER 2010/03 *Shear Wave Velocity as a Statistical Function of Standard Penetration Test Resistance and Vertical Effective Stress at Caltrans Bridge Sites.* Scott J. Brandenberg, Naresh Bellana, and Thomas Shantz. June 2010.

PEER 2010/02 *Stochastic Modeling and Simulation of Ground Motions for Performance-Based Earthquake Engineering.* Sanaz Rezaeian and Armen Der Kiureghian. June 2010.

PEER 2010/01 *Structural Response and Cost Characterization of Bridge Construction Using Seismic Performance Enhancement Strategies.* Ady Aviram, Božidar Stojadinović, Gustavo J. Parra-Montesinos, and Kevin R. Mackie. March 2010.

PEER 2009/03 *The Integration of Experimental and Simulation Data in the Study of Reinforced Concrete Bridge Systems Including Soil-Foundation-Structure Interaction.* Matthew Dryden and Gregory L. Fenves. November 2009.

PEER 2009/02 *Improving Earthquake Mitigation through Innovations and Applications in Seismic Science, Engineering, Communication, and Response. Proceedings of a U.S.-Iran Seismic Workshop.* October 2009.

PEER 2009/01 *Evaluation of Ground Motion Selection and Modification Methods: Predicting Median Interstory Drift Response of Buildings.* Curt B. Haselton, Ed. June 2009.

PEER 2008/10 *Technical Manual for Strata.* Albert R. Kottke and Ellen M. Rathje. February 2009.

PEER 2008/09 *NGA Model for Average Horizontal Component of Peak Ground Motion and Response Spectra.* Brian S.-J. Chiou and Robert R. Youngs. November 2008.

PEER 2008/08 *Toward Earthquake-Resistant Design of Concentrically Braced Steel Structures.* Patxi Uriz and Stephen A. Mahin. November 2008.

PEER 2008/07 *Using OpenSees for Performance-Based Evaluation of Bridges on Liquefiable Soils.* Stephen L. Kramer, Pedro Arduino, and HyungSuk Shin. November 2008.

PEER 2008/06 *Shaking Table Tests and Numerical Investigation of Self-Centering Reinforced Concrete Bridge Columns.* Hyung IL Jeong, Junichi Sakai, and Stephen A. Mahin. September 2008.

PEER 2008/05 *Performance-Based Earthquake Engineering Design Evaluation Procedure for Bridge Foundations Undergoing Liquefaction-Induced Lateral Ground Displacement.* Christian A. Ledezma and Jonathan D. Bray. August 2008.

PEER 2008/04 *Benchmarking of Nonlinear Geotechnical Ground Response Analysis Procedures.* Jonathan P. Stewart, Annie On-Lei Kwok, Yousseff M. A. Hashash, Neven Matasovic, Robert Pyke, Zhiliang Wang, and Zhaohui Yang. August 2008.

PEER 2008/03 *Guidelines for Nonlinear Analysis of Bridge Structures in California.* Ady Aviram, Kevin R. Mackie, and Božidar Stojadinović. August 2008.

PEER 2008/02 *Treatment of Uncertainties in Seismic-Risk Analysis of Transportation Systems.* Evangelos Stergiou and Anne S. Kiremidjian. July 2008.

PEER 2008/01 *Seismic Performance Objectives for Tall Buildings.* William T. Holmes, Charles Kircher, William Petak, and Nabih Youssef. August 2008.

PEER 2007/12 *An Assessment to Benchmark the Seismic Performance of a Code-Conforming Reinforced Concrete Moment-Frame Building.* Curt Haselton, Christine A. Goulet, Judith Mitrani-Reiser, James L. Beck, Gregory G. Deierlein, Keith A. Porter, Jonathan P. Stewart, and Ertugrul Taciroglu. August 2008.

PEER 2007/11 *Bar Buckling in Reinforced Concrete Bridge Columns.* Wayne A. Brown, Dawn E. Lehman, and John F. Stanton. February 2008.

PEER 2007/10 *Computational Modeling of Progressive Collapse in Reinforced Concrete Frame Structures.* Mohamed M. Talaat and Khalid M. Mosalam. May 2008.

PEER 2007/09 *Integrated Probabilistic Performance-Based Evaluation of Benchmark Reinforced Concrete Bridges.* Kevin R. Mackie, John-Michael Wong, and Božidar Stojadinović. January 2008.

PEER 2007/08 *Assessing Seismic Collapse Safety of Modern Reinforced Concrete Moment-Frame Buildings.* Curt B. Haselton and Gregory G. Deierlein. February 2008.

PEER 2007/07 *Performance Modeling Strategies for Modern Reinforced Concrete Bridge Columns.* Michael P. Berry and Marc O. Eberhard. April 2008.

PEER 2007/06 *Development of Improved Procedures for Seismic Design of Buried and Partially Buried Structures.* Linda Al Atik and Nicholas Sitar. June 2007.

PEER 2007/05 *Uncertainty and Correlation in Seismic Risk Assessment of Transportation Systems.* Renee G. Lee and Anne S. Kiremidjian. July 2007.

PEER 2007/04 *Numerical Models for Analysis and Performance-Based Design of Shallow Foundations Subjected to Seismic Loading.* Sivapalan Gajan, Tara C. Hutchinson, Bruce L. Kutter, Prishati Raychowdhury, José A. Ugalde, and Jonathan P. Stewart. May 2008.

PEER 2007/03 *Beam-Column Element Model Calibrated for Predicting Flexural Response Leading to Global Collapse of RC Frame Buildings.* Curt B. Haselton, Abbie B. Liel, Sarah Taylor Lange, and Gregory G. Deierlein. May 2008.

PEER 2007/02 *Campbell-Bozorgnia NGA Ground Motion Relations for the Geometric Mean Horizontal Component of Peak and Spectral Ground Motion Parameters.* Kenneth W. Campbell and Yousef Bozorgnia. May 2007.

PEER 2007/01 *Boore-Atkinson NGA Ground Motion Relations for the Geometric Mean Horizontal Component of Peak and Spectral Ground Motion Parameters.* David M. Boore and Gail M. Atkinson. May. May 2007.

PEER 2006/12 *Societal Implications of Performance-Based Earthquake Engineering.* Peter J. May. May 2007.

PEER 2006/11 *Probabilistic Seismic Demand Analysis Using Advanced Ground Motion Intensity Measures, Attenuation Relationships, and Near-Fault Effects.* Polsak Tothong and C. Allin Cornell. March 2007.

PEER 2006/10 *Application of the PEER PBEE Methodology to the I-880 Viaduct.* Sashi Kunnath. February 2007.

PEER 2006/09 *Quantifying Economic Losses from Travel Forgone Following a Large Metropolitan Earthquake.* James Moore, Sungbin Cho, Yue Yue Fan, and Stuart Werner. November 2006.

PEER 2006/08 *Vector-Valued Ground Motion Intensity Measures for Probabilistic Seismic Demand Analysis*. Jack W. Baker and C. Allin Cornell. October 2006.

PEER 2006/07 *Analytical Modeling of Reinforced Concrete Walls for Predicting Flexural and Coupled–Shear-Flexural Responses*. Kutay Orakcal, Leonardo M. Massone, and John W. Wallace. October 2006.

PEER 2006/06 *Nonlinear Analysis of a Soil-Drilled Pier System under Static and Dynamic Axial Loading.* Gang Wang and Nicholas Sitar. November 2006.

PEER 2006/05 *Advanced Seismic Assessment Guidelines.* Paolo Bazzurro, C. Allin Cornell, Charles Menun, Maziar Motahari, and Nicolas Luco. September 2006.

PEER 2006/04 *Probabilistic Seismic Evaluation of Reinforced Concrete Structural Components and Systems.* Tae Hyung Lee and Khalid M. Mosalam. August 2006.

PEER 2006/03 *Performance of Lifelines Subjected to Lateral Spreading.* Scott A. Ashford and Teerawut Juirnarongrit. July 2006.

PEER 2006/02 *Pacific Earthquake Engineering Research Center Highway Demonstration Project.* Anne Kiremidjian, James Moore, Yue Yue Fan, Nesrin Basoz, Ozgur Yazali, and Meredith Williams. April 2006.

PEER 2006/01 *Bracing Berkeley. A Guide to Seismic Safety on the UC Berkeley Campus.* Mary C. Comerio, Stephen Tobriner, and Ariane Fehrenkamp. January 2006.

PEER 2005/16 *Seismic Response and Reliability of Electrical Substation Equipment and Systems.* Junho Song, Armen Der Kiureghian, and Jerome L. Sackman. April 2006.

PEER 2005/15 *CPT-Based Probabilistic Assessment of Seismic Soil Liquefaction Initiation.* R. E. S. Moss, R. B. Seed, R. E. Kayen, J. P. Stewart, and A. Der Kiureghian. April 2006.

PEER 2005/14 *Workshop on Modeling of Nonlinear Cyclic Load-Deformation Behavior of Shallow Foundations.* Bruce L. Kutter, Geoffrey Martin, Tara Hutchinson, Chad Harden, Sivapalan Gajan, and Justin Phalen. March 2006.

PEER 2005/13 *Stochastic Characterization and Decision Bases under Time-Dependent Aftershock Risk in Performance-Based Earthquake Engineering.* Gee Liek Yeo and C. Allin Cornell. July 2005.

PEER 2005/12 *PEER Testbed Study on a Laboratory Building: Exercising Seismic Performance Assessment.* Mary C. Comerio, editor. November 2005.

PEER 2005/11 *Van Nuys Hotel Building Testbed Report: Exercising Seismic Performance Assessment.* Helmut Krawinkler, editor. October 2005.

PEER 2005/10 *First NEES/E-Defense Workshop on Collapse Simulation of Reinforced Concrete Building Structures.* September 2005.

PEER 2005/09 *Test Applications of Advanced Seismic Assessment Guidelines.* Joe Maffei, Karl Telleen, Danya Mohr, William Holmes, and Yuki Nakayama. August 2006.

PEER 2005/08 *Damage Accumulation in Lightly Confined Reinforced Concrete Bridge Columns.* R. Tyler Ranf, Jared M. Nelson, Zach Price, Marc O. Eberhard, and John F. Stanton. April 2006.

PEER 2005/07 *Experimental and Analytical Studies on the Seismic Response of Freestanding and Anchored Laboratory Equipment.* Dimitrios Konstantinidis and Nicos Makris. January 2005.

PEER 2005/06 *Global Collapse of Frame Structures under Seismic Excitations*. Luis F. Ibarra and Helmut Krawinkler. September 2005.

PEER 2005//05 *Performance Characterization of Bench- and Shelf-Mounted Equipment.* Samit Ray Chaudhuri and Tara C. Hutchinson. May 2006.

PEER 2005/04 *Numerical Modeling of the Nonlinear Cyclic Response of Shallow Foundations.* Chad Harden, Tara Hutchinson, Geoffrey R. Martin, and Bruce L. Kutter. August 2005.

PEER 2005/03 *A Taxonomy of Building Components for Performance-Based Earthquake Engineering.* Keith A. Porter. September 2005.

PEER 2005/02 *Fragility Basis for California Highway Overpass Bridge Seismic Decision Making*. Kevin R. Mackie and Božidar Stojadinović. June 2005.

PEER 2005/01 *Empirical Characterization of Site Conditions on Strong Ground Motion.* Jonathan P. Stewart, Yoojoong Choi, and Robert W. Graves. June 2005.

PEER 2004/09 *Electrical Substation Equipment Interaction: Experimental Rigid Conductor Studies.* Christopher Stearns and André Filiatrault. February 2005.

PEER 2004/08 *Seismic Qualification and Fragility Testing of Line Break 550-kV Disconnect Switches.* Shakhzod M. Takhirov, Gregory L. Fenves, and Eric Fujisaki. January 2005.

PEER 2004/07 *Ground Motions for Earthquake Simulator Qualification of Electrical Substation Equipment.* Shakhzod M. Takhirov, Gregory L. Fenves, Eric Fujisaki, and Don Clyde. January 2005.

PEER 2004/06 *Performance-Based Regulation and Regulatory Regimes.* Peter J. May and Chris Koski. September 2004.

PEER 2004/05 *Performance-Based Seismic Design Concepts and Implementation: Proceedings of an International Workshop.* Peter Fajfar and Helmut Krawinkler, editors. September 2004.

PEER 2004/04 *Seismic Performance of an Instrumented Tilt-up Wall Building.* James C. Anderson and Vitelmo V. Bertero. July 2004.

PEER 2004/03 *Evaluation and Application of Concrete Tilt-up Assessment Methodologies.* Timothy Graf and James O. Malley. October 2004.

PEER 2004/02 *Analytical Investigations of New Methods for Reducing Residual Displacements of Reinforced Concrete Bridge Columns.* Junichi Sakai and Stephen A. Mahin. August 2004.

PEER 2004/01 *Seismic Performance of Masonry Buildings and Design Implications.* Kerri Anne Taeko Tokoro, James C. Anderson, and Vitelmo V. Bertero. February 2004.

PEER 2003/18 *Performance Models for Flexural Damage in Reinforced Concrete Columns.* Michael Berry and Marc Eberhard. August 2003.

PEER 2003/17 *Predicting Earthquake Damage in Older Reinforced Concrete Beam-Column Joints.* Catherine Pagni and Laura Lowes. October 2004.

PEER 2003/16 *Seismic Demands for Performance-Based Design of Bridges.* Kevin Mackie and Božidar Stojadinović. August 2003.

PEER 2003/15 *Seismic Demands for Nondeteriorating Frame Structures and Their Dependence on Ground Motions.* Ricardo Antonio Medina and Helmut Krawinkler. May 2004.

PEER 2003/14 *Finite Element Reliability and Sensitivity Methods for Performance-Based Earthquake Engineering.* Terje Haukaas and Armen Der Kiureghian. April 2004.

PEER 2003/13 *Effects of Connection Hysteretic Degradation on the Seismic Behavior of Steel Moment-Resisting Frames.* Janise E. Rodgers and Stephen A. Mahin. March 2004.

PEER 2003/12 *Implementation Manual for the Seismic Protection of Laboratory Contents: Format and Case Studies.* William T. Holmes and Mary C. Comerio. October 2003.

PEER 2003/11 *Fifth U.S.-Japan Workshop on Performance-Based Earthquake Engineering Methodology for Reinforced Concrete Building Structures.* February 2004.

PEER 2003/10 *A Beam-Column Joint Model for Simulating the Earthquake Response of Reinforced Concrete Frames.* Laura N. Lowes, Nilanjan Mitra, and Arash Altoontash. February 2004.

PEER 2003/09 *Sequencing Repairs after an Earthquake: An Economic Approach.* Marco Casari and Simon J. Wilkie. April 2004.

PEER 2003/08 *A Technical Framework for Probability-Based Demand and Capacity Factor Design (DCFD) Seismic Formats*. Fatemeh Jalayer and C. Allin Cornell. November 2003.

PEER 2003/07 *Uncertainty Specification and Propagation for Loss Estimation Using FOSM Methods.* Jack W. Baker and C. Allin Cornell. September 2003.

PEER 2003/06 *Performance of Circular Reinforced Concrete Bridge Columns under Bidirectional Earthquake Loading*. Mahmoud M. Hachem, Stephen A. Mahin, and Jack P. Moehle. February 2003.

PEER 2003/05 *Response Assessment for Building-Specific Loss Estimation.* Eduardo Miranda and Shahram Taghavi. September 2003.

PEER 2003/04 *Experimental Assessment of Columns with Short Lap Splices Subjected to Cyclic Loads*. Murat Melek, John W. Wallace, and Joel Conte. April 2003.

PEER 2003/03 *Probabilistic Response Assessment for Building-Specific Loss Estimation.* Eduardo Miranda and Hesameddin Aslani. September 2003.

PEER 2003/02 *Software Framework for Collaborative Development of Nonlinear Dynamic Analysis Program.* Jun Peng and Kincho H. Law. September 2003.

PEER 2003/01 *Shake Table Tests and Analytical Studies on the Gravity Load Collapse of Reinforced Concrete Frames.* Kenneth John Elwood and Jack P. Moehle. November 2003.

PEER 2002/24 *Performance of Beam to Column Bridge Joints Subjected to a Large Velocity Pulse.* Natalie Gibson, André Filiatrault, and Scott A. Ashford. April 2002.

PEER 2002/23 *Effects of Large Velocity Pulses on Reinforced Concrete Bridge Columns.* Greg L. Orozco and Scott A. Ashford. April 2002.

PEER 2002/22 *Characterization of Large Velocity Pulses for Laboratory Testing.* Kenneth E. Cox and Scott A. Ashford. April 2002.

PEER 2002/21 *Fourth U.S.-Japan Workshop on Performance-Based Earthquake Engineering Methodology for Reinforced Concrete Building Structures*. December 2002.

PEER 2002/20 *Barriers to Adoption and Implementation of PBEE Innovations.* Peter J. May. August 2002.

PEER 2002/19 *Economic-Engineered Integrated Models for Earthquakes: Socioeconomic Impacts.* Peter Gordon, James E. Moore II, and Harry W. Richardson. July 2002.

PEER 2002/18 *Assessment of Reinforced Concrete Building Exterior Joints with Substandard Details.* Chris P. Pantelides, Jon Hansen, Justin Nadauld, and Lawrence D. Reaveley. May 2002.

PEER 2002/17 *Structural Characterization and Seismic Response Analysis of a Highway Overcrossing Equipped with Elastomeric Bearings and Fluid Dampers: A Case Study.* Nicos Makris and Jian Zhang. November 2002.

PEER 2002/16 *Estimation of Uncertainty in Geotechnical Properties for Performance-Based Earthquake Engineering.* Allen L. Jones, Steven L. Kramer, and Pedro Arduino. December 2002.

PEER 2002/15 *Seismic Behavior of Bridge Columns Subjected to Various Loading Patterns.* Asadollah Esmaeily-Gh. and Yan Xiao. December 2002.

PEER 2002/14 *Inelastic Seismic Response of Extended Pile Shaft Supported Bridge Structures.* T.C. Hutchinson, R.W. Boulanger, Y.H. Chai, and I.M. Idriss. December 2002.

PEER 2002/13 *Probabilistic Models and Fragility Estimates for Bridge Components and Systems.* Paolo Gardoni, Armen Der Kiureghian, and Khalid M. Mosalam. June 2002.

PEER 2002/12 *Effects of Fault Dip and Slip Rake on Near-Source Ground Motions: Why Chi-Chi Was a Relatively Mild M7.6 Earthquake.* Brad T. Aagaard, John F. Hall, and Thomas H. Heaton. December 2002.

PEER 2002/11 *Analytical and Experimental Study of Fiber-Reinforced Strip Isolators*. James M. Kelly and Shakhzod M. Takhirov. September 2002.

PEER 2002/10 *Centrifuge Modeling of Settlement and Lateral Spreading with Comparisons to Numerical Analyses***.** Sivapalan Gajan and Bruce L. Kutter. January 2003.

PEER 2002/09 *Documentation and Analysis of Field Case Histories of Seismic Compression during the 1994 Northridge, California, Earthquake*. Jonathan P. Stewart, Patrick M. Smith, Daniel H. Whang, and Jonathan D. Bray. October 2002.

PEER 2002/08 *Component Testing, Stability Analysis and Characterization of Buckling-Restrained Unbonded Braces™*. Cameron Black, Nicos Makris, and Ian Aiken. September 2002.

PEER 2002/07 *Seismic Performance of Pile-Wharf Connections.* Charles W. Roeder, Robert Graff, Jennifer Soderstrom, and Jun Han Yoo. December 2001.

PEER 2002/06 *The Use of Benefit-Cost Analysis for Evaluation of Performance-Based Earthquake Engineering Decisions*. Richard O. Zerbe and Anthony Falit-Baiamonte. September 2001.

PEER 2002/05 *Guidelines, Specifications, and Seismic Performance Characterization of Nonstructural Building Components and Equipment*. André Filiatrault, Constantin Christopoulos, and Christopher Stearns. September 2001.

PEER 2002/04 *Consortium of Organizations for Strong-Motion Observation Systems and the Pacific Earthquake Engineering Research Center Lifelines Program: Invited Workshop on Archiving and Web Dissemination of Geotechnical Data, 4–5 October 2001*. September 2002.

PEER 2002/03 *Investigation of Sensitivity of Building Loss Estimates to Major Uncertain Variables for the Van Nuys Testbed.* Keith A. Porter, James L. Beck, and Rustem V. Shaikhutdinov. August 2002.

PEER 2002/02 *The Third U.S.-Japan Workshop on Performance-Based Earthquake Engineering Methodology for Reinforced Concrete Building Structures*. July 2002.

PEER 2002/01 *Nonstructural Loss Estimation: The UC Berkeley Case Study.* Mary C. Comerio and John C. Stallmeyer. December 2001.

PEER 2001/16 *Statistics of SDF-System Estimate of Roof Displacement for Pushover Analysis of Buildings.* Anil K. Chopra, Rakesh K. Goel, and Chatpan Chintanapakdee. December 2001.

PEER 2001/15 *Damage to Bridges during the 2001 Nisqually Earthquake.* R. Tyler Ranf, Marc O. Eberhard, and Michael P. Berry. November 2001.

PEER 2001/14 *Rocking Response of Equipment Anchored to a Base Foundation.* Nicos Makris and Cameron J. Black. September 2001.

PEER 2001/13 *Modeling Soil Liquefaction Hazards for Performance-Based Earthquake Engineering.* Steven L. Kramer and Ahmed-W. Elgamal. February 2001.

PEER 2001/12 *Development of Geotechnical Capabilities in OpenSees.* Boris Jeremić. September 2001.

PEER 2001/11 *Analytical and Experimental Study of Fiber-Reinforced Elastomeric Isolators*. James M. Kelly and Shakhzod M. Takhirov. September 2001.

PEER 2001/10 *Amplification Factors for Spectral Acceleration in Active Regions.* Jonathan P. Stewart, Andrew H. Liu, Yoojoong Choi, and Mehmet B. Baturay. December 2001.

PEER 2001/09 *Ground Motion Evaluation Procedures for Performance-Based Design.* Jonathan P. Stewart, Shyh-Jeng Chiou, Jonathan D. Bray, Robert W. Graves, Paul G. Somerville, and Norman A. Abrahamson. September 2001.

PEER 2001/08 *Experimental and Computational Evaluation of Reinforced Concrete Bridge Beam-Column Connections for Seismic Performance*. Clay J. Naito, Jack P. Moehle, and Khalid M. Mosalam. November 2001.

PEER 2001/07 *The Rocking Spectrum and the Shortcomings of Design Guidelines.* Nicos Makris and Dimitrios Konstantinidis. August 2001.

PEER 2001/06 *Development of an Electrical Substation Equipment Performance Database for Evaluation of Equipment Fragilities*. Thalia Agnanos. April 1999.

PEER 2001/05 *Stiffness Analysis of Fiber-Reinforced Elastomeric Isolators.* Hsiang-Chuan Tsai and James M. Kelly. May 2001.

PEER 2001/04 *Organizational and Societal Considerations for Performance-Based Earthquake Engineering.* Peter J. May. April 2001.

PEER 2001/03 *A Modal Pushover Analysis Procedure to Estimate Seismic Demands for Buildings: Theory and Preliminary Evaluation.* Anil K. Chopra and Rakesh K. Goel. January 2001.

PEER 2001/02 *Seismic Response Analysis of Highway Overcrossings Including Soil-Structure Interaction.* Jian Zhang and Nicos Makris. March 2001.

PEER 2001/01 *Experimental Study of Large Seismic Steel Beam-to-Column Connections.* Egor P. Popov and Shakhzod M. Takhirov. November 2000.

PEER 2000/10 *The Second U.S.-Japan Workshop on Performance-Based Earthquake Engineering Methodology for Reinforced Concrete Building Structures.* March 2000.

PEER 2000/09 *Structural Engineering Reconnaissance of the August 17, 1999 Earthquake: Kocaeli (Izmit), Turkey.* Halil Sezen, Kenneth J. Elwood, Andrew S. Whittaker, Khalid Mosalam, John J. Wallace, and John F. Stanton. December 2000.

PEER 2000/08 *Behavior of Reinforced Concrete Bridge Columns Having Varying Aspect Ratios and Varying Lengths of Confinement.* Anthony J. Calderone, Dawn E. Lehman, and Jack P. Moehle. January 2001.

PEER 2000/07 *Cover-Plate and Flange-Plate Reinforced Steel Moment-Resisting Connections.* Taejin Kim, Andrew S. Whittaker, Amir S. Gilani, Vitelmo V. Bertero, and Shakhzod M. Takhirov. September 2000.

PEER 2000/06 *Seismic Evaluation and Analysis of 230-kV Disconnect Switches.* Amir S. J. Gilani, Andrew S. Whittaker, Gregory L. Fenves, Chun-Hao Chen, Henry Ho, and Eric Fujisaki. July 2000.

PEER 2000/05 *Performance-Based Evaluation of Exterior Reinforced Concrete Building Joints for Seismic Excitation.* Chandra Clyde, Chris P. Pantelides, and Lawrence D. Reaveley. July 2000.

PEER 2000/04 *An Evaluation of Seismic Energy Demand: An Attenuation Approach.* Chung-Che Chou and Chia-Ming Uang. July 1999.

PEER 2000/03 *Framing Earthquake Retrofitting Decisions: The Case of Hillside Homes in Los Angeles.* Detlof von Winterfeldt, Nels Roselund, and Alicia Kitsuse. March 2000.

PEER 2000/02 *U.S.-Japan Workshop on the Effects of Near-Field Earthquake Shaking.* Andrew Whittaker, ed. July 2000.

PEER 2000/01 *Further Studies on Seismic Interaction in Interconnected Electrical Substation Equipment.* Armen Der Kiureghian, Kee-Jeung Hong, and Jerome L. Sackman. November 1999.

PEER 1999/14 *Seismic Evaluation and Retrofit of 230-kV Porcelain Transformer Bushings*. Amir S. Gilani, Andrew S. Whittaker, Gregory L. Fenves, and Eric Fujisaki. December 1999.

PEER 1999/13 *Building Vulnerability Studies: Modeling and Evaluation of Tilt-up and Steel Reinforced Concrete Buildings.* John W. Wallace, Jonathan P. Stewart, and Andrew S. Whittaker, editors. December 1999.

PEER 1999/12 *Rehabilitation of Nonductile RC Frame Building Using Encasement Plates and Energy-Dissipating Devices.* Mehrdad Sasani, Vitelmo V. Bertero, James C. Anderson. December 1999.

PEER 1999/11 *Performance Evaluation Database for Concrete Bridge Components and Systems under Simulated Seismic Loads.* Yael D. Hose and Frieder Seible. November 1999.

PEER 1999/10 *U.S.-Japan Workshop on Performance-Based Earthquake Engineering Methodology for Reinforced Concrete Building Structures.* December 1999.

PEER 1999/09 *Performance Improvement of Long Period Building Structures Subjected to Severe Pulse-Type Ground Motions*. James C. Anderson, Vitelmo V. Bertero, and Raul Bertero. October 1999.

PEER 1999/08 *Envelopes for Seismic Response Vectors.* Charles Menun and Armen Der Kiureghian. July 1999.

PEER 1999/07 *Documentation of Strengths and Weaknesses of Current Computer Analysis Methods for Seismic Performance of Reinforced Concrete Members.* William F. Cofer. November 1999.

PEER 1999/06 *Rocking Response and Overturning of Anchored Equipment under Seismic Excitations.* Nicos Makris and Jian Zhang. November 1999.

PEER 1999/05 *Seismic Evaluation of 550 kV Porcelain Transformer Bushings.* Amir S. Gilani, Andrew S. Whittaker, Gregory L. Fenves, and Eric Fujisaki. October 1999.

PEER 1999/04 *Adoption and Enforcement of Earthquake Risk-Reduction Measures.* Peter J. May, Raymond J. Burby, T. Jens Feeley, and Robert Wood.

PEER 1999/03 *Task 3 Characterization of Site Response General Site Categories*. Adrian Rodriguez-Marek, Jonathan D. Bray, and Norman Abrahamson. February 1999.

PEER 1999/02 *Capacity-Demand-Diagram Methods for Estimating Seismic Deformation of Inelastic Structures: SDF Systems*. Anil K. Chopra and Rakesh Goel. April 1999.

PEER 1999/01 *Interaction in Interconnected Electrical Substation Equipment Subjected to Earthquake Ground Motions.* Armen Der Kiureghian, Jerome L. Sackman, and Kee-Jeung Hong. February 1999.

PEER 1998/08 *Behavior and Failure Analysis of a Multiple-Frame Highway Bridge in the 1994 Northridge Earthquake.* Gregory L. Fenves and Michael Ellery. December 1998.

PEER 1998/07 *Empirical Evaluation of Inertial Soil-Structure Interaction Effects.* Jonathan P. Stewart, Raymond B. Seed, and Gregory L. Fenves. November 1998.

PEER 1998/06 *Effect of Damping Mechanisms on the Response of Seismic Isolated Structures.* Nicos Makris and Shih-Po Chang. November 1998.

PEER 1998/05 *Rocking Response and Overturning of Equipment under Horizontal Pulse-Type Motions.* Nicos Makris and Yiannis Roussos. October 1998.

PEER 1998/04 *Pacific Earthquake Engineering Research Invitational Workshop Proceedings, May 14–15, 1998: Defining the Links between Planning, Policy Analysis, Economics and Earthquake Engineering.* Mary Comerio and Peter Gordon. September 1998.

PEER 1998/03 *Repair/Upgrade Procedures for Welded Beam to Column Connections.* James C. Anderson and Xiaojing Duan. May 1998.

PEER 1998/02 *Seismic Evaluation of 196 kV Porcelain Transformer Bushings.* Amir S. Gilani, Juan W. Chavez, Gregory L. Fenves, and Andrew S. Whittaker. May 1998.

PEER 1998/01 *Seismic Performance of Well-Confined Concrete Bridge Columns.* Dawn E. Lehman and Jack P. Moehle. December 2000.

ONLINE PEER REPORTS

The following PEER reports are available by Internet only at http://peer.berkeley.edu/publications/peer_reports_complete.html.

PEER 2012/103 *Performance-Based Seismic Demand Assessment of Concentrically Braced Steel Frame Buildings.* Chui-Hsin Chen and Stephen A. Mahin. December 2012.

PEER 2012/102 *Procedure to Restart an Interrupted Hybrid Simulation: Addendum to PEER Report 2010/103.* Vesna Terzic and Bozidar Stojadinovic. October 2012.

PEER 2012/101 *Mechanics of Fiber Reinforced Bearings.* James M. Kelly and Andrea Calabrese. February 2012.

PEER 2011/107 *Nonlinear Site Response and Seismic Compression at Vertical Array Strongly Shaken by 2007 Niigata-ken Chuetsu-oki Earthquake.* Eric Yee, Jonathan P. Stewart, and Kohji Tokimatsu. December 2011.

PEER 2011/106 *Self Compacting Hybrid Fiber Reinforced Concrete Composites for Bridge Columns.* Pardeep Kumar, Gabriel Jen, William Trono, Marios Panagiotou, and Claudia Ostertag. September 2011.

PEER 2011/105 *Stochastic Dynamic Analysis of Bridges Subjected to Spacially Varying Ground Motions.* Katerina Konakli and Armen Der Kiureghian. August 2011.

PEER 2011/104 *Design and Instrumentation of the 2010 E-Defense Four-Story Reinforced Concrete and Post-Tensioned Concrete Buildings.* Takuya Nagae, Kenichi Tahara, Taizo Matsumori, Hitoshi Shiohara, Toshimi Kabeyasawa, Susumu Kono, Minehiro Nishiyama (Japanese Research Team) and John Wallace, Wassim Ghannoum, Jack Moehle, Richard Sause, Wesley Keller, Zeynep Tuna (U.S. Research Team). June 2011.

PEER 2011/103 *In-Situ Monitoring of the Force Output of Fluid Dampers: Experimental Investigation.* Dimitrios Konstantinidis, James M. Kelly, and Nicos Makris. April 2011.

PEER 2011/102 *Ground-motion prediction equations 1964 - 2010.* John Douglas. April 2011.

PEER 2011/101 *Report of the Eighth Planning Meeting of NEES/E-Defense Collaborative Research on Earthquake Engineering.* Convened by the Hyogo Earthquake Engineering Research Center (NIED), NEES Consortium, Inc. February 2011.

PEER 2010/111 *Modeling and Acceptance Criteria for Seismic Design and Analysis of Tall Buildings.* Task 7 Report for the Tall Buildings Initiative - Published jointly by the Applied Technology Council. October 2010.

PEER 2010/110 *Seismic Performance Assessment and Probabilistic Repair Cost Analysis of Precast Concrete Cladding Systems for Multistory Buildlings.* Jeffrey P. Hunt and Božidar Stojadinovic. November 2010.

PEER 2010/109 *Report of the Seventh Joint Planning Meeting of NEES/E-Defense Collaboration on Earthquake Engineering. Held at the E-Defense, Miki, and Shin-Kobe, Japan, September 18–19, 2009.* August 2010.

PEER 2010/108 *Probabilistic Tsunami Hazard in California.* Hong Kie Thio, Paul Somerville, and Jascha Polet, preparers. October 2010.

PEER 2010/107 *Performance and Reliability of Exposed Column Base Plate Connections for Steel Moment-Resisting Frames.* Ady Aviram, Božidar Stojadinovic, and Armen Der Kiureghian. August 2010.

PEER 2010/106 *Verification of Probabilistic Seismic Hazard Analysis Computer Programs.* Patricia Thomas, Ivan Wong, and Norman Abrahamson. May 2010.

PEER 2010/105 *Structural Engineering Reconnaissance of the April 6, 2009, Abruzzo, Italy, Earthquake, and Lessons Learned.* M. Selim Günay and Khalid M. Mosalam. April 2010.

PEER 2010/104 *Simulating the Inelastic Seismic Behavior of Steel Braced Frames, Including the Effects of Low-Cycle Fatigue.* Yuli Huang and Stephen A. Mahin. April 2010.

PEER 2010/103 *Post-Earthquake Traffic Capacity of Modern Bridges in California.* Vesna Terzic and Božidar Stojadinović. March 2010.

PEER 2010/102 *Analysis of Cumulative Absolute Velocity (CAV) and JMA Instrumental Seismic Intensity (I_{JMA}) Using the PEER–NGA Strong Motion Database.* Kenneth W. Campbell and Yousef Bozorgnia. February 2010.

PEER 2010/101 *Rocking Response of Bridges on Shallow Foundations.* Jose A. Ugalde, Bruce L. Kutter, and Boris Jeremic. April 2010.

PEER 2009/109 *Simulation and Performance-Based Earthquake Engineering Assessment of Self-Centering Post-Tensioned Concrete Bridge Systems.* Won K. Lee and Sarah L. Billington. December 2009.

PEER 2009/108 *PEER Lifelines Geotechnical Virtual Data Center.* J. Carl Stepp, Daniel J. Ponti, Loren L. Turner, Jennifer N. Swift, Sean Devlin, Yang Zhu, Jean Benoit, and John Bobbitt. September 2009.

PEER 2009/107 *Experimental and Computational Evaluation of Current and Innovative In-Span Hinge Details in Reinforced Concrete Box-Girder Bridges: Part 2: Post-Test Analysis and Design Recommendations.* Matias A. Hube and Khalid M. Mosalam. December 2009.

PEER 2009/106 *Shear Strength Models of Exterior Beam-Column Joints without Transverse Reinforcement.* Sangjoon Park and Khalid M. Mosalam. November 2009.

PEER 2009/105 *Reduced Uncertainty of Ground Motion Prediction Equations through Bayesian Variance Analysis.* Robb Eric S. Moss. November 2009.

PEER 2009/104 *Advanced Implementation of Hybrid Simulation.* Andreas H. Schellenberg, Stephen A. Mahin, Gregory L. Fenves. November 2009.

PEER 2009/103 *Performance Evaluation of Innovative Steel Braced Frames.* T. Y. Yang, Jack P. Moehle, and Božidar Stojadinovic. August 2009.

PEER 2009/102 *Reinvestigation of Liquefaction and Nonliquefaction Case Histories from the 1976 Tangshan Earthquake.* Robb Eric Moss, Robert E. Kayen, Liyuan Tong, Songyu Liu, Guojun Cai, and Jiaer Wu. August 2009.

PEER 2009/101 *Report of the First Joint Planning Meeting for the Second Phase of NEES/E-Defense Collaborative Research on Earthquake Engineering.* Stephen A. Mahin et al. July 2009.

PEER 2008/104 *Experimental and Analytical Study of the Seismic Performance of Retaining Structures.* Linda Al Atik and Nicholas Sitar. January 2009.

PEER 2008/103 *Experimental and Computational Evaluation of Current and Innovative In-Span Hinge Details in Reinforced Concrete Box-Girder Bridges. Part 1: Experimental Findings and Pre-Test Analysis.* Matias A. Hube and Khalid M. Mosalam. January 2009.

PEER 2008/102 *Modeling of Unreinforced Masonry Infill Walls Considering In-Plane and Out-of-Plane Interaction.* Stephen Kadysiewski and Khalid M. Mosalam. January 2009.

PEER 2008/101 *Seismic Performance Objectives for Tall Buildings.* William T. Holmes, Charles Kircher, William Petak, and Nabih Youssef. August 2008.

PEER 2007/101 *Generalized Hybrid Simulation Framework for Structural Systems Subjected to Seismic Loading.* Tarek Elkhoraibi and Khalid M. Mosalam. July 2007.

PEER 2007/100 *Seismic Evaluation of Reinforced Concrete Buildings Including Effects of Masonry Infill Walls.* Alidad Hashemi and Khalid M. Mosalam. July 2007.

The Pacific Earthquake Engineering Research Center (PEER) is a multi-institutional research and education center with headquarters at the University of California, Berkeley. Investigators from over 20 universities, several consulting companies, and researchers at various state and federal government agencies contribute to research programs focused on performance-based earthquake engineering.

These research programs aim to identify and reduce the risks from major earthquakes to life safety and to the economy by including research in a wide variety of disciplines including structural and geotechnical engineering, geology/seismology, lifelines, transportation, architecture, economics, risk management, and public policy.

PEER is supported by federal, state, local, and regional agencies, together with industry partners.

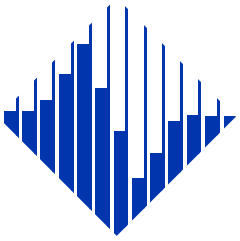

PEER Core Institutions:
University of California, Berkeley (Lead Institution)
California Institute of Technology
Oregon State University
Stanford University
University of California, Davis
University of California, Irvine
University of California, Los Angeles
University of California, San Diego
University of Southern California
University of Washington

PEER reports can be ordered at http://peer.berkeley.edu/publications/peer_reports.html or by contacting

Pacific Earthquake Engineering Research Center
University of California, Berkeley
325 Davis Hall, mail code 1792
Berkeley, CA 94720-1792
Tel: 510-642-3437
Fax: 510-642-1655
Email: peer_editor@berkeley.edu

ISSN 1547-0587X